Developing transition metal dichalcogenide alloys for applications to integrated photonics

by

Yifei Li

B.S., University of Illinois at Urbana-Champaign (2016)

Submitted to the Department of Materials Science and Engineering in partial fulfillment of the requirements for the degree of

DOCTOR OF PHILOSOPHY IN MATERIALS SCIENCE AND ENGINEERING

AT THE

MASSACHUSETTS INSTITUTE OF TECHNOLOGY

July 2022

© 2022 Massachusetts Institute of Technology. All rights reserved.

Signature of Author: ____
Department of Materials Science and Engineering
July 19, 2022

Certified by: ____
Rafael Jaramillo
Thomas Lord Associate Professor of Materials Science and Engineering
Thesis Supervisor

Certified by: ____
Ju Li
Battelle Energy Alliance Professor of Nuclear Science and Engineering
Professor of Materials Science and Engineering
Thesis Supervisor

Accepted by: ____
Prof. Frances Ross
Chair, Departmental Committee on Graduate Studies

Developing transition metal dichalcogenide alloys for applications to integrated photonics

by

Yifei Li

Submitted to the Department of Materials Science and Engineering
on Jan 14, 2022, in partial fulfillment of the
requirements for the degree of
Doctor of Philosophy in Materials Science and Engineering

Abstract

We explore the potential of transition metal dichalcogenides (TMDs) as phase-change materials for photonics integrated circuits (PIC). We measure the near-infrared (NIR) optical properties of bulk crystal telluride TMDs and sulfide TMDs. We find that telluride TMDs have large optical density and large optical contrast, but the loss is too high. The sulfide TMDs have lower loss, but the phase change energy is much higher. We further propose designing sulfide TMD alloys that are thermodynamically adjacent to phase boundaries between competing crystal structures, to realize martensitic (*i.e.,* displacive, order-order) switching. We report large-area thin film synthesis of 1T TiS_2 and high-Ti-content, single-phase 2H alloy $Mo_{1-x}Ti_xS_2$ thin films at temperature as low as 500 °C using a scalable two-step method of metal film deposition, followed by sulfurization in an H_2S gas furnace. We demonstrate different roughening processes for each case and optimize the morphology.

Thesis Supervisor: Rafael Jaramillo, Ju Li
Title: Thomas Lord Associate Professor, Battelle Energy Alliance Professor

Acknowledgements

I am grateful to my advisor Professor Rafael Jaramillo and Professor Ju Li for their instruction. I can't finish the thesis without them and I really hope I could learn more from them during my phD candidate time.

I want to thank my family and friends for the support in my hard time.

I also want to thank every colleague who helped me on the project:

$Mo_{1-x}W_xTe_2$ crystal synthesis: Sergiy Krylyuk, Albert Davydov

Optical property characterization: Akshay Singh, Seong Soon Jo, Balint Fodor, Laszlo Makai

DFT calculations: Haowei Xu, Jian Zhou

Film synthesis: Akshay Singh, Seong Soon Jo, Heshan Yu, Prof. Ichiro Takeuchi

Bulk crystal synthesis: Seng Huat Lee

Electron Microscopy: Austin Akey, Kate Reidy, Baoming Wang, Prof. Frances Ross

Synchrotron X-ray microscopy: Zhonghou Cai, Tao Zhou, Michael Xu, Prof. James LeBeau

Ion-intercalation: Younggyu Kim, Mantao Huang, Seungchan Ryu, Prof. Bilge Yildiz

Giant photo-elasticity: Yuying Zhou, Alan Schwartzman, Bilal Azhar, Joseph Bennett

MRL: Charlie Settens, Timothy McClure, Libby Shaw, Lars Llorente

Nano: Kurt Broderick, Gary Riggott, Paul Tierney, Tim Turner, Anna Osherov

LEM: Mike Tarkanian, Jame Hunter, Shaymus Hudson, David Bono

EHS: Jim Doughty

Harvard CNS: Greg Lin, Arthur McClelland

Contents

Chapter 1: Introduction
1.1. Active phase change photonic materials
1.2. Transition Metal Dichalcogenides (TMDs) materials
1.3. Thesis overview

Chapter 2: NIR optical property measurement of bulk crystal TMDs
2.1. Introduction
2.2. Method
2.2.1. Ellipsometry
2.2.2. Fourier Transform InfraRed (FTIR)
2.2.3. Density Functional Theory (DFT) calculation
2.3. NIR optical property of telluride TMD
2.3.1. Polymorphism of $MoWTe_2$
2.3.2. Materials preparation
2.3.3. Optical property and Figure of merit
2.3.4. Summary
2.4. NIR optical property of sulfide TMDs
2.4.1. Bulk crystal MoS_2, TiS_2 and ZrS_2
2.4.2. Optical property
2.4.3. Theory prediction as complementary
2.4.4. Rough surface and oxide layer characterization and model correction
2.4.5. The effects of focusing optics on TiS_2
2.4.6. Multiple angle of incidence (MAI) measurement
2.4.7. Mueller matrix (MM) measurement
2.5. Summary

3. Alloy Design of sulfide TMDs
3.1. Introduction
3.2. Methods
3.2.1. Quasi-Harmonic Approximation (QHA) method to calculate Gibbs free energy
3.2.2. Parameters
3.3. Results and Discussion
3.4. Summary

4. TMD synthesis
4.1. Films for photonic integrated circuits (PIC) application
4.2. Method
4.2.1. Two-step method
4.2.2. Characterization
4.3. The formation of large-area MoS_2 thin films by oxygen-catalyzed sulfurization
4.4. Making Large-Area Titanium Disulfide Films at Reduced Temperature by Balancing the Kinetics of Sulfurization and Roughening
4.4.1. Introduction
4.4.2. Experimental Techniques

4.4.3. Synthesized TiS_2 film
4.4.4. The correlation of O_2 background levels, process temperature and morphology
4.4.5. The roughening mechanism
4.4.6. Summary
4.5. Stabilizing far-from-equilibrium $(Mo,Ti)S_2$ thin films by metal sulfurization at reduced temperature
4.5.1. Introduction
4.5.2. Experimental Techniques
4.5.3. Synthesized $Mo_{0.6}Ti_{0.4}S_2$ film
4.5.4. Morphology optimization by rapid sulfurization at low temperature
4.5.5. Orientation of synthesized film
4.5.6. Optical property
4.5.7. Summary
4.6. Summary

5. Ongoing and Future Work
5.1. Phase change demonstration
5.1.1. Design of stack for voltage gating TMD
5.1.2. Method: fabrication and characterization
5.1.3. Intermediate results and discussion
5.1.4. Experiments for ion-intercalation
5.2. Recommendation for Future Work
5.3. Conclusion and Key Findings of the Thesis

Chapter 1: Introduction

1.1 Active Phase Change Materials

Integrated photonic circuits offer the possibility to process massive data flows with faster speed and lower energy consumption than electronic circuits, and to construct beyond-von Neumann computing architectures including functions such as compute-in-memory and deep learning.[1,2] Essential for photonic circuits are active materials that can modulate the phase and amplitude of light to perform switching, logic, and signal processing; if these changes are non-volatile, then they can also be used for memory. To fulfill the requirement of aggressively- miniaturized integration, photonic materials should have strong light-matter interaction and process compatibility with other materials. Particularly for active materials, low fatigue and excellent durability are necessary for the longevity of high-frequency devices.

The most well-established active photonic materials interact weakly with near infrared (NIR) light, and thus require a large interaction volume.[3] The interaction length required to produce a substantial modulation of the optical phase is $L\sim \lambda_0/\Delta n$, where λ_0 is the free-space wavelength, and Δn is the refractive index change. For instance, commercially-established materials such as $LiNbO_3$ using the Pockels effect, and Si using the plasma dispersion effect, produce Δn in the order of 0.001, and thus require millimeter-scale interaction lengths.[4] In contrast, phase-change materials such as the widely-studied Ge-Sb-Te (GST) system feature refractive index changes $\Delta n > 1$ between crystalline and amorphous phases,[5,6] and are therefore of interest as active materials for integrated photonics. In these materials, phase-change functionality is based on time-temperature processing to achieve melt-quench and recrystallization transformations. This operating principle leads to high power consumption and fatigue problems (*e.g.* poor durability for

more than a billion cycles[7]). Also, the operation frequency is limited to sub-GHz due to the kinetics of recrystallization.[7,8]

Therefore, there is a need to expand the selection of materials available for phase-change functionality in the NIR for integrated photonics.

1.2. Transition Metal Dichalcogenides (TMDs) materials

In view of the need for active materials for integrated photonics, and the challenges presented by established phase-change materials, continued discovery and development of active materials is important. In this contribution we explore transition metal dichalcogenides (TMDs) as candidates for phase-change photonic materials.

TMDs are layered materials (van der Waals-bonded solids) with intriguing physical properties that include layer-number-dependent band gap, electron pseudospin, exciton and trion excitations, chemical tunability, catalytic action, polymorphism and phase-change behavior, and strong above-band gap light absorption [9–17]. Weak van der Waals bonds between layers suggests process compatibility and easy integration with various material platforms, with reduced concerns over matching crystal structures or thermal expansion coefficients. The wide chemical and crystallographic variety of TMDs provides flexibility for optimizing materials and composites for particular uses, including phase-change applications. Hence, TMDs are intriguing for development as phase-change materials for integrated photonics applications[18–20].

The NIR and below-band gap optical properties of TMDs have been little-studied[21–24]. TMDs interact strongly with light, and are expected to feature low-loss for below-band gap wavelengths. Polymorphism suggests that transition between structural phases (e.g., 2H and 1T discussed in **Chapter 2**) may be useful for optical switching[25,26]. This diffusionless, order-order transformation

(Martensitic transformation) is expected to be faster, require less energy, and to cause less fatigue than melt-quench and recrystallization transformations needed for GST.

1.3. Thesis overview

In the thesis, we try to develop TMD materials for applications to photonics integrated circuits. In the material design, our first idea is to use telluride TMDs, whose reversible phase transformation has been demonstrated. Hence, we establish methods to test NIR optical properties of bulk crystals using ellipsometry, Fourier Transform InfraRed (FTIR) and Density Functional Theory (DFT) (**Section 2.2**). However, following optical measurements show the large optical loss of tellurides (**Section 2.3**). Thus, we turn to sulfide TMDs with larger band gaps and the low loss is confirmed optical measurement on bulk crystals (**Section 2.4**). However, the switching energy of pure transition metal TMDs (e.g., MoS_2, TiS_2) is too high, which makes the switching slow and power-hungry. Therefore, we use theoretical prediction (**Section 3.2**) to explore the alloy TMDs and find that the switching energy of heterogenous alloy $Mo_xTi_{1-x}S_2$ could be reduced to almost zero with specific composition (**Section 3.3**). The material progress in shown in **Figure 1.1**.

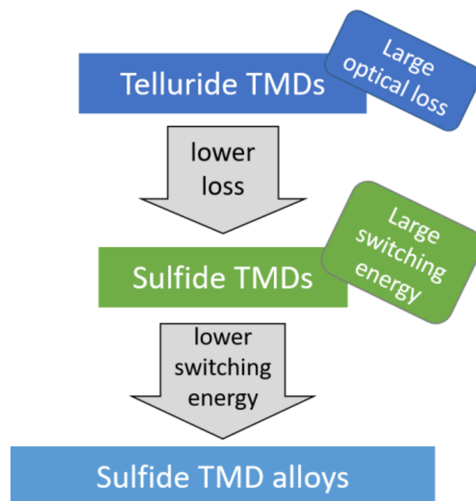

Figure 1.1: Materials design progress diagram

Utilizing TMDs in integrated photonic circuit technology require reliable methods to make and pattern large-area and uniform thin films. We develop a scalable two-step method (metal film deposition and sulfurization in H_2S) to grow large-area, uniform, polycrystalline thin films of TMDs (**Section 4.2**). Since the low switching energy requires the Mo:Ti ratio to be close to 1, which is far-from-equilibrium, we research the synthesis method of pure MoS_2 and TiS_2 at first. For MoS_2, we demonstrate the catalysis effect of O_2 in sulfurization (**Section 4.3**), whereas for TiS_2, we discuss the correlations between background O_2 level, lowest process temperature and surface morphology (**Section 4.4**). Finally, we synthesize alloy $Mo_xTi_{1-x}S_2$ and optimize the morphology by suppressing the phase segregation (**Section 4.4**).

Chapter 2: NIR optical property measurement of bulk crystal TMDs

The chapter reproduces our previously published work on optical property measurement on bulk crystal telluride TMDs and sulfide TMDs[18,19]. I contributed on ellipsometry and FTIR measurement with data analysis and DFT prediction of dielectric function.

2.1. Introduction

The NIR and below-band gap optical properties of TMDs have been little-studied[21–24]. In this Chapter, we use spectroscopic ellipsometry, Fourier transform infrared spectroscopy, and density functional theory prediction (**Section 2.2**) to explore the optical properties of telluride TMD including $MoTe_2$ and $Mo_{0.91}W_{0.09}Te_2$ in both 2H and 1T phase (**Section 2.3**) and sulfide TMDs including 1T-ZrS_2, 1T-TiS_2, 2H-MoS_2 (**Section 2.4**) and 1T-MoS_2 (**Section 2.5**).

2.2. Method

2.2.1. Ellipsometry

Ellipsometry is an optical characterization method that measures the change of polarized light reflected (or transmitted) from flat samples. We show in **Figure 2.1** a schematic diagram of reflection ellipsometry. As a high-precision, fast, and non-destructive measurement, ellipsometry is a mainstay method for measuring material properties (*e.g.,* refractive index) and characterizing device processing (*e.g.*, layer thickness). Ellipsometry is highly-valued in commercial semiconductor wafer processing, due to its accuracy in characterizing thin films such as oxides on semiconductor substrates, and its ability to map large wafers and real-time monitoring. With proper modelling and calibration, ellipsometry can also characterize materials properties besides optical properties such as composition, crystallinity, doping concentration, and electrical conductivity.

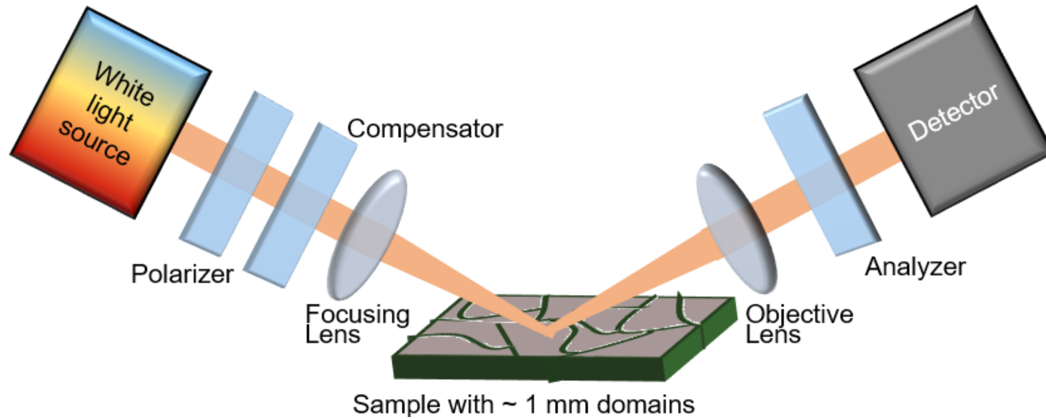

Figure 2.1: Schematic of SE-2000 ellipsometry setup. The SE-2000 system consists of the following elements in consecutive order: broadband white light source, polarizer, rotating compensator, micro-spot objective projecting the light onto the sample, analyzer, and finally the detection is performed by a CCD based multi-channel detector, or by a InGaAs photodiode array-based detector for the NIR range. Woollam VASE instrument performs similarly, but has an auto-retarder in place of the compensator, coupled with a rotating analyzer.

However, several limitations should be considered in the measurements. The ellipsometry has relative low accuracy in the characterization of low absorption coefficients (alpha < 100 cm^-1). Therefore, our conclusions that some TMDs have low-loss in the infrared regime are qualitative. Also, the samples need large, flat and smooth surface for measurement, but the surfaces of bulk TMD crystals, which will be discussed in following sections, are covered by small facets. Therefore, we have to use the focus optics to shrink the spot size to fit in a single facet, but the depolarization occurs because the incidence light beam is no longer parallel and angle of incidence varies. We generally neglected the focus effect in data analysis since the optical path is short and the variation due to focus is small, which will be further discussed in **Section 2.4**. Another problem in measuring bulk TMD crystals with facets is that we spent most of time on focusing and adjusting tilt angles, which may introduce extra inconsistency and error in experiments.

We performed spectroscopic measurements in UV-to-NIR spectral range (λ = 300 - 2100 nm) of 1T'-$MoTe_2$, 2H-$MoTe_2$, 1T'-$Mo_{0.91}W_{0.09}Te_2$, 2H-$Mo_{0.91}W_{0.09}Te_2$, 2H-MoS_2, 1T-TiS_2 and 1T-ZrS_2 single crystal samples using a Woollam UV-NIR Vase Ellipsometer and a Semilab SE-2000 with

focusing optics (spot size ~300 µm). The technique involves measuring the ellipsometric ratio (ρ) of the p- and s-polarized component of reflection Fresnel coefficients (r_{pp}, r_{sp}, r_{ps}, r_{ss}) on a smooth surface. A general form of the reflection matrix can be defined by the Jones matrix (J):

$$J = \begin{bmatrix} r_{pp} & r_{ps} \\ r_{sp} & r_{ss} \end{bmatrix} = r_{ss} \begin{bmatrix} \rho_{pp} & \rho_{ps} \\ \rho_{sp} & 1 \end{bmatrix} \tag{2.1}$$

where the cross-polarization components ρ_{ps} and ρ_{sp} are 0 for isotropic samples and birefringent samples with optic axes perpendicular to the surface. ρ (ρ_{pp}, we drop the subscript for convenience) is measured as

$$\rho = \frac{r_{pp}}{r_{ss}} = \tan(\psi)\exp(-i\Delta) \tag{2.2}$$

where ψ and Δ are the ellipsometric angles. ρ is a complex function of the wavelength, and can be used to directly calculate real and imaginary optical constants, without relying on Kramers-Kronig (KK) relations. Relying on KK-constrained data can result in erroneous results, due to extension of KK integral into spectral regions where measurements were not performed.

For a bulk, isotropic material the dielectric function ϵ can be calculated directly from ellipsometric data as

$$\tilde{n} = \sin(\Phi)\sqrt{1 + \tan^2(\Phi)\left(\frac{1-\rho}{1+\rho}\right)^2} \tag{2.3}$$

where we take the convention that $\tilde{n} = n + ik = \sqrt{\epsilon} = \sqrt{\epsilon_1 + i\epsilon_2}$, and Φ is the angle of incidence (AoI) relative to the surface normal direction[27].

TMDs are highly anisotropic due to their layered crystal structures. We measured bulk crystals and synthesized films, all of which are birefringent with the optical axis perpendicular to the crystal surface, as shown in **Figure 2.2**. We label the complex refractive index for polarization perpendicular and parallel to the optical axis as ordinary (n_o, k_o) and extraordinary (n_e, k_e),

respectively. Fresnel coefficients for a semi-infinite thick, birefringent material with optical axes normal to the surface can be written as

$$r_{pp} = \frac{\tilde{n}_e * \tilde{n}_o * cos(\Phi) - \left(\tilde{n}_e{}^2 - \ sin^2(\Phi)\right)^{\frac{1}{2}}}{\tilde{n}_e * \tilde{n}_o * cos(\Phi) + \ \left(\tilde{n}_e{}^2 - \ sin^2(\Phi)\right)^{\frac{1}{2}}} \tag{2.4}$$

$$r_{ss} = \frac{cos(\Phi) - \left(\tilde{n}_o{}^2 - \ sin^2(\Phi)\right)^{\frac{1}{2}}}{cos(\Phi) + \left(\tilde{n}_o{}^2 \ - \ sin^2(\Phi)\right)^{\frac{1}{2}}} \tag{2.5}$$

where $\tilde{n}_e, \tilde{n}_o$ are in-plane and out-of-plane complex refractive indices respectively, and Φ is *AoI*.[28] Subsequently, an pseudo-refractive index $\tilde{n}_{eff}$ can be defined and calculated using **Equation 2.2** and **2.3.**

Since the in-plane refractive index of TMDs is large, incident light is strongly refracted for practical values of the *AoI* (~70°, to avoid Brewster's angle). Therefore, the E-field of the light propagating within the material is nearly-parallel to the optic axis, and as a result, ellipsometry is far more sensitive to the ordinary than to the extraordinary refractive index.[18] Under these conditions, for measurements on semi-infinite TMD crystals, the ordinary refractive index is well-approximated by $\tilde{n}_{\mathrm{eff}}$, as the simulation shown in **Figure 2.3**. Also, the $\tilde{n}_{\mathrm{eff}}$ depends on the *AoI*, but the variation is small, as shown in **Section 2.4**. In the following section, we will only report the pseudo-refractive index $\tilde{n}_{eff}$ results from ellipsometer, as an approximation to the in-plane refractive index $\tilde{n}_{\mathrm{o}}$. We note that the pseudo-refractive index could be useful in multilayer structure as well. If the $\tilde{n}_{\mathrm{eff}}$ at specific *AoI* of the bulk is known, the measurement on the anisotropic film with the same orientation at the same *AoI* can be modeled as that on an isotropic film with measured $\tilde{n}_{\mathrm{eff}}$ without any error or correction, and the thickness can be efficiently

determined by nonlinear fitting. Since the $\tilde{n}_{\mathrm{eff}}$ is almost invariant as the *AoI* varies, the approximation is useful for any *AoI*.

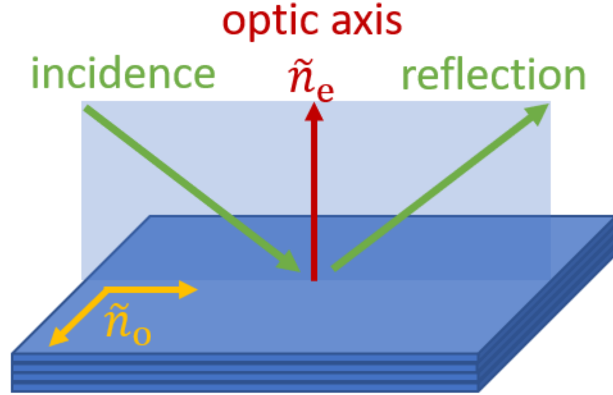

Figure 2.2: Model of a semi-infinite, birefringent sample with optical axes normal to the exposed face.

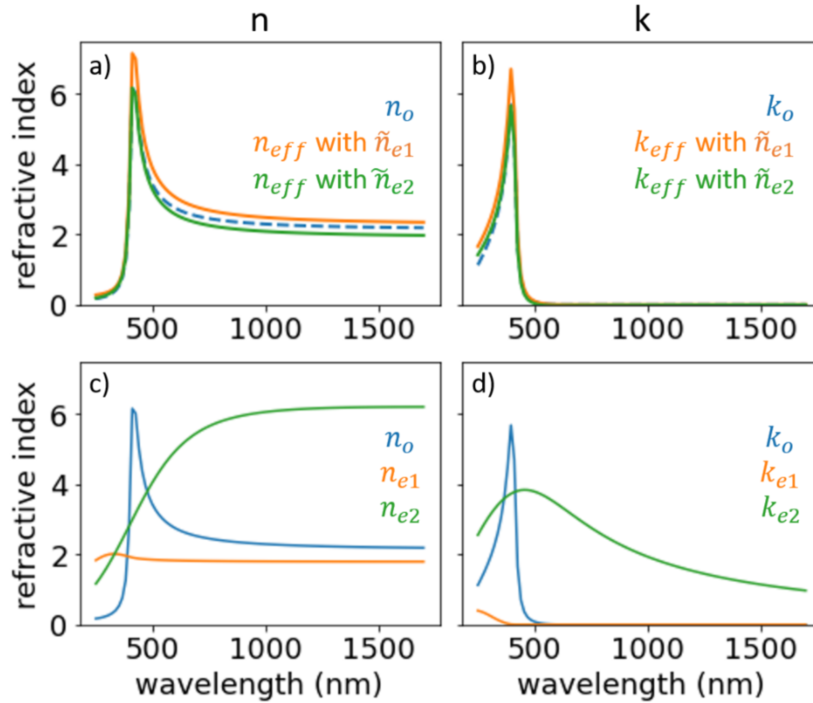

Figure 2.3: Pseudo-refractive index $\tilde{n}_{eff}$ is a good approximation of in-plane refractive index $\tilde{n}_o$. We simulated ellipsometer-measured (*AoI*=70°) pseudo-refractive indices $\tilde{n}_{eff}$, corresponding to birefringent materials with same in-plane refractive index $\tilde{n}_o$ and highly distinct out-of-plane refractive $\tilde{n}_{e1}$ and $\tilde{n}_{e2}$. $\tilde{n}_o$, $\tilde{n}_{e1}$ and $\tilde{n}_{e2}$ are random generated by single peak Tauc-Lorentz model. a) b) Real and imagery part of $\tilde{n}_o$ and $\tilde{n}_{eff}$ from the birefringent materials with $\tilde{n}_o$ and $\tilde{n}_{e1}$ or $\tilde{n}_{e2}$. c) d) Real and

imagery part of $\tilde{n}_o$, $\tilde{n}_{e1}$ and $\tilde{n}_{e2}$ for reference. Even though $\tilde{n}_{e1}$ and $\tilde{n}_{e2}$ are highly distinct, the corresponding $\tilde{n}_{eff}$ are quite close to $\tilde{n}_o$.

Another major difficulty in ellipsometry is data analysis. As an indirect technique, analyzing ellipsometry data amounts to solving an inverse problem. For a specific optical model including sample geometry and incidence plane, there exists an analytic forward function that maps material properties to experimental data: ellipsometric angles (Ψ and Δ) as a function of wavelength (λ) and angle of incidence (AoI). To interpret materials properties from experimental data, the inverse function (*i.e.,* the backward function) needs to be solved, explicitly or implicitly. However, the forward function is complex and nonlinear, which makes inversion difficult. For well-understood materials and a limited number of unknowns (*e.g.* oxide thickness), ellipsometry data is straightforward to analyze. However, in more complex scenarios the analysis is often inaccurate, highly time-consuming, or both. Such can be the case when material properties or the sample structure are unknown.

There are several established approaches used to derive optical properties from spectroscopic ellipsometry data by inverting the forward function. The most common approach is nonlinear regression, combined with models that represent optical materials properties using a small number of parameters, such as Drude and Tauc-Lorentz models. A related approach is spline analysis.[29,30] In this approach, the imaginary part of the dielectric function is parametrized by a piecewise polynomial, and the real part is calculated by the KK relation. In this case, the nonlinear regression acts on the spline parameterization, rather than on the underlying spectral model. The spline approach avoids assuming particular models for the material and can improve accuracy, but comes with an added computational cost. A third approach may be termed wavelength-by-wavelength.[31,32] At a given wavelength, the forward function depends only on the sample properties, not on the evaluation at other wavelengths. Hence, at a given wavelength, the input and

output tensors of the forward function have relatively low dimensionality (*e.g.*, less than 10), which makes it possible to analytically approximate the inverse function. However, this approach is valid only when the forward function is one-to-one, and there is no simple criterion to determine whether this is the case. Also, since the function is evaluated wavelength-by-wavelength, this approach doesn't guarantee the continuity, smoothness, and KK-consistency of the inferred spectrum. Working on complicated models, each of these established approaches could be time-consuming, inaccurate, and may involve strong assumptions.

The three methods introduced above can also be considered (classified) as a type of conventional machine learning (ML). Training time is proportional to the parameter space volume, which grows exponentially with the number of parameters. Conventional ML based on nonlinear regression may converge reasonably well, but only when the model parameters are initialized well, and this often requires much experience (human factor). Compared to conventional ML, the accuracy and analysis speed of deep learning (DL) increases exponentially with the size of the training data set. DL training emulates the process by which an experienced expert may initialize model parameters for nonlinear regression. We developed a series of automatic data analysis methods based on deep learning which demonstrate higher accuracy (5x) and faster inferring speed (1000x) on specific multilayer GeSbTe stacks. This work is a separate work that I did as a student in MIT, although outside the scope of my thesis here[33].

2.2.2. Fourier Transform InfraRed spectroscopy (FTIR)

We used an FTIR microscope (Bruker Lumos) to measure normal-incidence reflectance in the IR (λ = 1.3 - 16.6 μm) of 1T'-$MoTe_2$, 2H-$MoTe_2$, 1T'-$Mo_{0.91}W_{0.09}Te_2$ and 2H-$Mo_{0.91}W_{0.09}Te_2$ single crystal samples. The reflectance (R) depends on the in-plane, ordinary refractive index (n_0 + ik_o) as

$$R = \frac{(n_0-1)^2+k_o{}^2}{(n_0+1)^2+k_o{}^2} \quad (2.6)$$

The reflectance is real-valued number in the range [0, 1], and cannot determine the in-plane complex refractive index without further modeling and/or Kramers-Kronig inversion. FTIR therefore contains less direct information about the optical material properties than ellipsometry.

However, FTIR measurement gives information from the normal incidence, which is forbidden in ellipsometry. The spot size of FTIR is much smaller (down to 50 μm on our instrument), thus smaller smooth regions on the surface are required and more diverse samples are possible. Also, the data are directly relevant to applications of phase-change materials for optical data storage. These attributes make FTIR a useful complementary technique to ellipsometry. However, the normal incidence also gives longer penetration depth. Therefore, the back reflection could be an issue in characterizing transparent materials. For comparison, we correct the spectra with back reflection by fitting the refractive indices (using multi-peak Tauc-Lorentz model) and layer thickness in finite thickness optical model (air-material-air) and reconstructing according to semi-infinite thick optical model (air-material)[19].

Equation 2.6 assumes that the sample is infinitely-thick, and the reflections from the back surface are non-existent. This assumption works well for semi-metallic 1T' samples with high absorption. However, the 2H samples are less than 100 μm thick, the FTIR measurements extend to λ = 16.6μm, and the semiconducting phase is not strongly absorbing below-band gap. Therefore, backside reflections in the semiconducting 2H samples result in substantial oscillations in the reflectivity data. To make a clear comparison between the reflectivity data for 2H and 1T' samples, highlighting the intrinsic material properties and not the sample dimensions, we used numerical modeling to remove the oscillations from the data. We used a model of a Lorentzian

dielectric media of finite-thickness to fit the data, and we then re-plotted the model predictions for an infinitely-thick sample according to **Equation 2.6**.

2.2.3. Density Functional Theory (DFT) calculation

We use the results of DFT electronic structure calculations to predict complex dielectric functions of bulk 2H-MoS_2, 1T-TiS_2 and 1T-ZrS_2 using the Random Phase Approximation (RPA)[34,35], which assumes that:

$$\varepsilon(q,\omega) = 1 - \frac{4\pi e^2}{q^2}\chi_0(q,\omega) \tag{2.7}$$

where q is the Bloch vector of the incident wave, ω is the frequency, $\chi_0(q,\omega)$ is the irreducible polarizability in the independent particle picture (Kohn-Sham levels). The polarizability contribution from correlation-exchange energy is ignored, but correlation-exchange energy is still involved because the energy levels, whom $\chi_0(q,\omega)$ corresponds to, are calculated with correlation-exchange term. Under the simplification, the imaginary part of the dielectric tensor in long wavelength limit (q→ 0) could be calculated as:

$$\epsilon^{(2)}_{\alpha\beta}(\omega) = \lim_{q\to 0}\left(\frac{4\pi e^2}{q^2\Omega}\right)\sum\nolimits_{c,v,k} 2w_k \left\langle u_{c,k+q\hat{\alpha}}\middle|u_{v,k}\right\rangle \left\langle u_{v,k}\middle|u_{c,k+q\hat{\beta}}\right\rangle \delta\left(E_{c,k} - E_{v,k} - \hbar\omega\right) \tag{2.8}$$

where $\alpha,\beta = x,y,z$ and $\hat{\alpha},\hat{\beta}$ are corresponding unit vectors, c and v indicate the conduction band states and valence band states respectively, $|u_{n,k}\rangle$ is the cell-periodic part of the wave functions of the band-n at k, Ω is the volume of the simulation supercell, w_k is the k-point weight. The real part of the dielectric tensor could be obtained by KK-relation:

$$\epsilon^{(1)}_{\alpha\beta}(\omega) = 1 + \frac{2}{\pi}P\int_0^\infty \frac{\epsilon^{(2)}_{\alpha\beta}(\omega)\omega'}{\omega'^2 - \omega^2}d\omega' \tag{2.9}$$

The DFT predictions provide a theoretical understanding of the dielectric properties of bulk TMDs and give reasonable estimations for the optical properties that the experiments can't provide,

including the out-of-plane refractive indices mentioned above and the dielectric functions of the materials not available in experiments.

We use Vienna ab-initio simulation package (VASP), version 5.4[36–39]. We treat the core and valence electrons by the projector-augmented plane-wave method, and we approximate the exchange-correlation interaction by the generalized gradient approximation functional, implemented in the Perdew-Burke-Ernzerhof form[40,41]. The energy minimization and force convergence criteria are 10^{-7} eV and 10^{-3} eV/Å, respectively. 10×10×5 Monkhorst-Pack k point mesh and fully relaxed unit cell are used for reasonable accuracy[42]. Phenomenological damping parameter was taken to be 0.025 eV in calculation.

The results are in qualitative agreement with the experiments results (shown in **Section 2.4**). However, due to the limit of computation power, we use PBE functional form in all the calculations. Hence, it should be noted that the DFT calculated electronic band structure has a substantial underestimation of the band gap (Kohn-Sham eigenvalues) and the effects of excitons are not included. Methods beyond the independent particle picture are required for better accuracy.

2.3. NIR optical property of telluride TMDs

2.3.1. Polymorphism of $MoWTe_2$

We study the $(Mo,W)Te_2$ system as a prototype. As shown in **Figure 2.4**, the 2H phase is trigonal prismatic, and 1T phase is octahedral. The monoclinic 1T' and orthorhombic T_d are charge-ordered (*i.e.* lower-symmetry) variations of the 1T structure, for which in-plane isotropy is broken, and are crystalographically very similar. $MoTe_2$ is a semiconductor in the 2H structure in its ground state, and can be prepared as a semi-metal in the 1T' structure as a metastable state. WTe_2 is a semi-metal in the T_d structure in its ground state, and could be a semiconductor in the 2H structure as a metastable state. The martensitic (*i.e.* displacive) phase transformation between

2H and 1T structures can be described by a lateral translation of one plane of chalcogen atoms.[43] This diffusionless, order-order transformation is expected to be faster, require less energy, and to cause less fatigue than melt-quench and recrystallization transformations needed for GST. Phase-change functionality at room-temperature has been demonstrated recently for $MoTe_2$ and $(Mo,W)Te_2$.[26,44,45] The energy (*i.e.* enthalpy at 0 K) difference between 2H and 1T' phases of $MoTe_2$ is 40 meV per formula unit (f.u.); for WTe_2, the energy difference between the 2H and T_d phases is -90 meV/f.u.[46] Making an alloy of $MoTe_2$ and WTe_2 decreases the energy difference between the 2H and distorted phases, and presumably reduces the energy barrier for switching.[46]

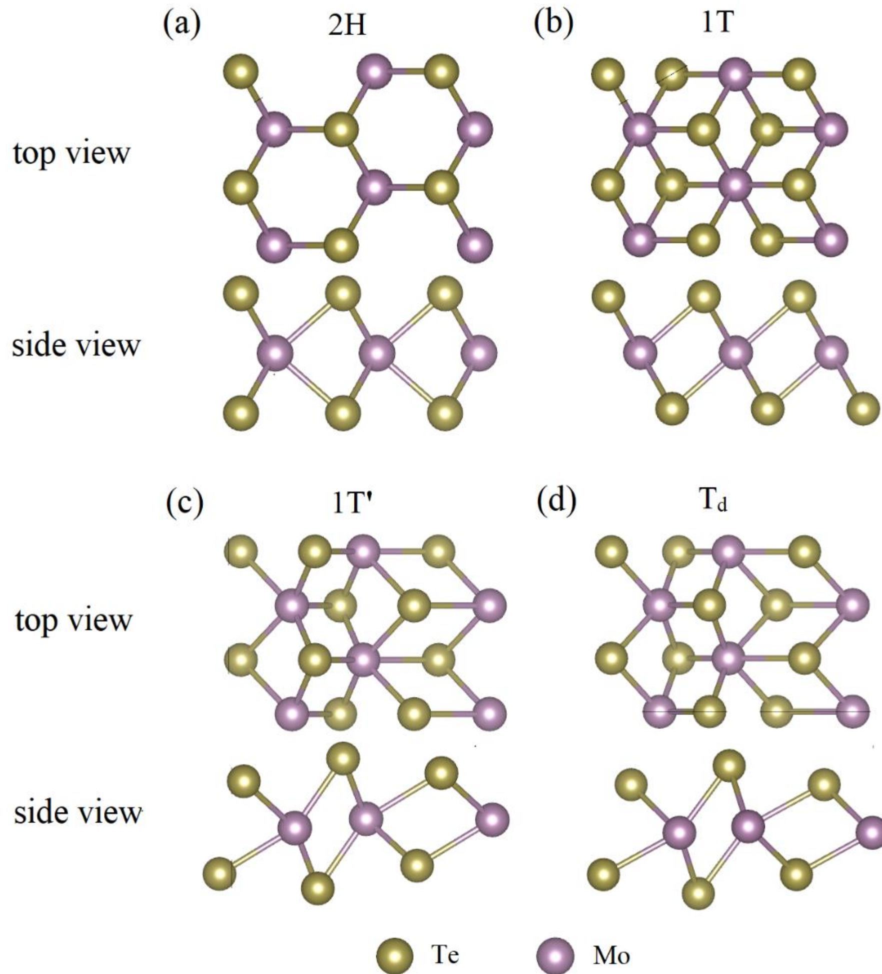

Figure 2.4: Top and side views of TMD crystal polymorphs: 2H (a), 1T (b), 1T' (c) and Td (d).

Here we study $MoTe_2$ and $Mo_{0.91}W_{0.09}Te_2$, which both have 2H phase as the ground state and 1T' phase as an excited, metastable state which can be experimentally-prepared. We measure the complex refractive index ($n + ik$) of 1T'-$MoTe_2$, 2H-$MoTe_2$, 1T'-$Mo_{0.91}W_{0.09}Te_2$ and 2H-$Mo_{0.91}W_{0.09}Te_2$ single crystal samples in the UV-to-NIR spectral region by spectroscopic ellipsometry (SE), and the normal-incidence reflectance by Fourier transform infrared spectroscopy (FTIR) microscopy. Our results show that the polymorphs of $MoTe_2$ and $Mo_{0.91}W_{0.09}Te_2$ have strong optical contrast in the NIR, and therefore may find use as phase-change materials for photonics. The loss coefficient of tellurium-based TMDs is rather large though, which motivates continued research on selenide and sulfide phase-change TMDs.

2.3.2. Materials preparation

We measured 1T'- and 2H-$Mo_{1-x}W_xTe_2$ crystals, $x = 0$ and 0.09, provided by Dr. Albert Davydov (NIST, Maryland), that were grown by the chemical vapor transport method[19]. All the samples are thin, single-crystalline flakes about few millimeters wide and about tens of micrometers thick. The smooth, mirror-like facets available for optical characterization vary from tens to hundreds of micrometers wide. The samples are highly-anisotropic due to the layered, van der Waals-bonded crystal structure. The 2H phase is birefringent. The 1T' and T_d phases are technically triaxial, due to broken in-plane symmetry. However, the charge-ordered domains are too small to be detected by the techniques used here, and may be irrelevant to many applications in integrated photonics; in other charge-ordered TMDs TaS_2 and $TaSe_2$, domains are on the nanometer-scale.[47,48] Therefore, we discuss all samples as if they are birefringent, with the ordinary optic axis (*i.e.* c-axis) perpendicular to the surface.

2.3.3. Optical property and Figure of merit

In **Figure 2.5** we present the complex refractive indices of $MoTe_2$ in the 2H and 1T' phases, measured by ellipsometry. Both phases have high n, indicating strong dielectric polarizability at optical frequencies. 1T'-MoTe2 has high loss coefficient throughout, as expected for a semimetal. It may be expected to have negative ϵ_1 at low energy, below the plasma edge, but our data do not extend into this region. As a semiconductor, 2H-$MoTe_2$ has suppressed loss below its band gap of 1.0 eV[49]. The spectral features that we measure for 2H-$MoTe_2$ match those previously reported by others. The A, B, A', and B' excitons (at 1.1, 1.4, 1.7, and 2.0 eV, respectively) that are split by spin-orbit and interlayer interactions are well-resolved, as are the C and D excitons (at 2.5 and 2.9 eV, respectively) that result from parallel band near the Brillouin zone Γ-point[49].

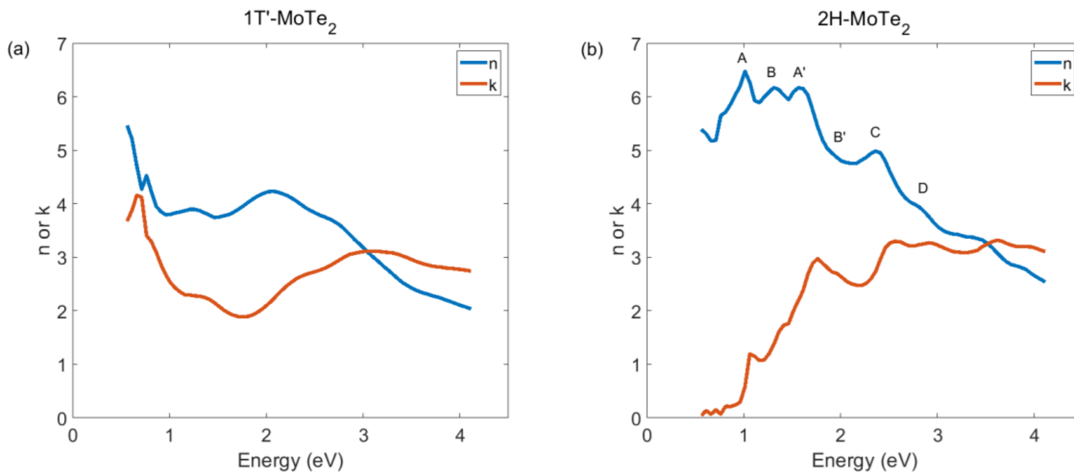

Figure 2.5: NIR-UV complex effective refractive index of 1T' (a) and 2H (b) $MoTe_2$. Measured at room-temperature and *AoI* = 70° by spectroscopic ellipsometry.

In **Figure 2.6** we present the difference between refractive indices of 2H- and 1T'-$MoTe_2$, $\Delta n = n_{2H} - n_{1T'}$. The large and variable data for n results in $\Delta n \sim \mathcal{O}(1)$. The prospects for phase-change performance can be captured by the figure-of-merit FOM $= |\Delta n|/(k_{2H} + k_{1T'})$, and the large Δn demonstrated here is promising. However, both phases are quite lossy, which suppresses the FOM to the range 0.4-0.9 the NIR bands most relevant for communications (1000 – 1550 nm).

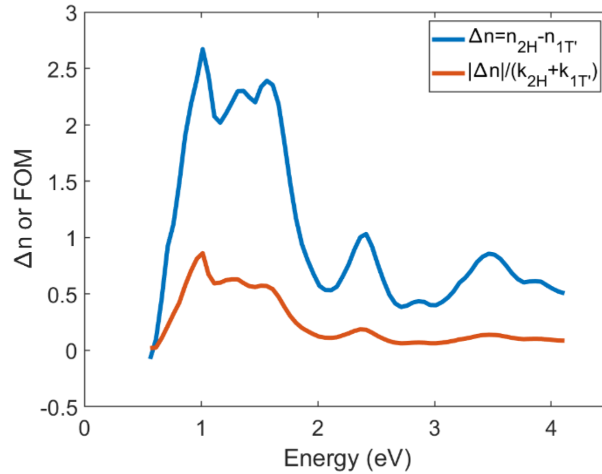

Figure 2.6: $\Delta n = n_{2H} - n_{1T'}$ and phase-change figure of merit, $\text{FOM} = |\Delta n|/(k_{2H} + k_{1T'})$ for $MoTe_2$.

In **Figure 2.7** we present the reflectance of 1T' and 2H phases of $MoTe_2$ and $Mo_{0.91}W_{0.09}Te_2$ in the range 0.05-0.9 eV, measured by FTIR microscopy. The semi-metallic 1T' phases have higher reflectivity than the semiconducting 2H phases, as expected. The strong optical contrast between phases persists even as the thermodynamic barrier decreases with alloying.

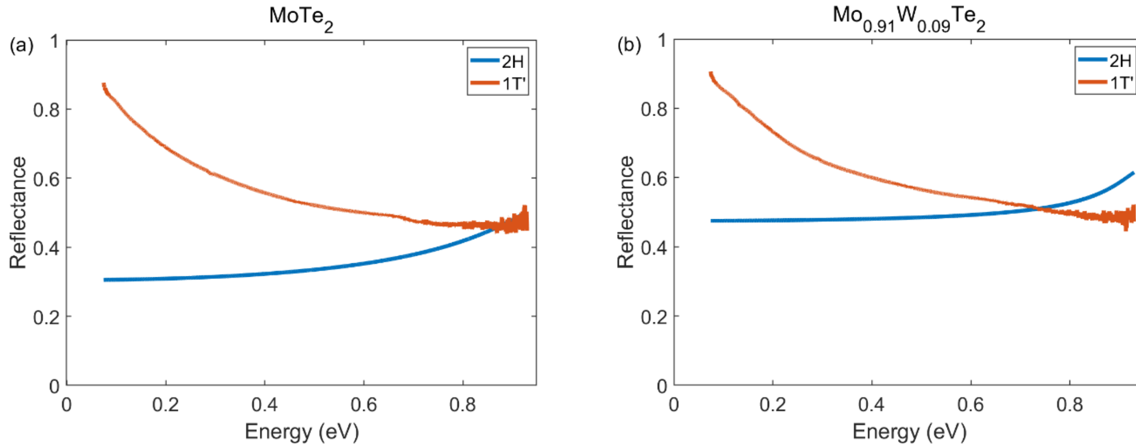

Figure 2.7: IR reflectance of 2H and 1T' $MoTe_2$ (a) and $Mo_{0.91}W_{0.09}Te_2$ (b) measured by FTIR microscopy. For the 2H-phase samples, the reflectance data has been corrected to account for backside reflection.

2.3.4. Summary

We use the (Mo,W)Te_2 system to explore the potential of TMDs as phase-change materials for integrated photonics. We measure the complex optical constant of $MoTe_2$ in both the 2H and 1T'

phases by spectroscopic ellipsometry. We find that both phases have large refractive index, which is good for confined light-matter interaction volume. The change Δn between phases is of $\mathcal{O}(1)$, which is large and comparable to established phase-change systems such as GST. However, both phases have large optical loss, which limits to FOM to below unity throughout the measured range. We further measure the NIR reflectivity of $MoTe_2$ and $Mo_{0.91}W_{0.09}Te_2$, in both the 2H and 1T' phases. The data show that the strong optical contrast between the 2H and 1T' structures persists even as the thermodynamic barrier between them is reduced by alloying. This bodes well for alloy design of phase-change materials.

Our results emphasize that TMDs have strong light-matter interaction, a number of polymorphs with strong optical contrast, and chemical diversity. The tellurium-based TMDs reported here have demonstrated phase-change operation, and may be relevant for applications including resistive memory and analog computing[44]. We suggest that selenium- and sulfur-based TMDs may be optimal for photonic phase-change applications because they are expected to have lower loss.

2.4. NIR optical property of sulfide TMDs

2.4.1. Bulk crystal MoS_2, TiS_2 and ZrS_2

In this section we focus on sulfide TMDs, because they have the largest band gap (relative to selenides and tellurides), and therefore offer the largest spectral range for low-loss, below-band gap operation. Here we measure the complex relative permittivity ($\epsilon = \epsilon_1 - i\epsilon_2$) of 2H-$MoS_2$, 1T-$ZrS_2$, and 1T-$TiS_2$ bulk crystals in the visible-to-NIR region (300 - 2100 nm), using spectroscopic ellipsometry (SE). We find that ϵ in the NIR cannot be simply extracted by extrapolating from visible light measurements, and requires explicit measurements. We find that spectroscopic measurements must account for the presence of rough surface and native oxide to avoid

overestimating NIR loss. We support our measurements with density functional theory (DFT) calculations, which further predict a large refractive index contrast between 2H and 1T phases.

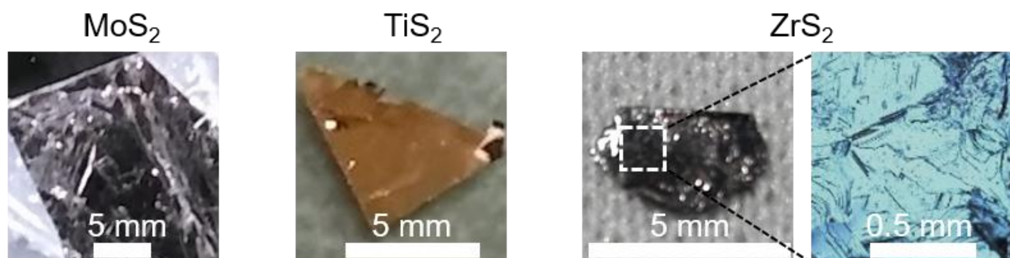

Figure 2.8: Low-magnification optical images of MoS_2, TiS_2 and ZrS_2 bulk crystals with different sized reflective facets. Higher magnification image (of dotted white box) of ZrS_2 is shown, clearly showing facets and heterogeneous nature of surface.

Optical images of bulk TMD crystals are shown in **Figure 2.8**. Sufficiently thick pieces of naturally occurring MoS_2 (from Smithsonian Institution, naturally-occurring molybdenite, catalog number NMNH B3306; and 2D Semiconductors), were chosen to reduce back reflections. The surface had ~ 1 mm scale reflective facets, which necessitated the use of focusing optics. TiS_2 was purchased from 2D Semiconductors (grown using flux technique) and had large reflective domains ~ 5 mm. ZrS_2 was purchased from 2Dsemiconductors, grown using flux zone method, and had a surface similar to MoS_2, with reflective domains ~ 1 mm. MoS_2 was measured using both Semilab and Woollam ellipsometers, with similar results; TiS_2 was measured using Woollam, and ZrS_2 was measured using Semilab ellipsometer.

2.4.2. Optical property

The presence of rough surface and native oxide layer affect the experimental results in the entire spectral range, and particularly for regions where the optical loss of the TMD is expected to be small, such as below the band gap of MoS_2 and ZrS_2. We directly measured the surface morphology, the thickness and composition of the native oxide using cross-sectional TEM. On MoS_2 we find a rough surface, possibly including a native oxide, approximately 2 nm thick. On ZrS_2 we find a native oxide layer nearly 20 nm thick; similarly thick native oxide layers have been

observed on $ZrSe_2$ [50]. On TiS_2 we saw no native oxide, within the imaging resolution of our experiment (~ 1 nm). Adding these overlayers to the optical model used to analyze the ellipsometry data significantly affects the extracted permittivity of MoS_2 and ZrS_2.

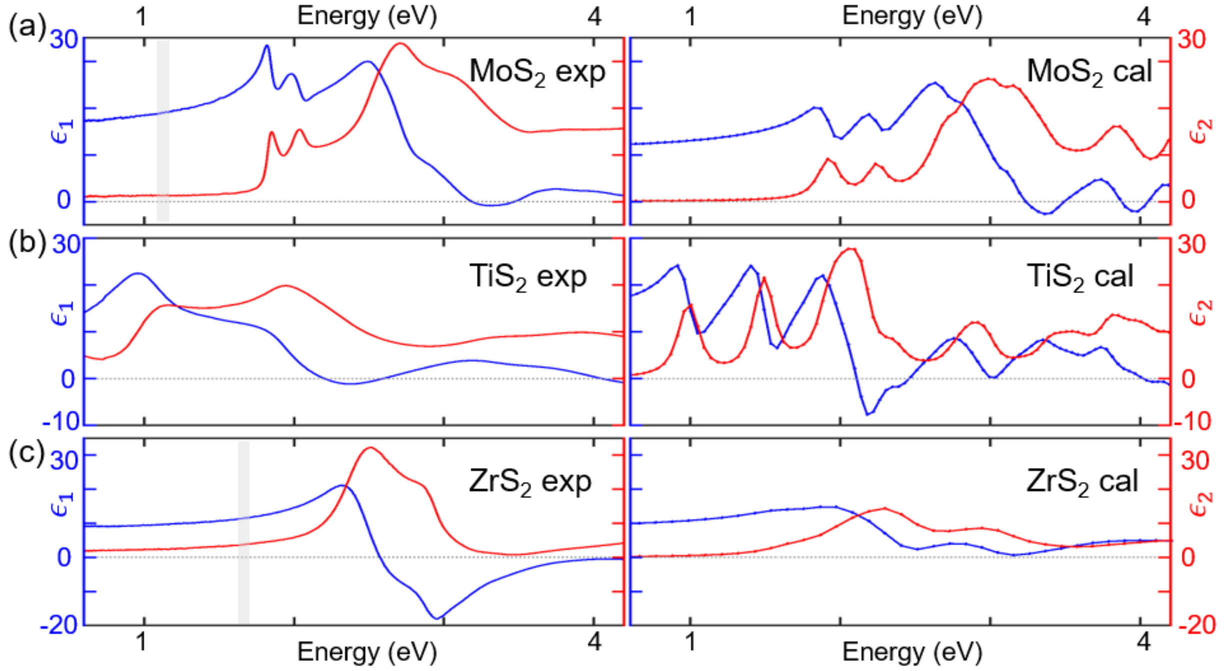

Figure 2.9: NIR-VIS complex relative permittivity (ϵ) of sulfide TMDs. (Left column) Experimentally measured actual permittivity at room-temperature and *AoI* = 70° by spectroscopic ellipsometry. (Right column) Calculated by DFT. Results shown for (a) 2H-MoS_2, (b)1T-TiS_2, and (c) 1T-ZrS_2. The indirect band gap of MoS_2 and ZrS_2 is indicated by light-gray lines.

In **Figure 2.9** we present the experimentally-measured and theoretically-calculated in-plane complex permittivity for MoS_2, TiS_2 and ZrS_2. The experimental data in **Figure 2.9** indicate the actual permittivity, determined by analyzing the ellipsometry data taking into account the rough surface and native oxide. Of particular relevance for NIR photonics, ϵ_1 is large below the band gap of MoS_2 and ZrS_2 (indirect E_g = 1.1 and 1.6 eV, respectively, indicated by solid gray lines); TiS_2 is a semimetal, (band gap ~ 0.3 - 0.5 eV) [23,51,52]. The DFT calculations match fairly well the experimental data, both in magnitude and in spectral position of individual features. The A, B and C excitons of MoS_2 are well-resolved[53]. For TiS_2, the experimentally-observed peaks match in

energy but are substantially broader than those calculated by DFT, and are qualitatively similar to previously-reported measurements of $TiSe_2$[22]. In ZrS_2, the strongest direct gap excitonic oscillators (2.5 eV and 2.9 eV) are observed in both experiment and theory, although the experimental data doesn't show the indirect gap transition near E_g. The 2.5 eV and 2.9 eV transitions are sufficiently close in energy to create zero-crossing of ϵ_1 near 3.2 eV, which is not seen in the DFT calculations. Cross-polarization components are explicitly measured through generalized ellipsometry, and are found to be ~ 0 for TiS_2 and MoS_2.

In **Figure 2.10** we plot experimentally-measured n and k in the NIR spectral region 0.6 - 1.5 eV (827 – 2067 nm). All three materials have large n, comparable to or larger than that of silicon ($n_{\text{NIR}} \approx 3.4$), which is appealing for guiding NIR light. MoS_2 and ZrS_2 are indirect-band gap semiconductors and have low-loss in the NIR. TiS_2 is semi-metallic and has higher loss.

The loss coefficients (k) determined by experiment and reported in **Figure 2.10** are conditional on the particular samples measured and on our optical modeling, and should be considered upper-bounds for these materials. In **Figure 2.10** we indicate k determined from **Equation 2.3**, assuming no rough surface and native oxide (dashed lines), and the value determined by optical modeling including effective roughness layer and native oxide thickness determined by TEM (solid lines). Taking the rough surface and native oxide into account results in a lower value of the determined loss. Another important variable is the presence of defects, which contribute to below-band gap absorption and optical loss. Our samples are bulk crystals (including a naturally-occurring specimen of MoS_2) and definitely contain defects, including sulfur vacancies that contribute to NIR absorption[54]. Measurements on synthetic MoS_2 monolayers have shown lower loss in the NIR [55,56]. Our theoretical calculations are performed using models of perfect, defect-free crystals and predict substantially lower loss than the experiments (see **Figure 2.9**). As the science of processing

TMD materials improves we will gain greater control over defects and can expect to have very low-loss TMDs for NIR applications.

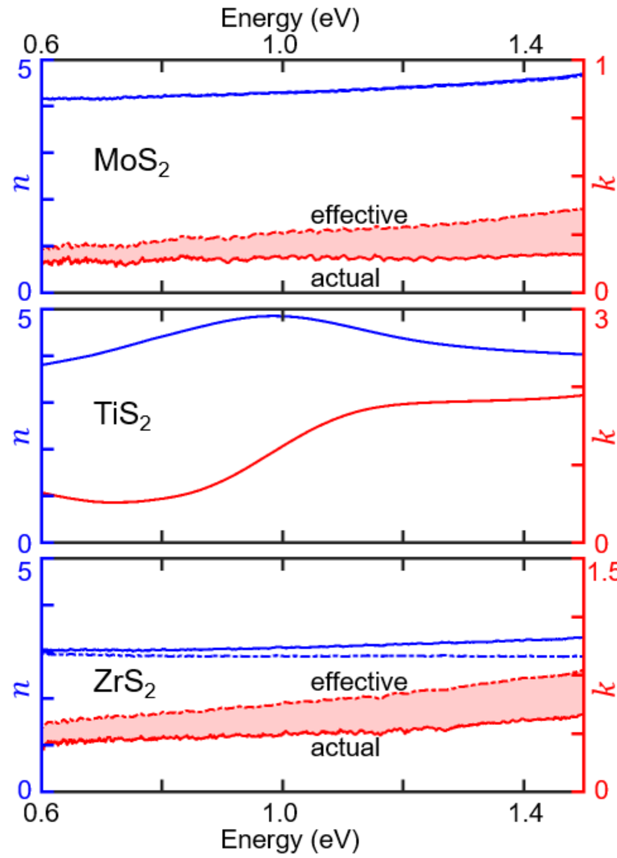

Figure 2.10: Experimentally-measured real (n) and imaginary (k) refractive index of MoS_2, TiS_2, and ZrS_2 in the NIR spectral region. The solid lines for MoS_2 and ZrS_2 are determined by modeling the ellipsometry data including rough surface and native oxide layers. The dashed lines represent the effective permittivity, which ignores the rough surface and native oxide. The red, shaded area represents experimental uncertainty (in k) due to potential mis-estimation of the rough surface and native oxide.

2.4.3. Theory prediction as complementary

Layered materials are expected to have large anisotropy due to the weak inter-layer bonding. Using DFT, we calculate the out-of-plane relative permittivity (ϵ_e) for all three TMDs under study. In **Figure 2.11**, ϵ_e and ϵ_o are plotted together for comparison. The calculated ϵ_e is much smaller than ϵ_o. Thus, we predict a large anisotropy between in-plane and out-of-plane directions, and these layered materials can be explored for optical modulators and polarization converters.

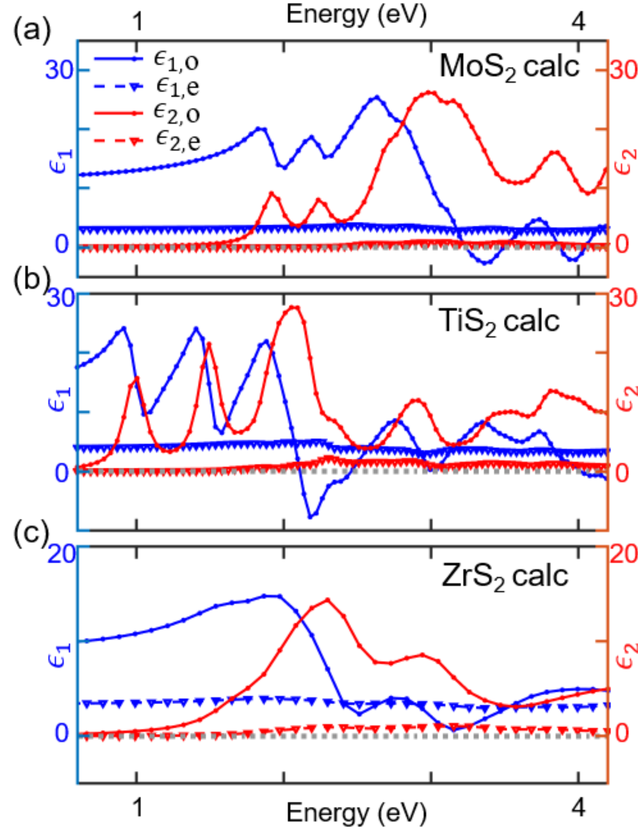

Figure 2.11: Comparison of calculated relative permittivity for electric field in-plane (ϵ_o, electric field perpendicular to the c-axis, solid line with circular markers) and out-of-plane (ϵ_e, electric field parallel to the c-axis, dotted line with triangular markers) for **(a)** MoS_2, **(b)** TiS_2 and **(c)** ZrS_2. ϵ_e is much smaller than ϵ_o, giving rise to giant birefringence.

In previous section, we demonstrate the consistency between experimental measurement and the theoretical simulation of the in-plane (or pseudo-) refractive index of birefringent TMDs. We now address the question of the usefulness of phase change in sulfide TMDs as functionality for active materials. In **Figure 2.12** we show the calculated refractive index difference (Δn) between the 2H and 1T' phases of bulk MoS_2. We here show results for the 1T' phase instead of 1T because, according to our DFT calculations, 1T' has lower energy than 1T for monolayer MoS_2, and therefore 1T may spontaneously relax to 1T' in the zero-temperature limit. Compared to the 1T phase, the 1T' phase has lower in-plane symmetry due to Mo-Mo dimerization, leading to optical tri-refringence. In **Figure 2.12** we have averaged the results for the principle in-plane axes for

consistency with the experimental literature, in which there is little evidence for strong in-plane anisotropy at room temperature (this could be due to ferroelastic domain microstructure, or a reduced order parameter at relatively high temperature). We find that Δn is large, comparable to or larger than that realized by phase-change materials in the GST system. The theoretically-predicted spectral features suggest photonics-relevant $\Delta n \sim 1$ throughout the NIR.

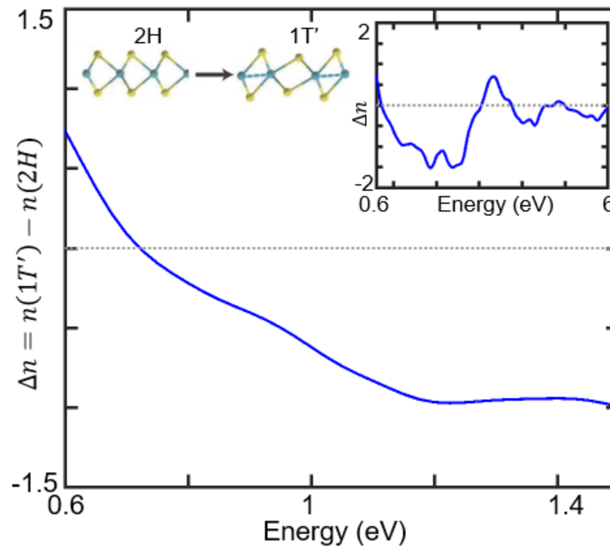

Figure 2.12: Theoretically-predicted refractive index difference (Δn) between the 1T' and 2H phases of bulk MoS_2 in the NIR. (Inset, right) Δn over a wider energy range. (Inset, left) Illustrated change of atomic structure for 2H-1T' phase transition.

2.4.4. Rough surface and oxide layer characterization and model correction

We used high-resolution TEM (HRTEM) and scanning TEM (STEM) to characterize the surface of bulk crystals. For TEM, we prepared cross-sectional samples via a gallium focused ion beam (FIB). We deposited a thin (~ 100 nm) amorphous carbon layer on top of the crystal for protection during subsequent FIB steps. Dark field (DF) STEM performed on MoS_2 (**Figure 2.13a**) indicates a slightly rough interface between carbon and underlying layered structure. HRTEM performed on TiS_2 (**Figure 2.13b**) shows a very sharp interface between FIB-deposited carbon and underlying crystals, and no overlayers. On the contrary, the ZrS_2 sample shows a thick amorphous layer on top of the pristine crystalline structure (**Figure 2.13c**).

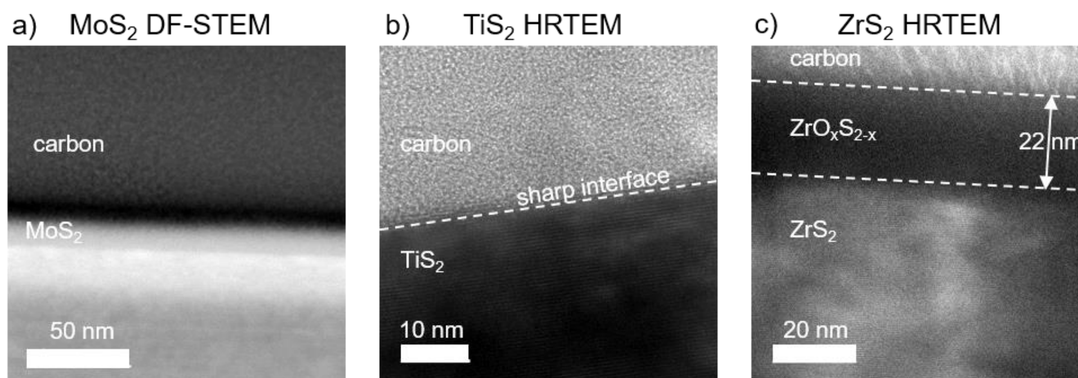

Figure 2.13: High-resolution TEM and STEM for sulfides. The carbon is deposited by focused ion beam instrument for protection of underlying crystalline material. a) Dark-field (DF) STEM for MoS_2 sample shows slightly rough interface between FIB-deposited carbon and underlying MoS_2. b) HRTEM for TiS_2 sample shows sharp interface between deposited carbon and underlying crystalline TiS_2. c) HRTEM for ZrS_2 sample shows amorphous overlayer on underlying crystalline ZrS_2.

To characterize the elemental composition of observed amorphous layers and top surface for MoS_2 and ZrS_2, we performed high resolution Energy Dispersive X-ray Spectroscopy (EDS) on the cross-sectional samples. In **Figure 2.14**, integrated intensities of characteristic X-ray peaks corresponding to carbon, transition metal (molybdenum/zirconium), sulfur and oxygen are plotted. For MoS_2, the interface seems fairly sharp (**Figure 2.14a**), and there is a distinct lack of oxygen in the underlying crystals. For ZrS_2, the amorphous layer measured via HRTEM, has a higher (lower) value of oxygen (sulfur/zirconium) compared to underlying pristine layers (**Figure 2.14b**). Qualitatively, we assign an average composition of 50% sulfur – 50% oxygen to this layer.

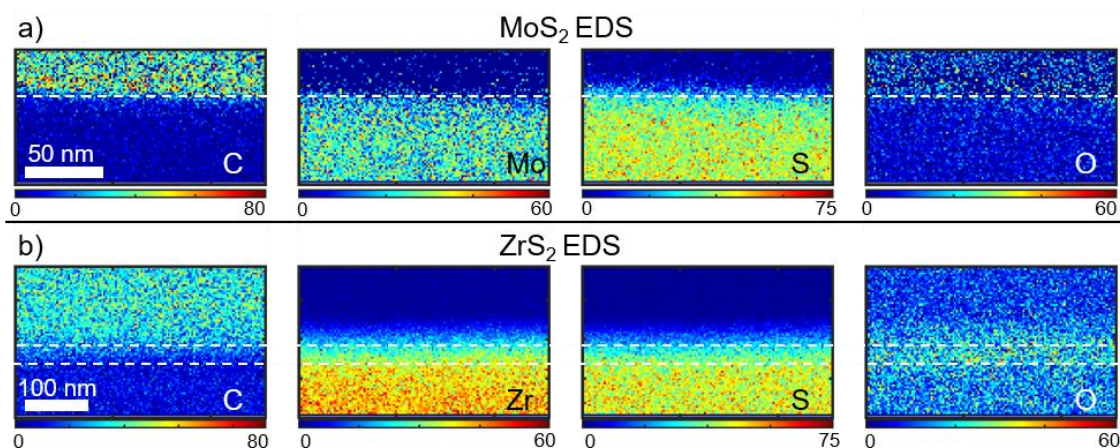

Figure 2.14: Energy Dispersive X-ray Spectroscopy (EDS) characterization of cross-sectional samples of a) MoS_2 and b) ZrS_2. The $K_{\alpha 1}$ lines are characteristic of the different elements (carbon, molybdenum/zirconium, sulfur and oxygen). The X-ray peaks are integrated to improve signal to noise.

TEM measurements show the presence of a moderately rough layer for MoS_2 (confirmed by atomic force microscopy, not shown here). The roughness is quantified as ~ 2 nm. Thus **Equation 2.3** can-not be simply used, and an optical model incorporating different layers needs to be defined. We define an optical model for the MoS_2 sample in **Figure 2.15a**. Similarly, an optical model for the ZrS_2 sample, incorporating a 20 nm overlayer is shown in **Figure 2.15b**. The modeling is performed using Semilab and Woollam software, and give similar results.

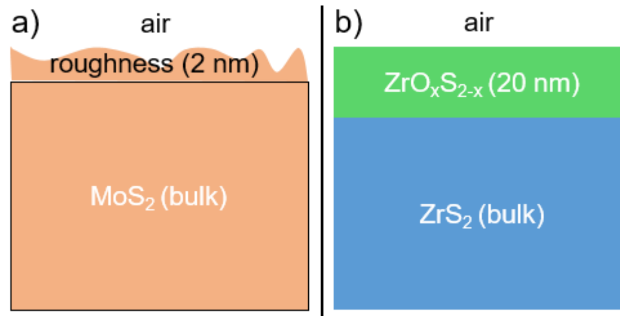

Figure 2.15: Schematic of the layer structure used for modeling raw ellipsometry data. a) MoS_2 data modeling incorporates a roughness layer of thickness ~ 2 nm on top of bulk MoS_2. b) ZrS_2 data modeling incorporates a zirconium oxy-sulfide layer (thickness ~ 20 nm) on top of bulk ZrS_2.

2.4.5. The effects of focusing optics on TiS_2

The focusing optics are necessary for a small spot size to avoid covering multiple small domains (with different tilts), which can cause mixing of polarizations. However, focusing optics can result in small amount of depolarization, and a change in the measured relative permittivity[27]. In **Figure 2.16**, we show that the measurements on TiS_2 using broad beam mode (3 mm spot size) and focusing beam mode (0.3 mm spot size) are quantitatively similar. Thus, the focusing mode can be used, without introducing error in the measurements. Note that such a comparison is only possible for TiS_2, since MoS_2 and ZrS_2 have very small (~ 1 mm) reflective domains.

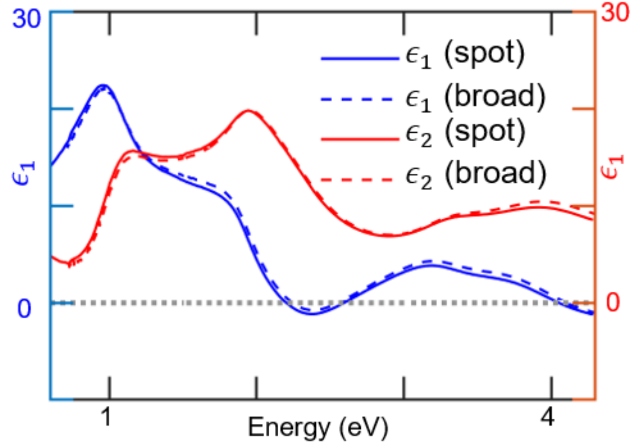

Figure 2.16: Comparison of relative permittivity measured via focused beam (spot) and broad beam (broad) for TiS_2 ($AoI = 70°$). The measurements are quantitatively similar, thus demonstrating focusing mode is suitable for ellipsometric measurements.

2.4.6. Multiple angle of incidence (MAI) measurement

To separate ϵ_o and ϵ_e, measurements at more than one AoI are needed. Measurements at low AoI are insensitive to ϵ_e, and high AoI is usually needed to measure ϵ_o. We carry out MAI measurements for MoS_2 and TiS_2, and display real part of effective (measured) relative permittivity (ϵ_1) in **Figure 2.17**. DFT calculations suggest a low ϵ_e, and suggest an increase in effective ϵ with increase in angles. The lack of measured changes in effective ϵ_1 for higher AoI (for MoS_2, TiS_2) is thus puzzling. However, after explicitly measuring the direction of optical axis, we realize that even at high AoI (for such high index materials), the measurement of ϵ_{eff} is only weakly dependent on ϵ_e. Thus, MAI measurements are unable to uncouple ϵ_o and ϵ_e due to high index and absorption. A way forward is to perform MAI measurements on the side-plane of polished and thick TMD crystals, where the optical axis will depend on sample rotation, and anisotropy will be extractable[57]. Such measurements are however, beyond the scope of this thesis.

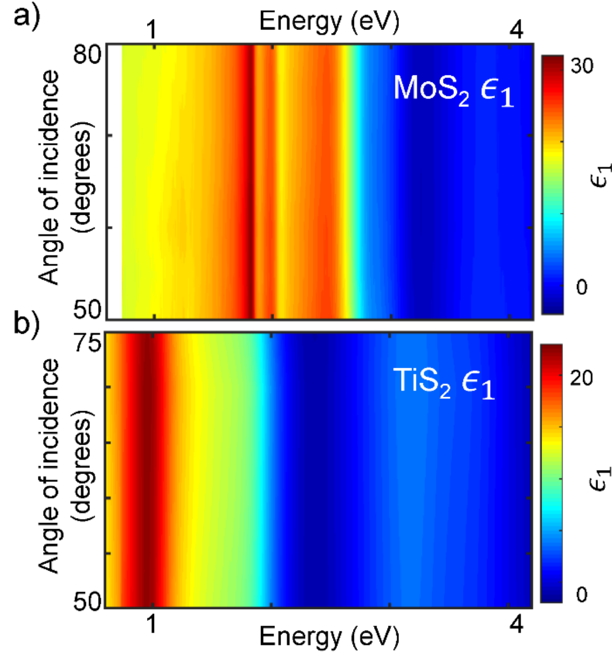

Figure 2.17: MAI measurements, plotting ϵ_1 for (a) MoS_2 and (b) TiS_2. No noticeable change is measured between low and high incidence angles.

2.4.7. Mueller matrix (MM) measurement

In previous results, we assume that semi-infinite thick birefringent materials with optical axes out-of-plane have zero cross-polarization components ρ_{ps} and ρ_{sp}. Experimentally, these components can be measured by using Mueller matrix (MM) formalism (a.k.a. generalized ellipsometry), which measures the complete dielectric polarization of a material [58,59].

In MM formalism, we use Stokes vector, instead of E-field vector in Jones matrix formalism, to describe the light. Stokes vector is defined as

$$S = [S_0, S_1, S_2, S_3]^T = [I, I_0 - I_{90}, I_{45} - I_{-45}, I_R - I_L]^T \quad (2.10)$$

where I is the total intensity, I_α is the intensity of the light component polarized at an angle α with respect to p-polarization, I_R and I_L are intensity of the right-hand and left-hand circular polarized light component. Comparing with Jones matrix formalism, the advantage of Stokes vector is the quantification of the degree of polarization as

$$p = \frac{{S_1}^2 + {S_2}^2 + {S_3}^2}{{S_0}^2} \tag{2.11}$$

where p = 1 for totally polarized light and p = 0 for unpolarized light. The Muller matrix M is the 4x4 matrix transforming incident light S_i to reflected light S_r.

$$S_r = M\, S_i \tag{2.12}$$

When the depolarization is 0, Muller matrix and Jones matrix could be converted to each other.

$$M = A(J \otimes J^*)A^{-1} \tag{2.13}$$

where $\otimes$ is tensor product, J is Jones matrix defined in **Equation 2.1**,

$$A = \begin{bmatrix} 1 & 0 & 0 & 1 \\ 1 & 0 & 0 & -1 \\ 0 & 1 & 1 & 0 \\ 0 & i & -i & 0 \end{bmatrix} \tag{2.14}$$

The symmetry of the M provides information about the optical symmetry of the material, such as the orientation of the birefringent optical axis relative to the incidence plane of the measurement [58,60] M provides the complete dielectric polarization of a material, and can measure cross-polarization components and depolarization effects due to surface layers[59,61]. The expected M for a birefringent material, with the optical axis parallel to plane of incidence, is shown in **Figure 2.18** (top left). Due to symmetry, certain elements are expected to be zero, while others should be repeated[58,60]. We carry out measurements on TiS_2 at AoI = 70°. With Woollam UV-NIR Vase, the last row of the M is not measurable[27]. We find that the measurements match the expected symmetry of a M corresponding to a birefringent material with optical axis in plane of incidence. Thus, the optical axis for TiS_2 points out-of-plane, with high in-plane rotational symmetry. MoS_2 also show similar behavior (measured through Semilab SE-2000, not shown here).

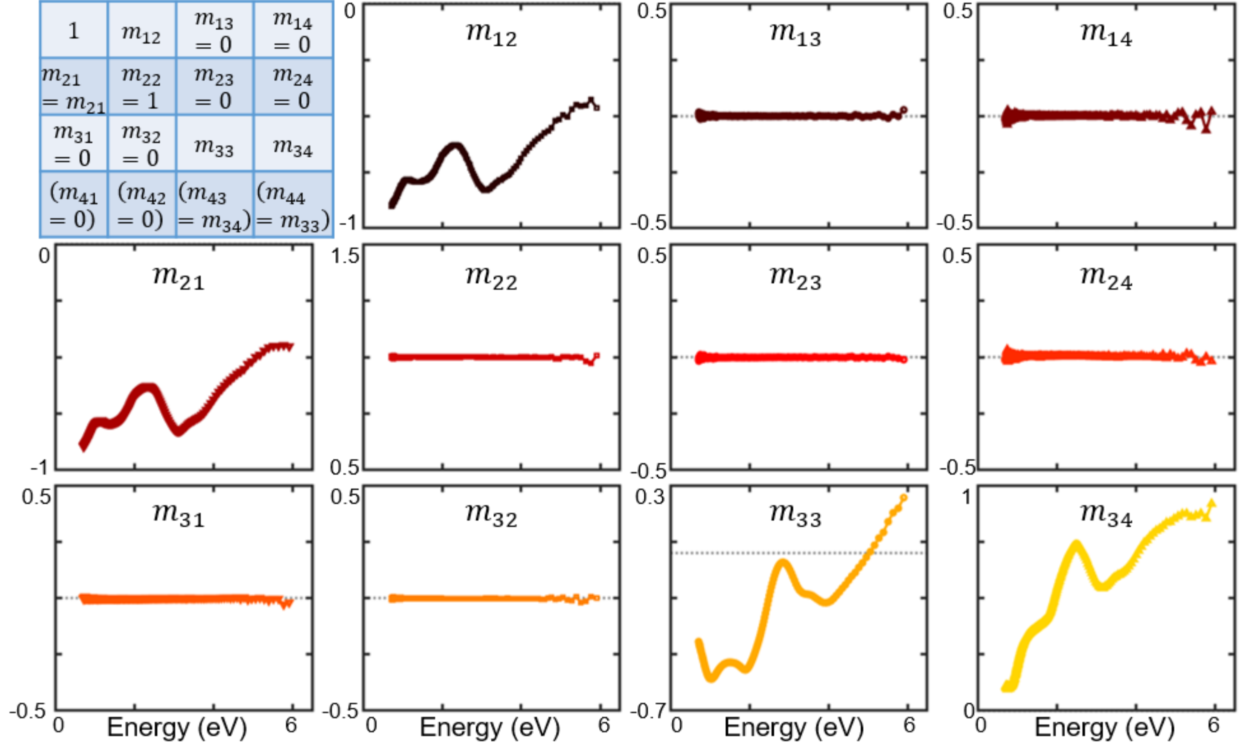

Figure 2.18: Mueller matrix (MM) ellipsometry on 1T-TiS_2. The table (top left) shows the symmetry expected from for a birefringent material with optical axis parallel to plane of incidence. The measurements (m_{12} etc.) support this symmetry. The last row of M is not measurable with the rotating compensator configuration used here. All components are normalized to m_{11}.

In the case of no depolarization, a Muller matrix M can be converted into an equivalent Jones matrix J as shown in **Equation 2.13**. This conversion $M \rightarrow J$ can be quantified with a quality factor,

$$p = \sqrt{\frac{Tr(M^T M)}{{m_{11}}^2} - 1} \tag{2.15}$$

related to degree of polarization p. We find that depolarization $1 - p$ is indeed ~ 0 for TiS_2 , as shown in **Figure 2.19a** (consistent with minimal surface roughness for TiS_2)[58,59]. Thus, the conversion $MM \rightarrow S$ can be carried out in **Figure 2.19b**. The cross-polarized (off-diagonal) components of S are ~ 0, indicating minimal polarization conversion.

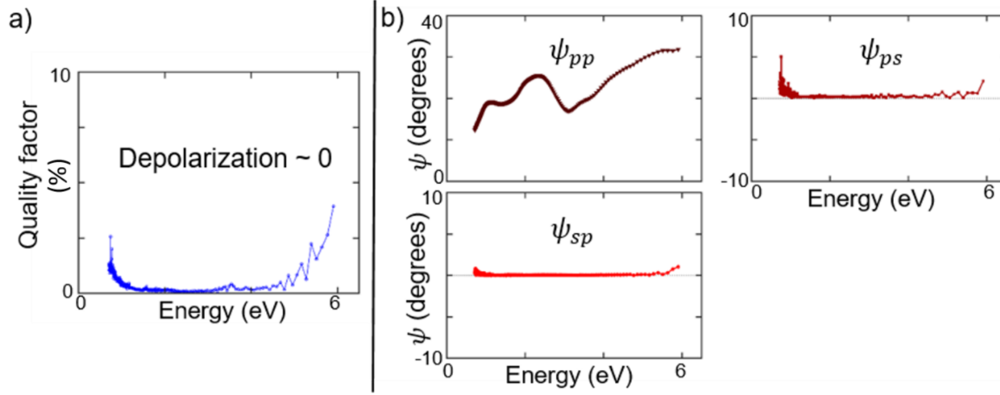

Figure 2.19: Mueller matrix (M) to equivalent Jones matrix conversion (J) for TiS_2 (AoI = 70°). (a) Quality factor quantifying the $M \rightarrow J$ conversion. The quality factor is analogous to a depolarization measurement. (b) Diagonal and off-diagonal components of equivalent S. Here, only ψ is plotted (see equation 1 of main text). All components are normalized to ρ_{ss}. Off-diagonal components are ~ 0.

2.5. Summary

We use the (Mo,W)Te_2 system as a prototype to explore the potential of TMDs as phase-change materials for integrated photonics. We find that both 2H and 1T phases have large high optical density and Δn between phases is comparable to well-establish phase change materials GST, but both phases have large optical loss, which limit the application of telluride TMDs in photonics.

We suggest that sulfur-based TMDs may be optimal for photonic phase-change applications because they have larger band gap, thus lower loss is expected. Therefore, we measure the complex optical properties of 2H-MoS_2, 1T-ZrS_2, and 1T-TiS_2, which are chosen to represent prototypes of the 2H and 1T structure types. All materials have high index of refraction ($n \sim$ 3-4), and MoS_2 and ZrS_2 feature low-loss in the NIR. We find that presence of rough surface and native oxides significantly changes the observed optical constants, which need to be characterized and modeled. Further, our DFT calculations predict a large refractive index and strong contrast in optical properties ($\Delta n \sim 1$) between the different structure (phase) types, suggesting a role for TMDs as phase-change materials for integrated photonics.

We focus on the NIR optical properties of sulfide TMDs because they offer lower optical loss (in NIR) than their selenide and telluride cousins. Unfortunately, the energetic cost of switching between phases is also highest for pure sulfides [44,46].

In next Chapter, we propose reducing switch energy by alloying sulfide TMDs. Our results from alloy $Mo_{0.91}W_{0.09}Te_2$ have already shown that the strong optical contrast between the 2H and 1T' structures persists even as the thermodynamic barrier between them is reduced by alloying. This bodes well for alloy design of phase-change materials.

Chapter 3: Alloy Design of sulfide TMDs

The chapter reproduce the our previously published work on alloy design of sulfide TMDs[18]. I contributed on the idea and the DFT calculation.

3.1. Introduction

In **Chapter 2**, our DFT calculations predict a large refractive index and strong contrast in optical properties ($\Delta n \sim 1$) between the different structure (phase) types, suggesting a role for TMDs as phase-change materials for integrated photonics.

The phase change behaviors of sulfide TMDs are not as good as their optical properties. The energetic cost of switching between phases is high for pure sulfides [44,46]. Alloying sulfide TMDs with different reference states could enable low-power switching and we have demonstrated that reducing phase change energy barrier by alloying doesn't eliminate the strong optical contrast.

However, the thermodynamics of TMD alloys are not well-established, and no phase diagrams have been published for the MoS_2-TiS_2-ZrS_2 ternary system, or the subsidiary binary systems. Here we use DFT calculations (**Section 3.2**) to evaluate the likelihood of making binary alloys near the 2H-1T phase boundary (**Section 3.3**).

3.2. Methods

3.2.1. Quasi-Harmonic Approximation (QHA) method to calculate Gibbs free energy

We calculate the Gibbs free energy of pure phases and alloys using DFT and the quasi-harmonic approximation (QHA) method, aided by Phonopy code[62–64]. We use the QHA to calculate phonon spectra, which can be approximated as quantum harmonic oscillators at fixed lattice constant, and the vibrational entropy. To this entropy we add a configurational entropy term, although this term is dwarfed by the vibrational entropy. The steps involved in phase diagram calculations are provided below:

1) Fully relaxed volume: Alloy metal sulfides are simulated in 2×2×2 (1T phase) and 2×2×1 (2H phase) supercells, thus each supercell contains 8 formula units. By varying the composition of 8 metal atoms in each supercell, 5 stoichiometries (TiS_2, $Ti_{0.75}Mo_{0.25}S_2$, $Ti_{0.50}Mo_{0.50}S_2$, $Ti_{0.25}Mo_{0.75}S_2$, MoS_2) in two phases (2H and 1T) are investigated. A Monkhorst-Pack k-point mesh of size 3×3×2 has been chosen, whose convergence has been tested up to 10×10×5. Each supercell is fully relaxed without any symmetry constraints by the conjugate gradient method, and the initial positions of ions are manually perturbed to promote the gradient descent.

2) Relaxation with Fixed volume: At given phase and stoichiometry, every fully relaxed supercell is strained by 0.5% in each vector, up to 2.5% in both compression and tension, to generate 11 different volume points. Each point is relaxed under similar condition but with fixed volume.

3) Phonon spectra: Under fixed phase, stoichiometry and volume, the dynamical matrix of each supercell is calculated by Parlinski-Li-Kawazoe method, combining the DFT simulation results of a set of displaced supercells in which one ion is displaced by 0.01 Å. The phonon spectra and density are derived by solving non-zero eigenvalue dynamical matrices. Then Helmholtz free energy (F) is the direct result of the partition function (Z) of phonon vibrations:

$$Z = \prod_{qv} \frac{\exp(-\hbar\omega(qv)/(2k_B\,T))}{1-\exp(-\hbar\omega(qv)/(k_B\,T))} \tag{3.1}$$

$$F = -k_B T \ln Z = \frac{1}{2}\sum_{qv} \hbar\omega(qv) + k_B T \sum_{qv} \ln\left[1-\exp\left(-\frac{\hbar\omega(qv)}{k_B T}\right)\right], \tag{3.2}$$

where q is the wave vector and ν is the band index. All the phonon spectra calculations use 15×15×15 q-point mesh.

4) Calculate the Gibbs free energy: Gibbs free energy (at given phase and stoichiometry under 0 Pa pressure) are calculated by minimization of the sum of Helmholtz free energy and pV, which only depends on volume under fixed temperature, as shown in **Figure 3.1**.

$$G(T,p) = \min_{V}\left[U(V) + F_{phonon}(T,V) + pV\right], \tag{3.3}$$

where $U(V)$ is the DFT calculated ground state energy. The configuration entropy term from Mo-Ti alloy is also added to the final results, but the contribution is in the scale of 0.1 eV, which is negligible.

$$S = -k_B \sum_{n=1}^{W} P_n \ln P_n \tag{3.4}$$

The contribution of pV term is also negligible since it is ~ 1 meV when pressure ~ 1 atmosphere.

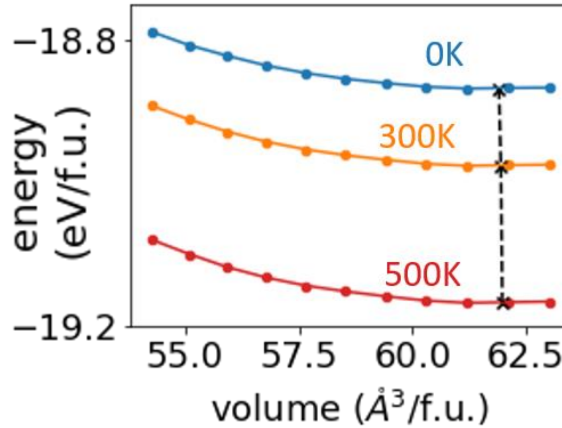

Figure 3.1: Minimizing the function of volume to find Gibbs free energy of 2H $Mo_{0.5}Ti_{0.5}S_2$ under given temperature and atmosphere pressure (1 atm). The energy-volume curve for each temperature is fitted from DFT-calculated total Helmholtz free energy plus pV term under given temperature, fixed pressure and varied volumes. Gibbs free energy under fixed pressure and given temperature is determined by the minimum of the fitted curve and marked as 'x'.

3.2.2 Parameters

We use Vienna ab-initio simulation package (VASP), version 5.4[36–39]. We treat the core and valence electrons by the projector-augmented plane-wave method, and we approximate the exchange-correlation interaction by the generalized gradient approximation functional,

implemented in the Perdew-Burke-Ernzerhof form[40,41]. The energy minimization and force convergence criteria are 10^{-7} eV and 10^{-3} eV/Å, respectively.

3.3. Results and Discussion

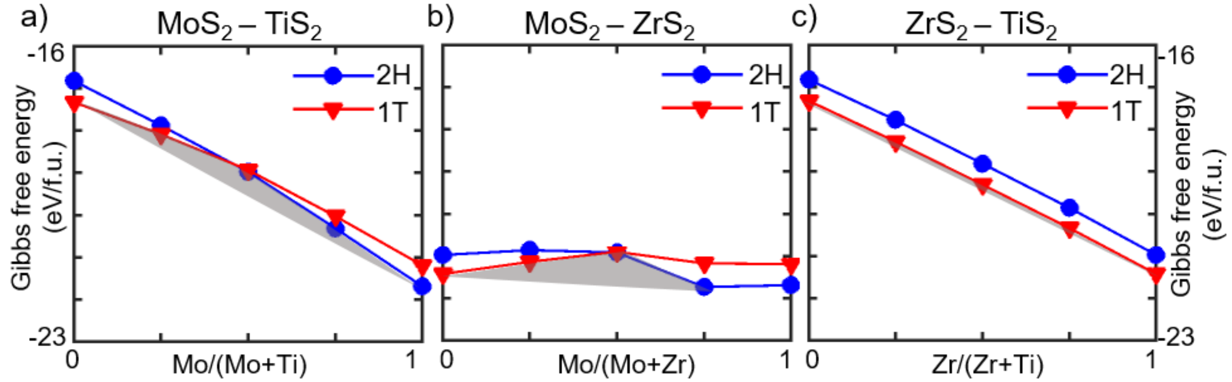

Figure 3.2: Theoretically-predicted Gibbs free energy-composition plots for the (a) MoS_2-TiS_2, (b) MoS_2-ZrS_2, (c) ZrS_2-TiS_2 systems at 300 K. In the first two cases the alloys are thermodynamically unstable relative to decomposition into pure phases. However, the free energy above the convex hull (grey zone) is small, which suggests that kinetic stabilization will be possible, e.g., through low-temperature processing. ZrS_2-TiS_2 system is expected to form stable alloy solutions.

In **Figure 3.2** we show the calculated Gibbs free energy-composition curves for the MoS_2-TiS_2 and MoS_2-ZrS_2 systems at 300 K. The results are very similar at 1000 K (not shown here), although with an overall downward shift of ~ 1 eV/f.u (formula unit) relative to the data at 300 K. For both systems, the free energy curves for the 2H and 1T phases cross at an intermediate composition, which is suggestive of a phase boundary. For the MoS_2-TiS_2 system the curves are concave-downward and lie above the convex hull, which for this system is a straight line connecting the pure phases. Therefore, MoS_2-TiS_2 alloys will have a tendency to phase-separate at equilibrium. For the MoS_2-ZrS_2 we predict a solid solution in the 2H structure for $Mo_xZr_{1-x}S_2$, $x > 0.75$, and phase separation for more Zr-rich compositions. For both of these systems, the relatively small energy difference between the alloy curves and the convex hull (< 1 eV/f.u.) suggests that alloys may be kinetically-stabilized near the 2H-1T phase boundary. The ZrS_2-TiS_2 system is likely to be stable as a solid solution in the 1T phase, for which we don't calculate a significant positive

enthalpy of mixing, and therefore don't expect to observe spinodal decomposition. Future work should consider metastability and the kinetics of phase separation in TMD alloys systems, and a particular focus on low-temperature processing of TMD alloy thin films.

3.4. Summary

In **Chapter 2**, our DFT calculations predict a large refractive index and strong contrast in optical properties ($\Delta n \sim 1$) between the different structure (phase) types, suggesting a role for TMDs as phase-change materials for integrated photonics. Achieving this goal will require making materials that are thermodynamically-adjacent to a phase boundary. For sulfides this will likely require alloying. We use DFT to calculate free energy-composition curves for alloys of MoS_2, ZrS_2, and TiS_2. The alloy structural phases become energetically degenerate at intermediate compositions, at which martensitic switching may be possible, if the alloys are found to be metastable or kinetically-stable.

In the following **Chapter 4** about TMD synthesis, we will focus on $(Mo,Ti)S_2$ system.

Chapter 4: TMD synthesis

The chapter reproduce our previously published work on MoS_2 and TiS_2 film synthesis and publishing work on $(Mo,Ti)S_2$ film synthesis[65,66]. I contributed on the film synthesis and most of film characterization except electron microscopy.

4.1. Films for photonic integrated circuits (PIC) application

We design for relatively thick (over 10 nm) and nanocrystalline films. The film thickness, much larger than monolayer and few-layer films that are emphasized for TMD optoelectronics and microelectronics, is chosen to enhance the optical interaction volume in PIC devices, as we have demonstrated through numerical simulation[67].We also claim that nanocrystalline, dense films may be preferable to single-crystal films for phase-change functionality in PIC applications: grain boundaries make a much smaller contribution to parasitic, below-band gap optical loss than do chemical impurities, and nanocrystalline material may have lower kinetic barriers to phase-change behavior than single crystals, as is known in traditional phase-change chalcogenides (*e.g.*, Ge-Sb-Te compounds).

Low process temperature is another priority in synthesis. TMD film deposition methods often require high temperature, due to various factors, including the high melting point of refractory transition metals, and the often-sluggish kinetics of replacing metal-oxygen bonds by metal-chalcogen bonds (MoS_2 is a notable exception to this trend)[68]. Lower process temperature may be essential for integration to avoid thermal damage to other materials and structures, especially for vertically integrated devices where other low-dimensional materials can be interfaced[69,70]. Lowering the process temperature may also widen the scope of materials available through alloy design. As we will discover in later sections, stabilizing TMD alloys, avoiding segregation,

achieving smooth and uniform surface morphology during growth further motivates the drive toward lower processing temperature.

4.2. Method

4.2.1. Two-step method

In the Chapter, we will discuss the thin film synthesis of MoS_2 (**Section 4.3**), TiS_2 (**Section 4.4**) and alloy $(Mo,Ti)S_2$ (**Section 4.5**) via two-step method, which is depositing transition metal thin films (thickness < 20 nm) by physical vapor deposition (PVD) and sulfurizing the metal films in the H_2S environment in our own chemical vapor deposition (CVD) style furnace. Metal thin-film PVD and H_2S processing are industrially-scalable methods. Although MoS_2 films obtained by sulfurization of Mo metal films have small grain size and likely will never match the crystalline quality of films obtained by high-temperature MOCVD, the two-step approach is of interest for applications where cost, flexibility, throughout, and large-area uniformity are higher priorities than crystal quality.

We have tried substrates including SiO_2, Si_3N_4, Si, glass, ITO, sapphire and metal sheet, with and without sequential pre-clean treatments with methanol, acetone and isopropyl alcohol. MoS_2 could be deposited on various substrates, with fine thickness control by tuning the thickness of Mo precursor. For the TMDs containing Ti, we choose Si_3N_4/Si as substrate for future photonic integration and avoid the oxide substrates which could be a secondary oxygen source during sulfurization.

We deposit polycrystalline thin films of Mo, Ti and their alloys by sputtering and electron-beam (E-beam) deposition, using AJA international Orion 5 magnetron sputtering (base pressure 10^{-5} Torr, process pressure 10^{-3} Torr), AJA electron-beam evaporator system (UHV), and an electron-beam source (Telemark) in our own Mantis Deposition molecular beam epitaxy (MBE)

chamber (base pressure 10^{-9} Torr, process pressure 10^{-8} torr). These PVD methods are standard in industry with large full-area coverage, high scalability and established patterning techniques. All metal thin films are deposited under room temperature with smooth surface (roughness approximately 3 Å).

During deposition, the deposition rate and film thickness are controlled by quartz crystal monitors (QCM) in all 3 PVD instruments. Post-deposition thickness is measured by X-ray reflectivity (XRR) on a Bruker D8 diffractometer and Profilometry Bruker DXT Stylus Profilometer. In the deposition involving Ti, we use the density of Z-factor of Ti metal as parameters for QCM. However, as we will discuss further in **Section 4.4**, Ti is very sensitive to the O_2 even in the vacuum environment. Therefore, the so-called deposited metal film contains certain amount of partial oxide TiO_x, as shown in **Figure 4.1**. We want to clarify that although the metal precursor has the composition of $TiO_{1.5}$ according to X-ray Photoelectron Spectroscopy (XPS), but the film could be oxidized during the deposition and post-deposition and XPS results emphasize the signals from the surface oxide even after depth profiling. Thus, we can't determine exact partial oxide composition for QCM calibration. Lacking reliable parameters for TiO_x, we have to treat the film as pure metal, which introduces system error. The post-deposition methods are subject to systematic errors as well: XRR data analysis can be complicated by finite film roughness and thickness-dependent layer density, whereas profilometer requires extra procedure patterning and the accuracy is low for thin film with thickness less than 10nm.

To synthesize alloy $Mo_xTi_{1-x}S_2$, we deposit the Mo-Ti alloy metal thin film precursor by co-sputtering. The composition is by controlled by calibrating deposition rate of each metal source separately by quartz crystal monitor (QCM) before co-sputtering. The system error of QCM due to the oxidation of Ti propagates. The post-synthesis (after sulfurization) elemental analysis after

the sulfurization is done by quantization of the electron dispersive spectroscopy (EDS) mapping of the cross-section sample. However, EDS can only characterize the continuous film part of the sample, as we will discuss further in **Section 4.5**.

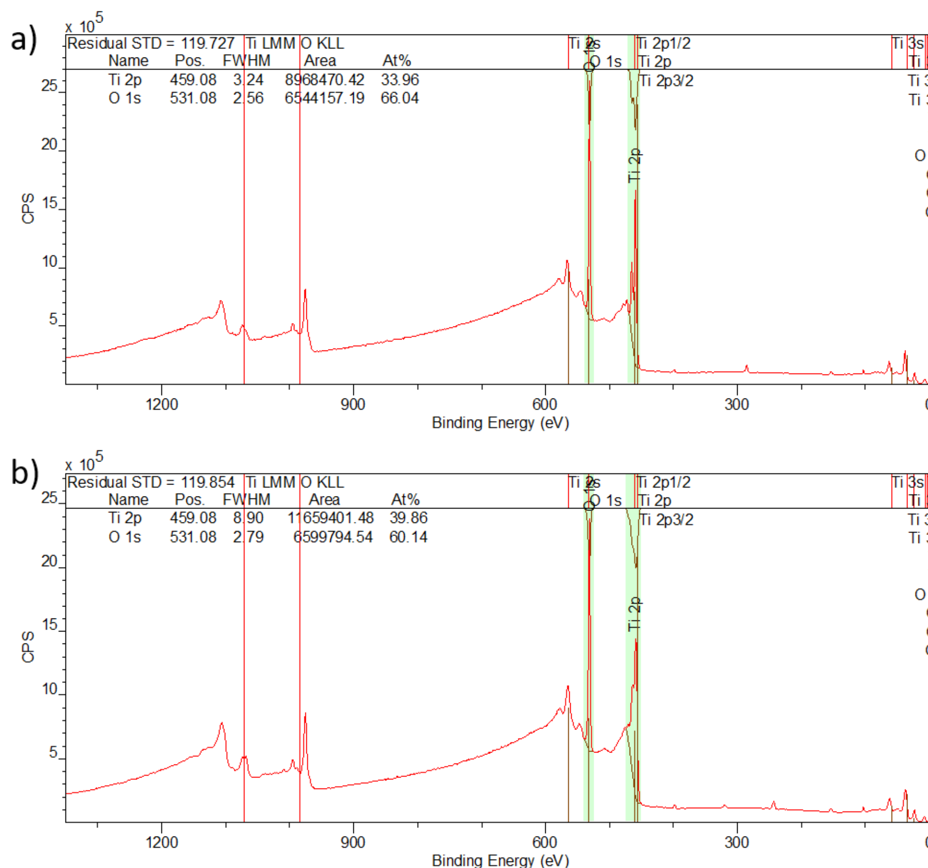

Figure 4.1: X-ray photoelectron spectroscopy (XPS) survey-scan data measured on the TiO_x precursor film corresponding to the TiS_2 film presented in **Figure 4.7**. (a) The composition at the surface after deposition and exposure to air is close to TiO_2. (b) The composition within the film, after ion etching (parameters), is close to $TiO_{1.5}$.

We sulfurize metal precursors in H_2S environment in our own CVD style hot-wall tube furnace reactor, as shown in **Figure 4.2**. Comparing to conventional methods using sulfur solid source, our gas source method is more scalable, controllable and consistent. The tube furnace runs under low pressure (base pressure ~ 0.1 Torr) and atmospheric pressure with temperature up to 1000°C. The mass flow controllers (MFCs) provide the flow of O_2, H_2S and H_2Se up to 100 sccm, Ar, N_2 and forming gas (FM gas, 5% H_2, 95% Ar) up to 1000 sccm.

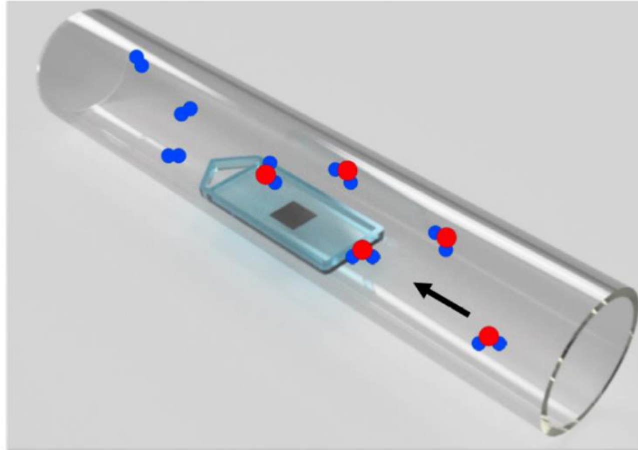

Figure 4.2: A schematic of sulfurization process. Pre-deposited metal (silver) is loaded at the center of 3-inch (or 1.5 inch) quartz tube. Black arrow indicates the direction of H_2S gas flow. Thermally decomposed sulfur (S) reacts with the metal thin film to form TMDs thin film. Red: S atom, Blue: H atom.

The sulfurization process generally consists of 4 steps, as shown in **Figure 4.3**. After loading the sample, we purge the tube with FM gas under the room temperature to reduce the residual O_2 introduced during loading process. Then we purge the tube with H_2S gas under room temperature to build up partial pressure for reaction. Therefore, the tube ramps up (~10°C /min) to process temperature in H_2S environment and holds for 0-36h during heating step. The furnace could be cooled down by natural cooling (simply stop heating) or quench cooling (expose quartz tube outside wall to the ambient). Due to the large thermal mass and low thermal leak rate, the natural cooling of the furnace from 500°C to 300°C (too low for reaction) takes more than 5hrs, while the quench cooling takes only seconds. In either way, the samples are cooled in H_2S environment to avoid post-oxidation.

We expect a volume expansion (~3 times) of film during the sulfurization. Since the area is restricted by the substrate, the major expansion is on thickness, with the ratio 3.36 for pure Mo and 3.26 for pure Ti.

The conditions to sulfurize Mo and Ti are highly distinct. For pure Mo metal films, we vary O_2 concentration (0-10 sccm) and process temperature (350-500°C) under low pressure to explore

the effects of O_2 on the kinetics of MoS_2 formation. For precursors containing Ti, we sulfurize the precursors under atmospheric pressure, in a flow of between 20 – 100 sccm H_2S and 0 – 200 sccm forming gas (5% H_2, 95% Ar or N_2) to minimize background O_2 level, at temperature up to 900 °C. The condition to sulfurize Mo-Ti alloy is similar to ones of Ti to make sure both are sulfurized.

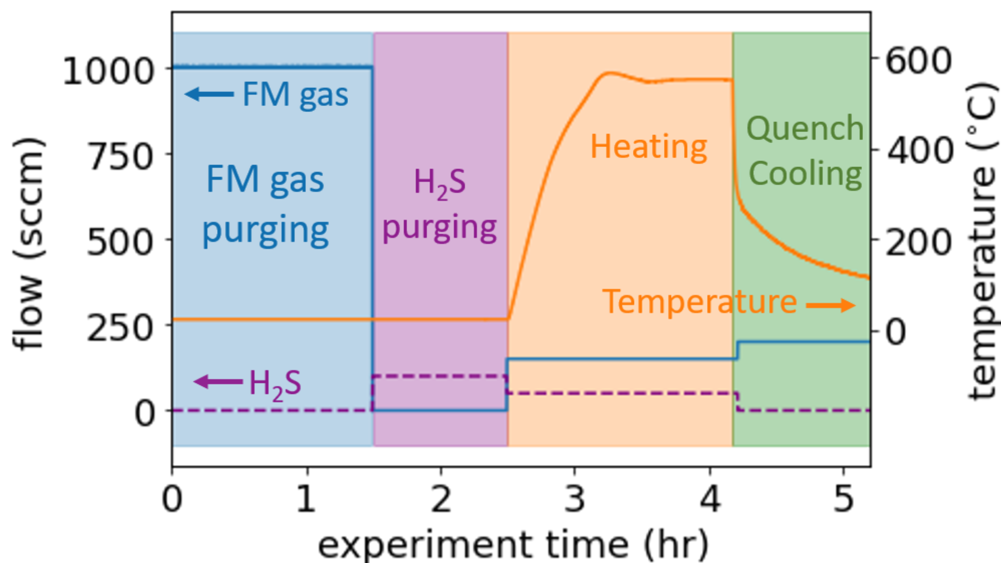

Figure 4.3: Temperature time curve and flow rate time curves of a generic sulfurization process.

Controlling O_2 concentration is essential in our experiments. The leak rate for 3-in tube from the ambient into the reactor under vacuum is <1 sccm, corresponding to <0.2 sccm of O_2. We determined this leak rate by analyzing steady-state and transient-rise pressure data under varying gas flow conditions. Therefore, the total flow of O_2 into our reactor is the flow controlled by the O_2 mass flow controller (MFC), plus this extra leak rate. We use an assortment of techniques including modification of equipment, process, and samples to control the level of trace oxygen in the furnace, and we measure the oxygen level using an electrochemical sensor (Southland Sensing TO2-1x ppm), as discussed in **Section 4.5**.

4.2.2. Characterization

We characterize the elemental composition of our films using X-ray photoelectron spectroscopy (XPS) and X-ray fluorescence (XRF). We recognize phase with Raman spectroscopy and X-ray diffraction (XRD). We explore the film morphology using atomic force microscopy (AFM), scanning electron microscopy (SEM) in plan-view geometry, transmission electron microscopy (TEM) in both plan view and cross-section geometry, and four-dimensional scanning transmission electron microscopy (4D STEM). We measure the optical properties of the films by Ellipsometry (SEMILAB SE2000). The detailed measurement parameters depend on specific films and will be discussed in following sections.

4.3. The formation of large-area MoS_2 thin films by oxygen-catalyzed sulfurization

This work is mainly done by my colleague Dr. Seong Soon Jo and I contributed on the idea and establishing two-step method for MoS_2 at early stage[65]. Since the synthesis of MoS_2 has been widely achieved in the field, we will introduce the results briefly.

In this work, we find that adding trace quantities of O_2 during sulfurization accelerates MoS_2 crystallization at reduced temperature, without affecting sulfur diffusion or overall film composition; O_2 also affects the MoS_2 layer orientation. The presence of O_2 does not affect mass transport, such as sulfur diffusion into the film. It does not affect the conversion of Mo from the 0 to the +4 oxidation state, or even the formation of Mo-S bonds. It seems that O_2 specifically catalyzes the formation of Mo-S-Mo bridging bonds, as suggested by molecular dynamics simulations[71], thereby building the backbone of crystalline 2H-MoS_2. The catalytic effect of O_2 accelerates the formation of 2H-MoS_2 at processing temperatures below 400 ℃.

Our two-step synthesis method allows us to grow large area MoS_2 thin films on various substrates, and to control the thickness of MoS_2 by tuning the thickness of Mo precursor. We demonstrate fully-sulfurized MoS_2 films made using thin metal precursors. In **Figure 4.4a** we show a MoS_2 film deposited across a 2-inch wafer. The Mo metal precursor film is 1 nm thick,

and is sulfurized under 20 sccm H_2S and 5 sccm O_2 gas flows at 400 ℃. XPS depth profiling shows that the films are uniformly sulfurized throughout. The same process can be used to make large-area MoS_2 films on various substrates; in **Figure 4.4b** we show films grown on Al, glass, and indium tin oxide (ITO). In all cases we confirm the MoS_2 phase identity using Raman spectroscopy, as shown in **Figure 4.4c**.

The two-step method produces films that are smooth and continuous. The process relies on PVD and gas-source sulfurization, and therefore is inherently scalable to wafer-scale and compatible with industrial coating. The crystal quality (*e.g.* grain size) of MoS_2 films made by metal sulfurization likely will never match that of films obtained by high-temperature MOCVD. However, the two-step approach may be of interest for applications where cost, flexibility, throughout, and large-area uniformity are higher priorities than crystal quality. Further research on catalysts for the formation of MoS_2 and other TMDs by metal sulfurization at low temperature may create new possibilities for industrial applications, such as electrochemical hydrogen evolution.[72,73]

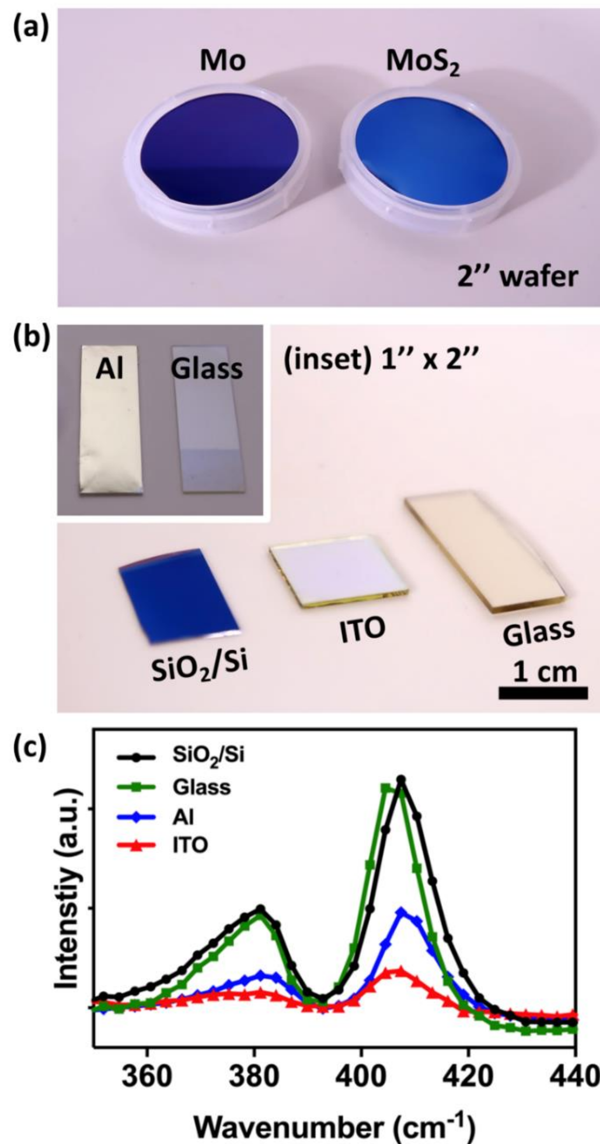

Figure 4.4: Making large-area MoS_2 thin films on various substrates by a low-temperature process catalyzed by oxygen. In all cases films are made by sulfurizing a 1 nm-thick Mo metal film under 20 sccm H_2S and 5 sccm O_2 at 400 °C. (a) Photograph of as-deposited 1 nm Mo metal precursor film and a post-sulfurization MoS_2 film on 2-inch SiO_2/Si wafers. (b) MoS_2 films on various substrates. From left to right: SiO_2/Si, ITO and glass. (Inset) Fully-covered, large-area MoS_2 on Al and glass substrates. (c) Raman spectra of MoS_2 grown on SiO_2/Si (black), glass (green), Al (blue), and ITO (red), respectively.

4.4. Making Large-Area Titanium Disulfide Films at Reduced Temperature by Balancing the Kinetics of Sulfurization and Roughening

4.4.1. Introduction

In this section, we report the synthesis of large-area, single-phase 1T-TiS_2 films via a two-step method with sulfurization temperature as low as 500 °C and the roughening mechanism during sulfurization.

4.4.2. Experimental Techniques

We deposit precursor Ti thin films (thickness < 10 nm) by AJA international Orion 5 magnetron sputtering (base pressure 10^{-5} Torr) on Si/SiO_2, SiN and sapphire substrates. Titanium oxidizes quickly, even in the high vacuum environment of PVD tools. Therefore, our precursor films are chemically TiO_x, and with roughness approximately 3 Å. We measure precursor film thickness during deposition using a QCM, using settings for Ti metal, and post-deposition using XRR on a Bruker D8 diffractometer. Each of these methods is subject to systematic errors: for QCM we use the material parameters for Ti metal, lacking reliable parameters for TiO_x, whereas XRR data analysis can be complicated by finite film roughness and thickness-dependent layer density. We perform sulfurization in a hot-wall tube furnace reactor at atmospheric pressure, in a flow of between 20 - 100 sccm H_2S and 0 - 200 sccm forming gas (5% H_2, 95% Ar), at temperature up to 900 °C. We use an assortment of techniques including modification of equipment, process, and samples to control the level of trace oxygen in the furnace. Based on the tube furnace we used in **Section 4.3**, we welded all unnecessary metal-to-metal seals to minimize the leaking rate and made a N_2 gas jacket to purge the metal-quartz seals and suppress O_2 leaking to the tube during experiments as shown in **Figure 4.5**. We optimize the process by purging the tube with FM gas before experiments and only ramping the tube in H_2S environment. The modifications of samples include using nitride substrates and cap the precursors with Mo layer. The oxygen level is measured by an electrochemical sensor (Southland Sensing TO2-1x ppm). The O_2 sensor is installed at the downstream of the quartz tube, as shown in **Figure 4.6**, and can only work under

room temperature, atmospheric pressure, and inert gas environment (low O_2 concentration and no H_2S). Therefore, all the O_2 levels reported are measured under the different conditions from that the sulfurization experiments run and we assume the levels are similar. To measure the O_2 levels, we purge the tube with 1000 sccm FM gas for 12 hrs, then flow 200 sccm FM gas and open the valve to connect tube and O_2 sensor, and read value at the steady state.

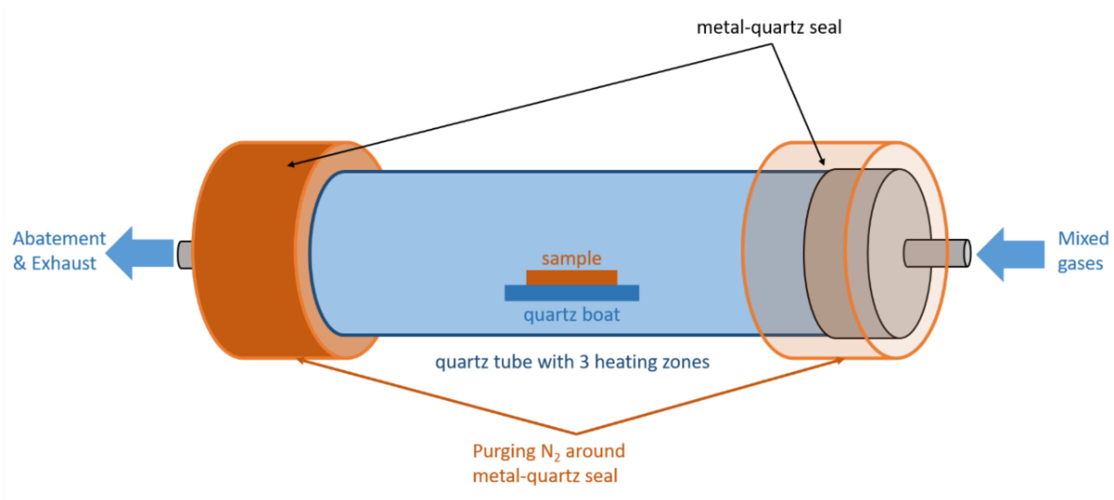

Figure 4.5: Schematic of N_2 gas jackets around metal-quartz seals to reduce O_2 partial pressure around the seals, thus the O_2 leaking to the tube is suppressed.

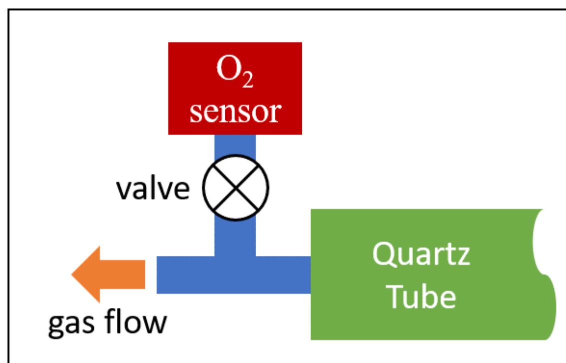

Figure 4.6: Schematic diagram of installing O_2 sensor on the tube furnace. The valve can only be opened when the environment is inert gas under atmospheric pressure and room temperature.

We characterize the elemental composition of our films using X-ray photoelectron spectroscopy (XPS) (Thermo Scientific K-alpha+, Al Kα source). We determine phase by Raman spectroscopy (Renishaw Invia Reflex Micro Raman) with excitation wavelength 532 nm. We use

atomic force microscopy (AFM, Veeco Dimension 3100) to characterize film morphology. We perform transmission electron microscopy (TEM) measurements in both plan view and cross-section geometry. For plan view measurements we grew samples directly on a TEM grid with 50 nm-thick amorphous SiN membranes (Norcada), and we imaged samples using a 200 kV field-emission TEM (JEOL 2010F). For cross-sectional TEM, we prepare samples using a focused ion beam (Helios Nanolab), as described elsewhere.[74]

4.4.3. Synthesized TiS_2 film

Here we report the synthesis of large-area TiS_2 films using a two-step method of metal deposition by physical vapor deposition (PVD), followed by sulfurization in H_2S gas in a hot-wall tube furnace reactor. This approach is reliable and scalable, since it uses industrially-compatible methods that are easy to implement for large wafers. However, Ti metal is extremely prone to oxidation, and Ti metal films deposited by PVD are more accurately described as TiO_x. Therefore, competition between S and O for Ti bonding orbitals is a central issue. In **Figure 4.7** we show the crystal structures of 1T-TiS_2, selected Ti oxides, and Ti metal. We also show a Richardson-Ellingham diagram for the Ti-O and Mo-O systems. This diagram highlights the extremes of oxygen activity control that are required to avoid Ti oxidation. In contrast, molybdenum oxide does not present an obstacle to the formation of 2H-MoS_2, and may even be a catalytic intermediate.[65,71,74] The Richardson-Ellingham diagram represents thermodynamic equilibrium and does not consider TMDs as competing phases, whereas thin film processing is inherently non-equilibrium, and the reacting components in our process include Ti, O, S, and H. Therefore, the oxygen partial pressures indicated in the Richardson-Ellingham diagram are not likely achieved in our process, even in close vicinity to the reacting film. Nevertheless, the Richardson-Ellingham diagram portrays the substantial barrier that Ti-O bonds pose for TiS_2 formation.

In general, high temperature and a highly-reducing environment are needed to substitute S for O and form TiS_2[75–77]. In addition to problems with integration, high temperature can lead to film breakup through coarsening, resulting in rough and non-continuous films. Here we find that the process temperature for TiS_2 film formation can be systematically reduced by lowering the level of trace oxygen in the sulfurization process. We are able to achieve large-area and uniform films of 1T-TiS_2 at process temperature as low as 500 °C, with further gains likely through continued improvement in oxygen control.

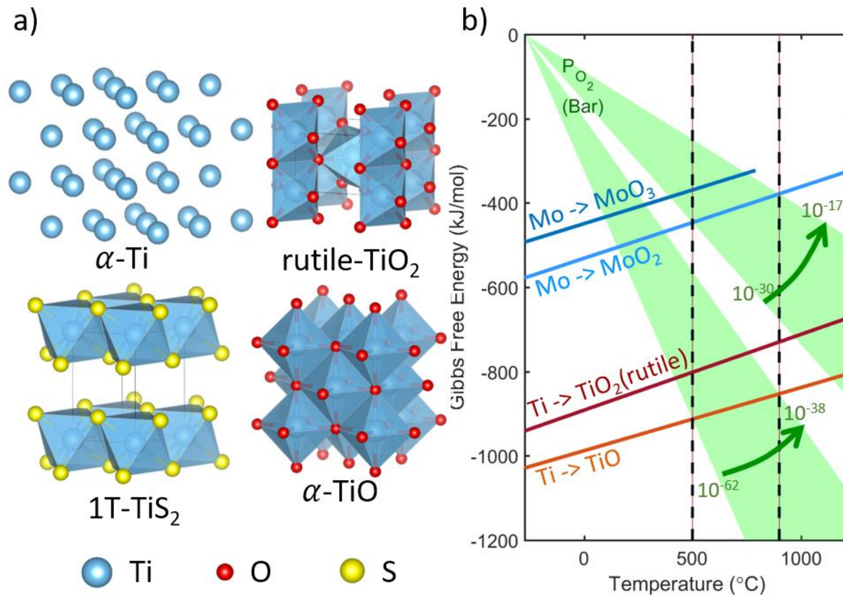

Figure 4.7: The challenge of out-competing Ti oxidation to make TiS_2 films. (a) Crystal structures of α-Ti, 1T-TiS_2, α-TiO, and rutile-TiO_2[78–81]. (b) Richardson-Ellingham diagram illustrating the extreme low values of oxygen activity (represented here by P_{O2}, labeled in green) needed to suppress Ti oxidation. We also show data for Mo oxidation.

In **Figure 4.8** we show characterization of a typical TiS_2 film sulfurized at 600 °C. For this film the precursor thickness was 3 nm, measured by quartz crystal monitor (QCM), and the final TiS_2 film thickness was 10 nm. The characteristic Raman peaks corresponding to the E (332 cm^{-1}) and A_1 (230.5 cm^{-1}) phonons of 1T-TiS_2 are well-defined, and we observe no Raman peaks from competing phases, including the tri-sulfide TiS_3 that sometimes results from low-temperature

synthesis[82]. XPS spectra show that the film consists of Ti and S with ratio about 1:2, but also indicate a significant level (*ca.* 10 at. %) oxygen remaining in the film. Since no second crystalline phase is recognized by Raman, XRD, or TEM (below), the oxygen may be incorporated as defects in TiS_2, or in intergranular, amorphous regions. Quantifying the oxygen-to-sulfur ratio using XPS data results in substantial overestimating systematic error, due to differential re-sputtering during depth profiling, and also due to the near-100% sticking coefficient of background oxygen in the XPS chamber, which is significant even at ultra-high vacuum.[83]

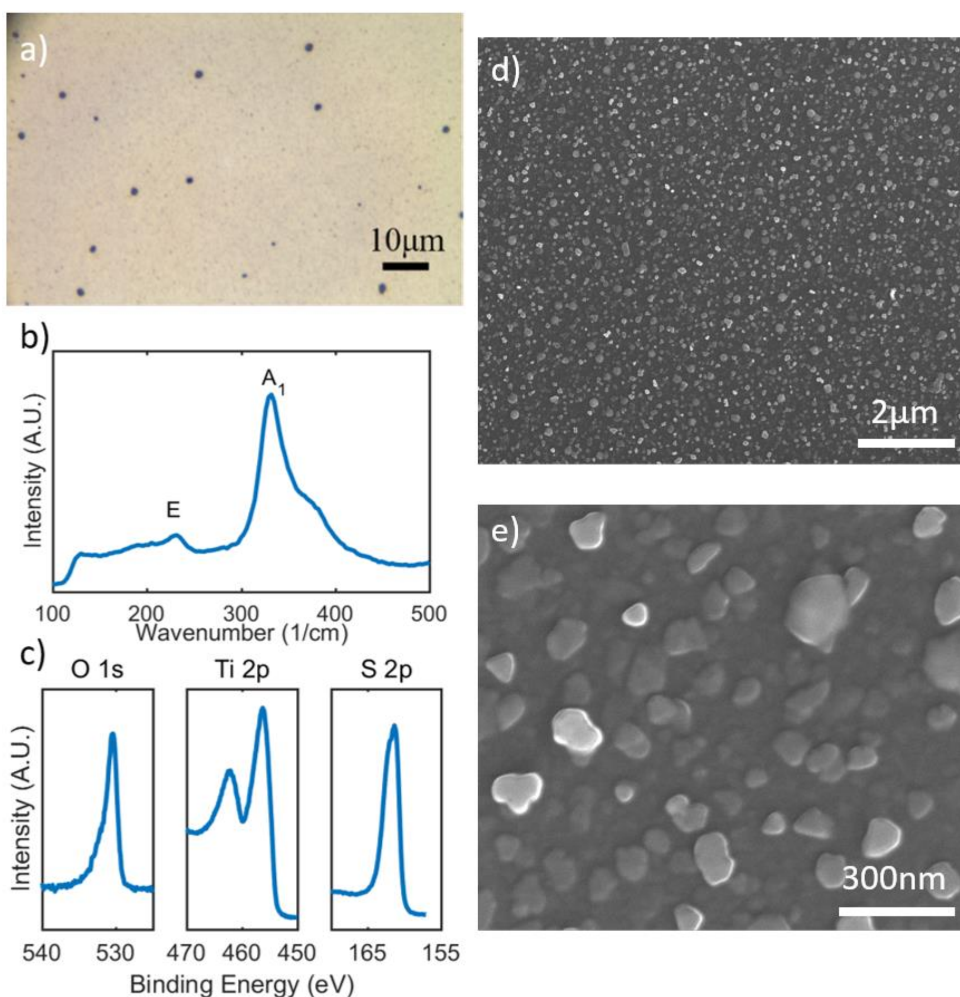

Figure 4.8: Characterization of a typical TiS_2 film sulfurized at 600°C. (a) Optical micrograph. (b) Raman spectra showing characteristic modes E and A_1. (c) XPS spectra measured on ion-beam cleaned surface. The Ti 2p and S 2p scan confirm the existence of TiS_2, but the O 1s scan indicates substantial oxygen content remaining. (d) and (e) SEM plan-view images at two magnifications.

4.4.4. The correlation of O_2 background levels, process temperature and morphology

The film morphology depends strongly on the sulfurization temperature. Higher-temperature sulfurization results in substantial grain growth and eventually to the formation of disconnected TiS_2 crystals. Lower-temperature sulfurization preserves the planar morphology, and results in smaller grains and smoother films. We find that lowest-achievable sulfurization temperature depends strongly on the level of trace oxygen in the sulfurization process. Therefore, the process temperature and film morphology depend strongly on the oxygen background.

In **Figure 4.9** we show results of TiS_2 films sulfurized at three different temperatures, between 900 and 500 °C and three different oxygen background concentrations, between 4400 and 25 ppm. With a background oxygen concentration of 4400 ppm, a high temperature of 900 °C is required for sulfurization and TiS_2 formation, resulting in substantial coarsening. The resulting sample is no longer a film but a series of isolated TiS_2 particles (**Figure 4.9a**), and the Raman spectra are position-dependent (**Figure 4.9d**). We can reduce the background oxygen concentration by installing N_2 gas jackets around the compression seals on our tube furnace, to reduce the O_2 leak rate from the atmosphere. We also deposit a thin gas barrier layer of Mo metal (1 nm) on top of the Ti metal (3-10 nm) precursor, in the same deposition chamber, to reduce the rate of Ti metal oxidation during sample transfer. With these changes, the background oxygen concentration is 200-1000 ppm (varies throughout the sulfurization process), and we can achieve sulfurization at 700 °C. The resulting film is continuous, although sizeable particles are visible under an optical microscope (**Figure 4.9b**). The Raman spectra confirms the presence of 1T-TiS_2 and 2H-MoS_2, as expected (**Figure 4.9d**). We can further reduce the background oxygen concentration by extensive purging of the tube before heating, and co-flowing forming gas with H_2S during sulfurization. With these changes, the background oxygen concentration is 25 ppm, and we can achieve

sulfurization at 500 °C. In **Figure 4.9c-d** we present results for a film sulfurized at 500 °C without a Mo barrier layer. The film is optically-smooth and the Raman spectra confirm the 1T-TiS_2 phase. For comparison we also present results for a film sulfurized at 500 °C without the described steps to reduce background oxygen concentration. In this case the TiO_x precursor film remains smooth (**Figure 4.9e**) and the Raman spectra show no signature of TiS_2 (**Figure 4.9f**). The results presented in **Figures 4.8-9** clearly show that reducing background oxygen is an effective route to producing large-area and uniform TiS_2 thin films by metal sulfurization.

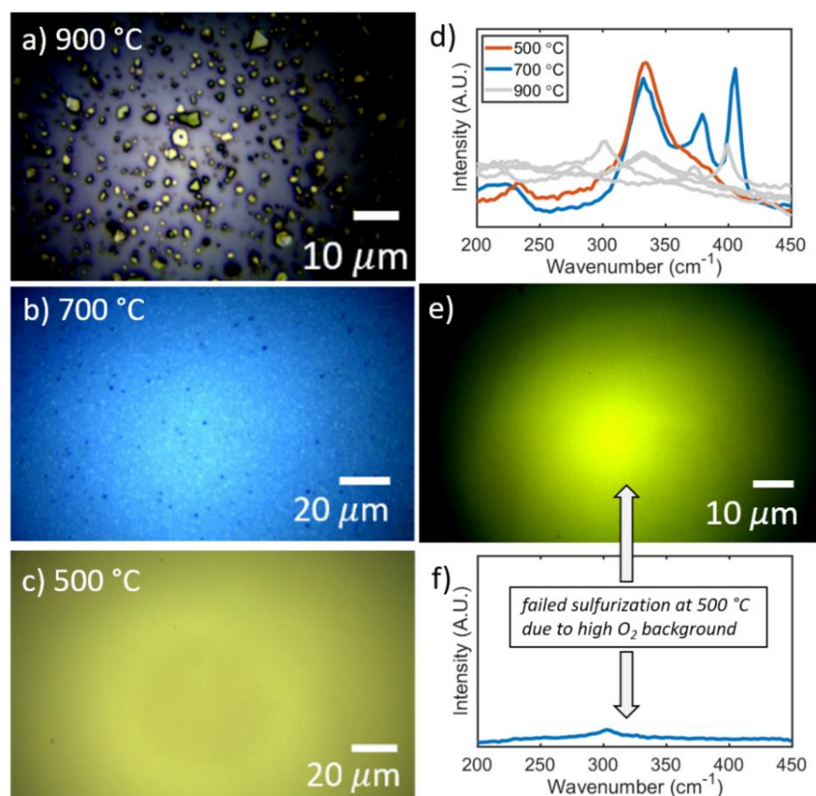

Figure 4.9: Lowering the sulfurization temperature - thereby improving film morphology – by reducing background oxygen concentration. (a-c) Optical micrographs of samples sulfurized in three different conditions. (a) Sulfurization at 900 °C for 24 h results in growth of discontinuous, faceted 1T-TiS_2 crystallites. (b) Sulfurization at 700 °C for 2.5 h results in a continuous film with particles visible. (c) Sulfurization at 500 °C for 4 h results in an optically-smooth film. (d) Raman spectra for the samples shown in (a-c). The spectra for the sample processed at 900 °C is position-dependent; we present data from several positions. The MoS_2 peaks (380 and 405 cm^{-1}) for the samples processed at 700 °C and 900 °C are due to the use of a Mo gas barrier layer. (e) Optical micrograph and (f) Raman spectra showing failure of

sulfurization at 500 °C for 4 h with insufficiently-reduced O_2 background. The color difference between the different micrographs is due to slightly different film thickness, and lamp changes between experiments.

We also note that the Mo barrier layer, used for the sample sulfurized above 700 °C as reported here, is no longer needed to assist TiS_2 formation for sulfurization temperature below 600 °C. This implies that the role of the Mo barrier layer is to slow the formation of new Ti-O bonds in the furnace during sulfurization, rather than to slow Ti oxidation during sample transfer. For sufficiently low background oxygen concentration in the sulfurization furnace, this barrier layer is no longer needed.

4.4.5. The roughening mechanism

We turn to TEM to understand the mechanism of sulfurization and film roughening. In **Figure 4.10** we show plan views of a film sulfurized at 600 °C and a cross-section view of a film sulfurized at 700 °C. The plan view data show complete coverage, with mostly-flat areas interrupted by vertically-oriented crystallites growing out-of-plane (**Figure 4.10a-b**). The selected-area electron diffraction (SAED) pattern measured on a mostly-flat region without vertical crystallites (**Figure 4.10c**) shows $\{01\bar{1}0\}$ and $\{11\bar{2}0\}$ diffraction rings, suggesting that these mostly-flat regions have (0001) in-plane texture, with the basal plane lying flat on the substrate. SAED measured on a vertical crystallite (**Figure 4.10d**) shows bright single-crystals diffraction spots from the crystallite, in addition to the rings from the surrounding flat regions. The pair of brightest reflections correspond to a d-spacing of 2.85 Å and we index as the $\{0002\}$ diffraction spots with expected spacing. The absence of $\{0001\}$ spots may result from thickness, tilting effect, or a high concentration of stacking faults, corresponding to imperfect registry of adjacent monolayers.[84] The $(1\bar{1}00)$ and $(1\bar{1}20)$ diffraction spots are also apparent. In **Figure 4.10e** we present a cross-section view that includes a crystallite lying flat on the substrate, and slightly protruding crystallites with

different orientations, extending to approximately twice the height of the flat crystallite; this view is typical of the mostly-flat regions, excluding the tall, vertical crystallites and is consistent with the in-plane texture described above. The TEM data therefore indicate a mostly-flat 1T-TiS_2 film, with crystallites of sub-100 nm lateral width lying mostly flat on the substrate, interrupted occasionally by vertically-oriented crystallites that grew out-of-plane.

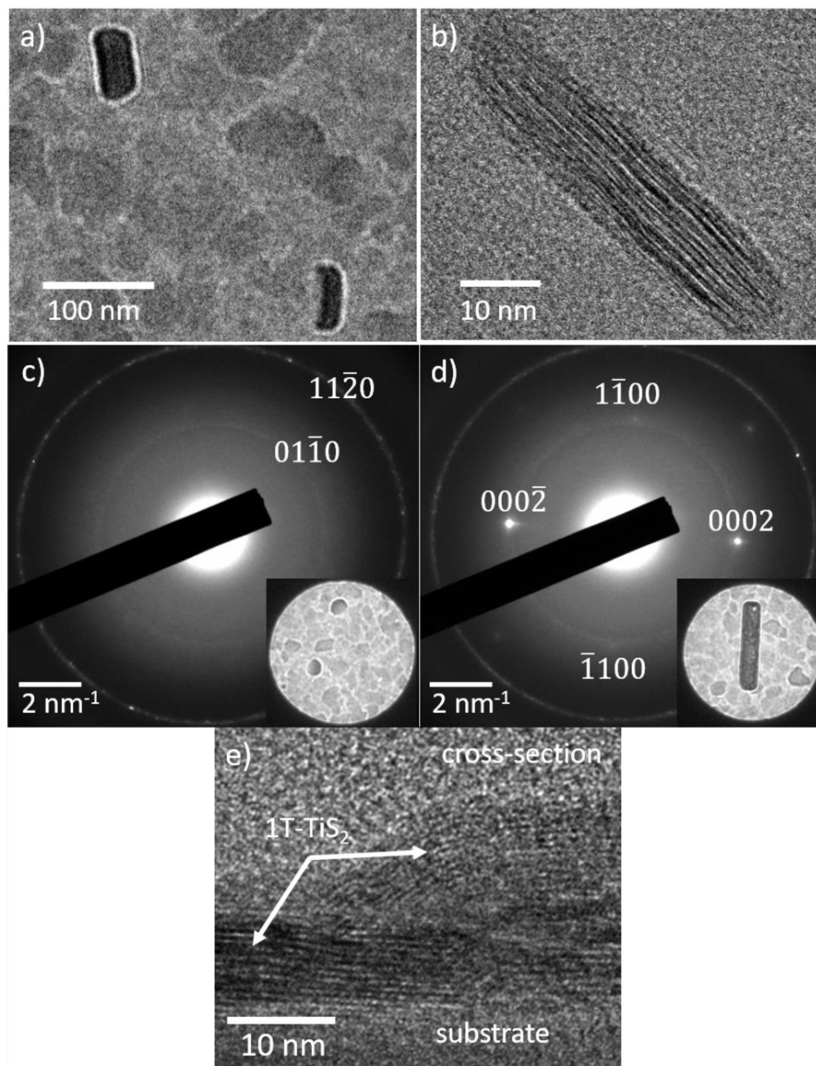

Figure 4.10: TEM study of 1T-TiS_2 films. (a-d) Film approximately 10 nm thick, sulfurized at 600 °C for 3 h; the precursor film was 3 nm thick (Ti metal thickness, measured by QCM). (a) Low-magnification plan view shows mostly-flat regions interrupted by vertical outgrowths. (b) High-resolution plan view of a vertically-oriented crystallite. (c) Diffraction pattern of a mostly-flat region of the film (inset). The indexed diffraction rings are consistent with in-plane (0001) texture of the grains. (d) Diffraction pattern of a region including a vertically-oriented crystallite (inset). The

discrete spots originate from the vertically-oriented crystallite and are consistent with the 1T-TiS_2 phase. The rings originate from the surrounding, mostly-flat film. The diffraction indices correspond to the spots; the ring index assignments are the same as in (c). (e) High-resolution cross-section view of a 1T-TiS_2 film sulfurized at 700 °C for 3 h.

The TEM data provide an explanation for the process by which films roughen during sulfurization, as shown in **Figure 4.11**. The low surface energy of the basal planes provides a thermodynamic driving force for (0001) texture. This is counteracted by the in-plane stress experienced during the formation of TiS_2 (volume 34.78 cm^3 per mole of Ti) from titanium oxide (18.88 cm^3 per mole of Ti for rutile TiO_2). Furthermore, crystal growth is expected to occur fastest at the layer edges. Therefore, crystallites that nucleate randomly with vertically-oriented edges experience accelerated growth, due to preferential edge growth (kinetic roughening), and to relieve the in-plane stress of the sulfurizing film.

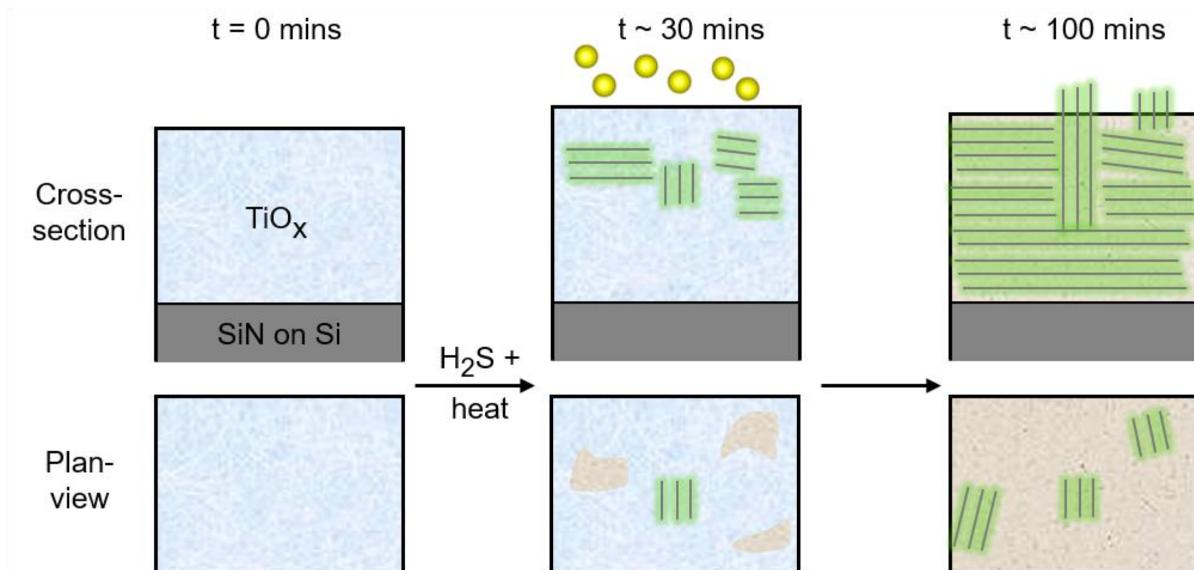

Figure 4.11: Schematic of TiS_2 film formation by sulfurization, visualized in cross-section and plan-view geometry. The concentration of vertically-oriented crystallites is exaggerated for illustration purposes.

The background oxygen concentration present in the tube furnace is a prime factor in determining the sulfurization results, but details of the TiO_x precursor film are also important, especially the thickness. We measure precursor film thickness by QCM (using settings for Ti metal)

during Ti deposition, and by X-ray reflectivity (XRR) post-deposition. The roughness of the resulting TiS_2 film depends proportionally on the precursor film thickness. We found that for precursor films 1 and 5 nm thick (measured by XRR), sulfurized at 600 °C, the resulting TiS_2 film roughness was 1.7 and 7.6 nm, respectively. For precursor films 3 and 5 nm thick (measured by QCM), sulfurized at 700 °C, the resulting TiS_2 film roughness was 7.2 and 10.3 nm, respectively. These results are consistent with expectations that smoother TiS_2 films result from lower sulfurization temperature and thinner precursors. For the results presented in **Figures 4.8-10**, the precursor films were between 3 - 5 nm thick. Raman measurements on the precursor film show no evidence for crystallized Ti or TiO_2; the phase composition is likely a mixture of nanocrystalline Ti and amorphous Ti oxide. Ti oxides (*e.g.* α-TiO and r-TiO_2, shown in **Figure 4.7**) are non-layered structures built from TiO_6 octahedra, and we assume the same of amorphous Ti oxides[85,86]. XPS depth profiling suggests that the Ti:O ratio in the precursor film is 1:2 at the surface, but closer to 1:1.5 beneath the surface. This is consistent with TiO_x forming during deposition, and only the topmost surface fully oxidizing to TiO_2 upon air exposure.

4.4.6. Summary

We conclude that film roughening during sulfurization results from the nucleation and growth of TiS_2 crystallites with initially-random orientation, under the competing influences of a preferred orientation, film stress, and anisotropic growth kinetics. Nucleation and growth of TiS_2 requires overcoming the kinetic barrier of replacing Ti-O bonds by Ti-S bonds. With high oxygen background levels this kinetic barrier is persistent, and requires high sulfurization temperature to overcome. Lower oxygen background levels enable lower sulfurization temperature, presumably by lowering the rate at which new Ti-O bonds form during phase transformation.

Here we synthesized large-area, single-phase 1T-TiS_2 films via a two-step method with sulfurization temperature as low as 500 °C. Based on the trends that we report, we expect that lower-temperature processing should be achievable through further reduction in O_2 background levels, and perhaps also by reducing the oxygen content in the TiO_x precursor film. We also predict that film roughness could be further reduced by lowering the sulfurization rate, for instance by reducing the H_2S process gas pressure.

Low-temperature film processing is desirable for integration and for stabilizing designer alloys. It is not a likely route to make single crystal films. Therefore, devices requiring single crystal TMD layers – such as transistors or quantum emitters – may rely on layer transfer to enable integration, since the TMD growth conditions are rather extreme. However, for many technologies, polycrystalline films do not present an obstacle. For refractive, sub-band gap applications in integrated photonics, such as phase-modulators, chemical purity that controls sub-band gap absorption may be more important than grain size. Besides integrated photonics, the approach that we develop here for film deposition may be useful for optical meta-materials, tribology, and electrochemistry.

The synthesis and characterization details of all the samples mentioned in this section are summarized in **Table 4.1**.

Sample identifier	**Figures**	**Description**	**Workflow**
TiS2_190814	**Figure 4.8**	no Mo cap, 600 °C for 3 h	OM and Raman taken by Akshay on 08/15/19 XPS taken by Yifei on 08/16/19
TiS2_5nm_MoCap_181107	**Figure 4.9a, d**	Mo cap, 900 °C for 24 h	Raman and OM taken by Yifei on 11/07/18
TiS2_190529	**Figure 4.9b, d, 4.10e**	Mo cap, 700 °C for 2.5 h	Raman and OM taken by Akshay on 05/31/19 TEM taken by Kate on 19/09/24

TiS2_191220	**Figure 4.9c, d**	no Mo cap, 500 °C for 4 h	Raman and OM taken by Yifei on 12/22/19
TiS2_191223	**Figure 4.9e, f**	no Mo cap, 500 °C for 4 h	Raman and OM taken by Yifei on 12/24/19
TiS2_grid_200113	**Figure 4.10a-d**	no Mo cap, 600 °C for 4 h	TEM taken by Kate and Yifei on 20/01/29

Table 4.1: List of samples studied in **Section 4.4** including their identifiers (*i.e.*, names), as found in our laboratory records and data files.

4.5. Stabilizing far-from-equilibrium (Mo,Ti)S_2 thin films by metal sulfurization at reduced temperature

4.5.1. Introduction

Alloy design offers a path towards new and useful TMDs that combine the relatively low optical loss in the near infrared of many sulfide TMDs, with lower energy requirements for phase-change functionality than in pure sulfides (*e.g.*, MoS_2)[18,67].

Here we focus on a fundamental challenge of alloy design: making uniform materials of a desired composition and phase, while suppressing unwanted chemical segregation and secondary phase formation. We report synthesis of $Mo_{1-x}Ti_xS_2$ thin films using a two-step method of metal film deposition by magnetron sputtering, followed by sulfurization in H_2S in a hot-wall tube furnace. The method is reliable and compatible with wafer-scale deposition. We emphasize relatively low sulfurization temperature, 600°C and below, which slows phase segregation and is compatible with deposition on PIC wafers including waveguides and dielectrics. Low processing temperature also promotes smooth and uniform films, which are needed for planar device processing. We design for relatively thick (over 10 nm) and nanocrystalline films. The film thickness, much larger than monolayer and few-layer films that are emphasized for TMD optoelectronics and microelectronics, is chosen to enhance the optical interaction volume in PIC devices, as we have demonstrated through numerical simulation[67]. We also claim that nanocrystalline, dense films may be preferable to single-crystal films for phase-change

functionality in PIC applications: grain boundaries make a much smaller contribution to parasitic, below-band gap optical loss than do chemical impurities, and nanocrystalline material may have lower barriers to phase-change behavior than single crystals, as has been discussed for phase transformations in other classes of materials[87–89]. The nanocrystalline, vertically-oriented, far-from-equilibrium thin films that our process enables may prove useful also for applications in chemical sensing and catalysis.

4.5.2. Experimental Techniques

We use a two-step method to synthesize $Mo_{1-x}Ti_xS_2$ films. Firstly, we deposit precursor Mo-Ti alloy films, of thickness below 10 nm), by magnetron sputtering (AJA international Orion 5, base pressure 10^{-5} Torr) on Si_3N_4/Si substrates. We control the precursor composition by calibrating the metal source rates, using a quartz crystal monitor (QCM), before deposition by co-sputtering. We choose Si_3N_4 as a substrate relevant for PIC device integration, and to avoid oxide substrates that could be a oxygen source during sulfurization.

Secondly, we sulfurize the precursor films in a hot-wall tube furnace reactor at atmospheric pressure, in a flow of between 20 – 100 sccm H_2S and 0 – 200 sccm forming gas (FG, 5% H_2, 95% Ar or N_2), at temperature between 500 and 600 °C. We use two different methods to cool the samples after sulfurization. "Slow cooling" refers to simply turning off the heating elements, and allowing the furnace to cool on its own, whereas "quench cooling" refers to opening the furnace enclosure, directly exposing the full hot tube to ambient air. Quench cooling from 500 °C to 300 °C takes more than 5 hours, whereas in quench cooling this same temperature drop is achieved in seconds. In both methods, the H_2S environment is maintained during cooling to avoid oxidation.

We use X-ray photoelectron spectroscopy (XPS) (Thermo Scientific Nexsa XPS, Al Kα source) to characterize the surface composition and chemistry of our films. We determine phase using

Raman spectroscopy (Renishaw Invia Reflex Micro Raman), with an excitation wavelength of 532 nm. We use atomic force microscopy (AFM, Veeco Dimension 3100) to characterize film morphology. We preform scanning electron microscopy (SEM, Zeiss Merlin) in plan-view geometry. We perform atomic resolution scanning transmission electron microscopy (STEM) using a probe-corrected microscope (Thermo Fisher Scientific Themis Z G3 60–300 kV S/TEM) operated at 200 kV, with a beam current of 30-40 pA, and 25 mrad convergence angle. We collected 4D STEM data using camera lengths of 360 mm and 460 mm, and a collection angle of 48 mrad. We prepared lamellar cross-sections for STEM imaging using a focused ion beam (FEI Helios 600) system, with Au and Pt protection layers. We characterized film optical properties using spectroscopic ellipsometry (SEMILAB SE2000).

The Mo:Ti metals ratio determined by QCM calibration is subject to systematic errors, including the fact that we calibrate the QCM for metallic Ti, but Ti metal is likely to partially oxidize, even in the sputtering chamber. We measure the metals ratio again after film sulfurization, by X-ray energy dispersive spectroscopy (EDS) measurements, but these results are affected by film non-uniformity (discussed below). Therefore, throughout this thesis we refer to our samples according to the metal composition x (as in $Mo_{1-x}Ti_xS_2$) determined by QCM calibration, unless explicitly stated otherwise.

4.5.3. Synthesized $Mo_{0.6}Ti_{0.4}S_2$ film

In **Figure 4.12** we present a $Mo_{0.6}Ti_{0.4}S_2$ film sulfurized at 550 °C for 1 hr, in 50 sccm H_2S and 150 sccm FG. Micrographs reveal a dense, nanocrystalline film, decorated by protruding, isolated particles. The film is a uniform TMD alloy, and the particles are titanium oxide. The precursor film was 5 nm thick, and the sulfurized film is 17 nm thick. The TMD alloy is Mo-rich, relative to the precursor, due to segregation of Ti in the particles on the surface. XPS data (**Fig. 1c**,

measured after 30 s ion milling) suggest that both Mo and Ti in the film are fully-sulfurized and consistent with core-level spectroscopy on MoS_2 and TiS_2. Depth-profiling reveals that the fraction of oxidized Ti increases near the surface, consistent with a sulfide $Mo_{1-x}Ti_xS_2$ film and TiO_x particles on top.

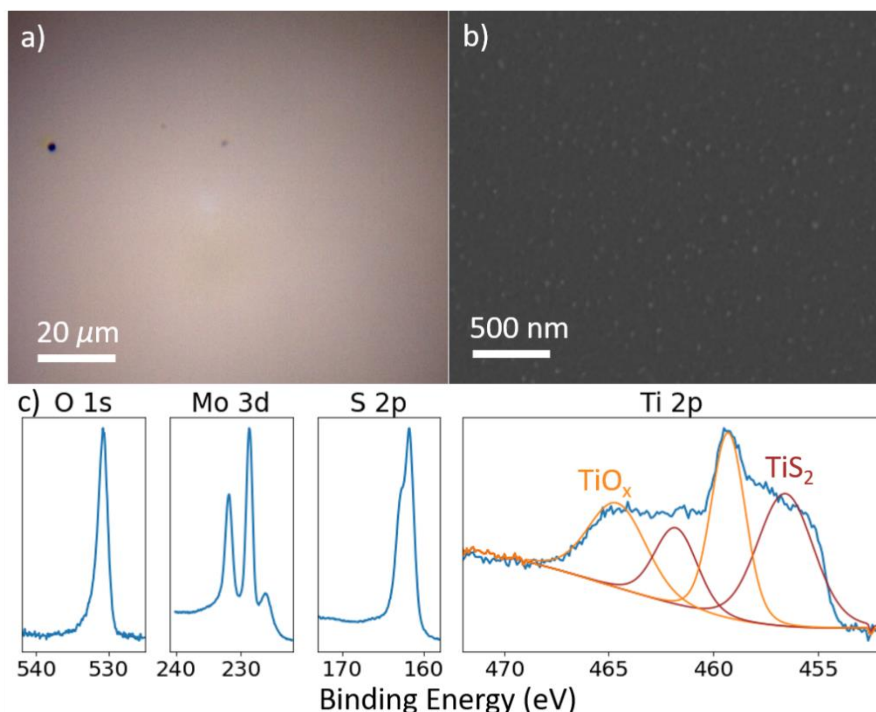

Figure 4.12: $Mo_{0.6}Ti_{0.4}S_2$ film, 17 nm thick, synthesized by sulfurization at 550 °C for 1 h. (a) Optical micrograph. (b) Plan-view SEM micrograph, showing a film-and-particle morphology. (c) XPS data measured after 30 s depth profiling (to clean surface carbon). We fit Ti 2p spectrum with 2 double peaks. 464.6 and 459.3 eV are corresponding to Ti oxide and the 461.8 and 456.5 eV are corresponding to Ti sulfide.

We use a combination of STEM EDS, atomic-resolution imaging, and Raman spectroscopy to identify the film as $Mo_{0.7}Ti_{0.3}S_2$ in the 2H, trigonal phase (MoS_2 structure type). In **Figure 4.13a** we present high-angle annular dark field (HAADF) imaging and EDS data, further illustrating that the sample structure is a sulfide alloy film capped by TiO_x particles. EDS data quantifies the film metals composition as $Mo_{0.7}Ti_{0.3}S_2$; as expected, this is Mo-rich compared to the precursor composition, due to Ti segregation. Atomic-resolution imaging (**Figure 4.13b**) shows a Moiré pattern, consistent with a layered crystal structure and hexagonal symmetry; definitive phase

identification by TEM is difficult due to the nanocrystalline, irregular film texture. Raman data (**Figure 4.13c**) display the peaks at 383 and 411 cm^{-1}, typical of 2H-MoS_2, and not the peak at 335 cm^{-1} typical of 1T-TiS_2. Electron diffraction (below) also attests to the 2H phase.

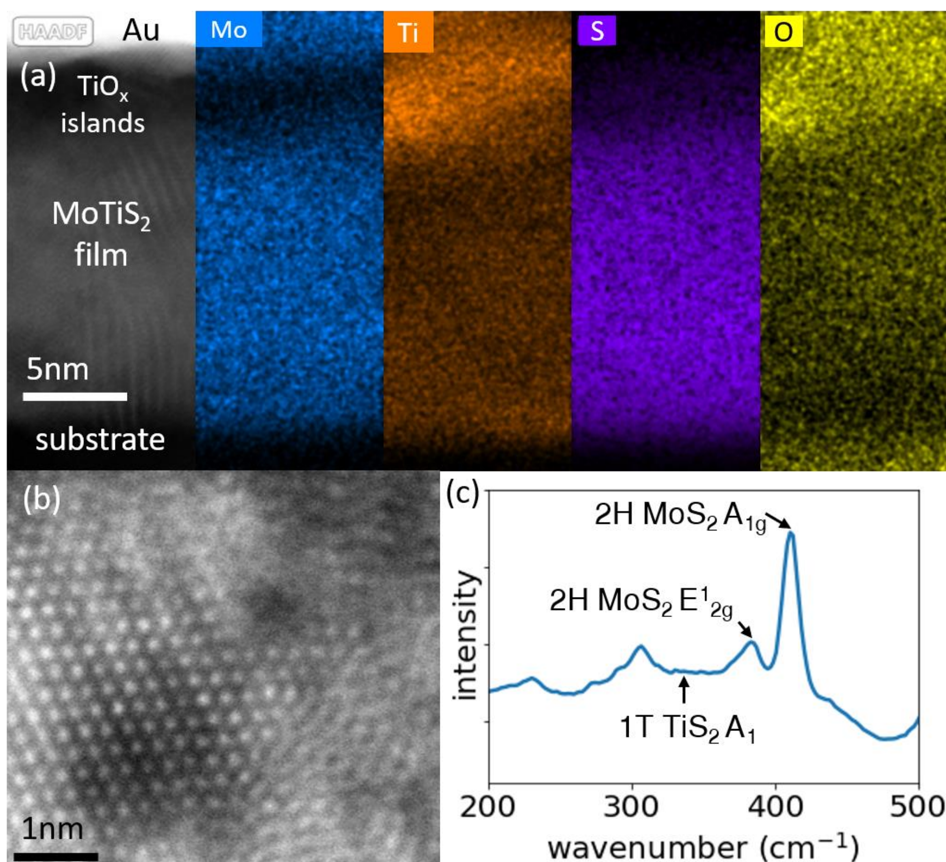

Figure 4.13: Composition and phase analysis of the $Mo_{0.6}Ti_{0.4}S_2$ film presented in **Fig. 1**. (a) Cross-section HAADF micrograph and EDS maps. (b) HAADF STEM image collected at 200 kV. (c) Raman spectrum, with characteristic peaks labeled.

4.5.4. Morphology optimization by rapid sulfurization at low temperature

To investigate the mechanism of particle formation, we sulfurize films for varying temperature, time, and cooling rate. In **Figure 4.14a-b** we present SEM data for $Mo_{0.5}Ti_{0.5}S_2$ sulfurized at 500 °C (36 h) and 600 °C (2 h); both were cooled slowly. Compared to the 500 °C sample, the particles in the 600 °C sample have undergone substantial coarsening, suggestive of a thermally-activated process of nucleation and growth. Raman data (**Figure 4.14c**) show that sulfurization at 600 °C promotes formation of the 1T-TiS_2 phase. EDS mapping data show that the particles in the

sample synthesized at 600 °C have composition TiS_2, whereas only TiO_x is present in the 500 °C sample.

Our calculated Gibbs free energy-composition data predict that the MoS_2-TiS_2 binary system is fully immiscible at moderate temperature[18]. We therefore expect a thermodynamic driving force Ti and Mo to segregate during sulfurization. The results presented here on metal film sulfurization illustrate that the process of phase segregation occurs first by Ti metal diffusion and coalescence into Ti-rich particles, which then transform into TiS_2 if given sufficient time and temperature in the sulfurizing armosphere. Since MoS_2 forms from Mo metal more readily than TiS_2 does from Ti metal (due in part to residual oxygen), it seems likely that during sulfurization, Ti metal and TiO_x diffuse through MoS_2.[65,66]

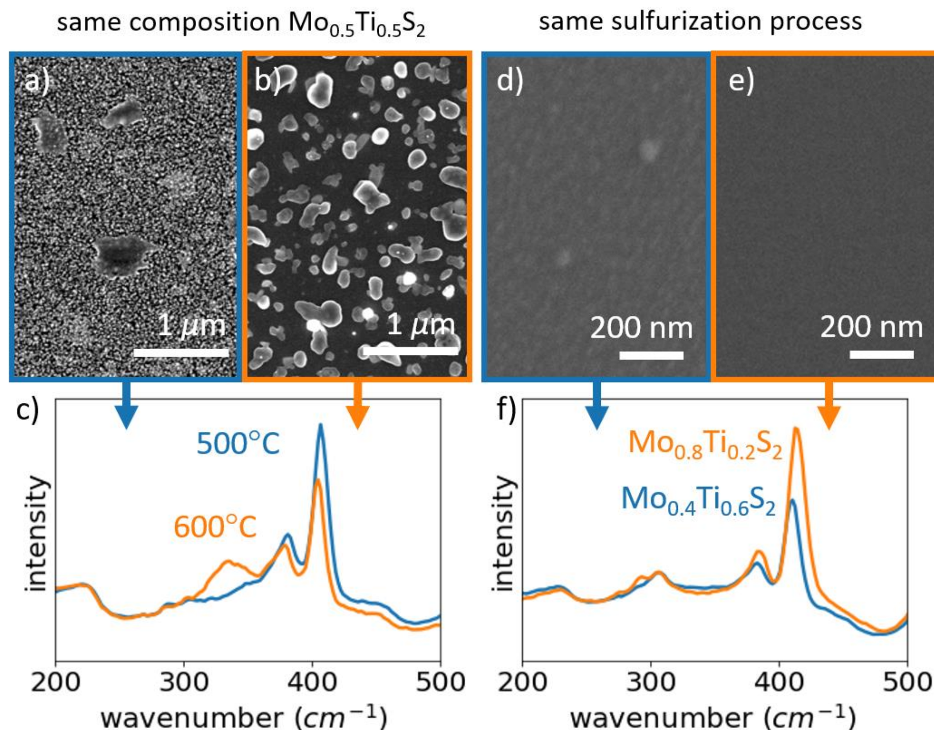

Figure 4.14: Select examples of how film morphology and phase vary with sulfurization temperature, time, cooling rate, and composition. (a-b) Plan-view SEM micrographs of $Mo_{0.5}Ti_{0.5}S_2$ films sulfurized at 500 °C (36 h) and 600 °C (2 h), respectively, both with slow cooling. (c) Raman spectra of films shown in (a-b), illustrating the emergence of 1T-TiS_2 phase with higher-temperature sulfurization. (d-e) Plan-view SEM micrographs of $Mo_{0.4}Ti_{0.6}S_2$ and $Mo_{0.8}Ti_{0.2}S_2$ films, respectively,

both sulfurized at 550 °C (1 h) with quench cooling. (f) Raman spectra of films shown (d-e), illustrating presence of only the 2H phase for films sulfurized at 550 °C and for shorter time, even as the Ti content triples from 20% to 60% metals basis.

These results suggest that rapid sulfurization at lower temperature is key to making high-Ti-content, single-phase $Mo_{1-x}Ti_xS_2$ films. In **Figure 4.14d-f** we present the results of sulfurizing films with two very different Ti contents, $Mo_{0.8}Ti_{0.2}$ and $Mo_{0.4}Ti_{0.6}$, at 550 °C and with quench cooling. The resulting films are much smoother than those sulfurized for longer time and at higher temperature, and the Raman spectra show evidence only of the 2H phase. We conclude that faster and lower-temperature processing can successfully trap Ti during sulfurization, yielding far-from-equilibrium, high-Ti-content 2H-phase thin films. We note that, although Ti and Mo metals have a wide miscibility gap for the temperature range studied here, we are assuming that they are fully mixed in the precursor films, which are deposited by sputtering on unheated substrates.

4.5.5. Orientation of synthesized film

In **Figure 4.15** we present results of 4D STEM measurements of a $Mo_{0.6}Ti_{0.4}S_2$ film sulfurized at 550 °C for 1 hr, with quench cooling. **Figure 4.15a** illustrates diffraction data measured at a single spot within the film. We see a pair of low-angle diffraction spots, at radius $(6.44\ \text{Å})^{-1}$, corresponding to the thickness of monolayer. Their appearance as discrete spots indicate that the crystal layers are aligned vertically with respect to the substrate. In **Figure 4.15b** we present analysis of the angular distribution of diffraction intensity averaged across the entire sample, a lamellar cross section of area 15x64 nm^2. The data show the film is strongly textured with the layers aligned vertically. In other words, the single-spot analysis in **Figure 4.15a** is representative of the film as a whole.

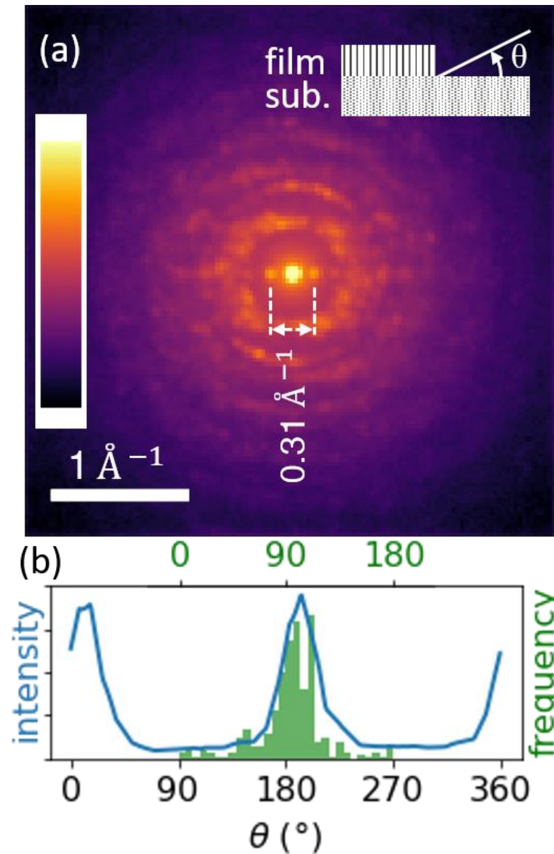

Figure 4.15: 4D STEM diffraction data measured on of $Mo_{0.6}Ti_{0.4}S_2$ film synthesized at 550 °C for 1 h, quench cooling. (a) Diffraction data measured at a spot fully within the TMD film, excluding the particles on top. The vertical direction in the image corresponds to the out-of-plane direction in the sample. Colorbar indicates diffraction intensity on a log scale. The two spots at low angle correspond to a layer spacing of 6.44 Å, consistent with typical TMD monolayer thickness. Their appearance as discrete spots, instead of a ring, indicates that the film is strongly textured with the TMD layers out-of-plane, as illustrated in the inset. (b) Angular distribution of diffraction intensity at radius $(6.44\ \text{Å})^{-1}$, averaging data measured at 60x256 pixels across a film cross section 15x64 nm^2. The strong central peak indicates that the film texture, visualized in (a) for measurement at a small region of 2.5x4 nm^2, is representative of the film as a whole. Distribution of the orientation, which is defined by the angle θ between TMD layer and substrate, for every 1x1 nm^2 spot through the film cross section. The layers are preferentially aligned vertically, with an angular spread of 27.24° (root-mean-square) around vertical ($\bar{\theta}$= 94.28°).

4.5.6. Optical property

The far-from-equilibrium TMD alloy films demonstrated here could be useful for various applications, including photonic integrated circuits, for which they could be deposited and patterned into devices to control optical phase. In anticipation of future such developments, we

report in **Figure 4.16** the optical properties of a $Mo_{0.6}Ti_{0.4}S_2$ film sulfurized at 550 °C for 1 hr, with quench cooling (as in **Figure 4.12**), measured by SE. In **Figure 4.16a** we present the measured spectroscopic angles, Ψ and Δ. In **Figure 4.16b** we present the inferred, effective complex refractive indices, n_{eff} and k_{eff}, and compare to results for MoS_2. TMDs are strongly birefringent, and the film texture means that our SE measurements mix the ordinary and extraordinary components of the refractive index, hence the label "effective". Meanwhile, the data we present for MoS_2 are the ordinary and extraordinary refractive indices[90].

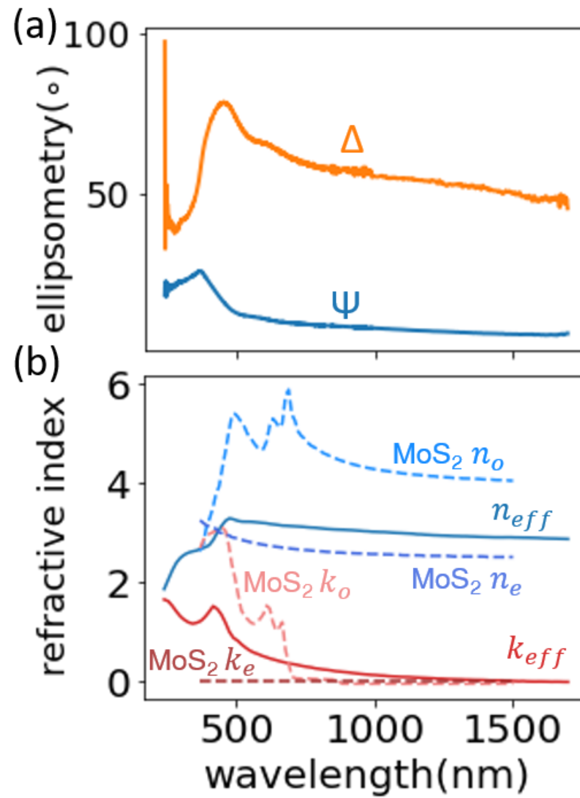

Figure 4.16: SE results for $Mo_{0.6}Ti_{0.4}S_2$ film, sulfurized at 550 °C for 1 hr, with quench cooling. (a) Ψ and Δ spectra measured at a 75° angle of incidence. (b) Inferred, effective refractive indices n_{eff} and k_{eff}; data are labeled effective because measurements mix the ordinary and extraordinary components, due to the crystallographic texture. Also shown for reference are the complex ordinary and extraordinary refractive indices of MoS_2[90].

Unlike MoS_2 that displayed three absorption resonances, we observed only one resonance at 420 nm (2.95 eV) in the $Mo_{0.6}Ti_{0.4}S_2$ film. The peak position is close to previously reported

resonances for MoS_2 at 2.8 and 3.1 eV, and TiS_2 at 3.3 eV, but the specific origin of this absorption feature remains unknown.[51,91,92] The SE results show that $Mo_{0.6}Ti_{0.4}S_2$ has low optical loss below the band gap, similar to pure MoS_2, despite the high concentration of Ti which is expected to favor metallicity.

4.5.7. Summary

We synthesized large-area, high-Ti-content, single-phase 2H alloy $Mo_{1-x}Ti_xS_2$ thin films via a two-step method with sulfurization temperature as low as 500 °C. Since the high Ti-alloy $Mo_{1-x}Ti_xS_2$ are far-from-equilibrium in the MoS_2-TiS_2 binary system, a thermodynamic driving force segregate Ti and Mo during sulfurization. The phase segregation occurs first by the diffusion of Ti metal and/or TiO_x oxide to the film surface, where they coalesce into Ti-rich particles that emerge from the sulfurization process as TiO_x or TiS_2, depending on the extent of sulfurization. Rapid sulfurization at lower temperature is key to suppressing phase segregation and making smooth and uniform alloy films, by kinetically trapping Ti in the forming TMD crystal structure. Based on the trends that we report here, we expect that the film morphology could be further improved by more precise control of the sulfurization time, and by further reducing the background O_2 concentration in the reactor, as discussed in our previous work.[66]

The 2H-$Mo_{1-x}Ti_xS_2$ alloy films exhibit low sub-band gap optical loss, despite a large concentration of Ti, which ought to favor metallicity (TiS_2 is semi-metallic). This is promising for using these and similar alloys for optical phase control with low insertion loss in photonic integrated circuits. By approaching the 2H-1T phase boundary in metastable alloys, we expect to reduce the thermodynamic barrier for phase transformation, enabling phase-change functionality in TMD alloys. We also note that the nanocrystalline and vertically-aligned film texture may be useful for applications in chemical sensing and catalysis.

The synthesis and characterization details of all the samples mentioned in this section are summarized in **Table 4.2**.

Sample identifier	Figures	Description	Workflow
MoTiS2_6040_550C_1h_211105	**Figure 4.12a-b, 4.13, 4.15, 4.16**	$Mo_{0.6}Ti_{0.4}S_2$ film, 17 nm thick, synthesized by sulfurization at 550 °C for 1 h, quench cooling	OM and Raman taken by Yifei on 11/07/21 SEM taken by Seong Soon on 11/15/21 TEM, EDS and 4D STEM taken by Kate on 01/22/22 Ellipsometer taken by Yifei on 11/12/21
MoTiS2_6040_550C_1h_211216	**Figure 4.12c**	$Mo_{0.6}Ti_{0.4}S_2$ film, 17 nm thick, synthesized by sulfurization at 550 °C for 1 h, quench cooling	XPS taken by Yifei on 12/20/21
MoTiS2_5050_500C_36h_210526	**Figure 4.14a, c**	$Mo_{0.5}Ti_{0.5}S_2$ film, 17 nm thick, synthesized by sulfurization at 500 °C for 36 h, slow cooling	Raman taken by Yifei on 06/02/21 SEM taken by Baoming on 08/31/21
MoTiS2_5050_600C_2h_210516	**Figure 4.14b, c**	$Mo_{0.5}Ti_{0.5}S_2$ film, 17 nm thick, synthesized by sulfurization at 600 °C for 2 h, slow cooling	Raman taken by Yifei on 05/19/21 SEM taken by Baoming on 08/31/21
MoTiS2_4060_550C_1h_211105	**Figure 4.14d, f**	$Mo_{0.4}Ti_{0.6}S_2$ film, 17 nm thick, synthesized by sulfurization at 550 °C for 1 h, quench cooling	Raman taken by Yifei on 11/07/21 SEM taken by Seong Soon on 11/15/21
MoTiS2_8020_550C_1h_211105	**Figure 4.14e, f**	$Mo_{0.8}Ti_{0.2}S_2$ film, 17 nm thick, synthesized by sulfurization at 550 °C for 1 h, quench cooling	Raman taken by Yifei on 11/07/21 SEM taken by Seong Soon on 11/15/21

Table 4.2: List of samples studied in **Section 4.5** including their identifiers (*i.e.*, names), as found in our laboratory records and data files.

4.6. Summary

In the Chapter, we discuss the thin film synthesis of MoS_2, TiS_2 and alloy $(Mo,Ti)S_2$ via two-step method, which is depositing transition metal thin films by PVD and sulfurizing the metal films in the H_2S environment in our own CVD style furnace.

We find that adding trace quantities of O_2 during sulfurization accelerates MoS_2 crystallization at reduced temperature, without affecting sulfur diffusion or overall film composition. The

catalytic effect of O_2 allows us to grow large area MoS_2 thin films on various substrates at processing temperatures below 400 °C.

We synthesized large-area, single-phase 1T-TiS_2 films with sulfurization temperature as low as 500 °C. We conclude that film roughening during sulfurization results from the nucleation and growth of TiS_2 crystallites with initially-random orientation, under the competing influences of a preferred orientation, film stress, and anisotropic growth kinetics. Lower oxygen background levels enable lower sulfurization temperature, which suppresses the formation of new Ti-O bonds during sulfurization and improves the film morphology. Based on the trends that we report, we expect that lower-temperature processing should be achievable through further reduction in O_2 background levels, and perhaps also by reducing the oxygen content in the TiO_x precursor film.

We synthesized large-area, high-Ti-content, single-phase 2H alloy $Mo_{1-x}Ti_xS_2$ thin films with sulfurization temperature as low as 500 °C. Since the high Ti-alloy $Mo_{1-x}Ti_xS_2$ are far-from-equilibrium in the MoS_2-TiS_2 binary system, a thermodynamic driving force segregate Ti and Mo during sulfurization. The phase segregation occurs first by the diffusion of Ti metal and/or TiO_x oxide to the film surface, where they coalesce into Ti-rich particles that emerge from the sulfurization process as TiO_x or TiS_2, depending on the extent of sulfurization. Rapid sulfurization at lower temperature is key to suppressing phase segregation and making smooth and uniform alloy films, by kinetically trapping Ti in the forming TMD crystal structure. The 2H-$Mo_{1-x}Ti_xS_2$ alloy films exhibit low sub-band gap optical loss, which is promising for optical phase control with low insertion loss in photonic integrated circuits.

Chapter 5

5. Ongoing and Future Work

The Chapter includes our current work on demonstrating phase transformation of synthesized TMD thin films. I contributed on the experiment design, device fabrication and process optimization, and device characterization.

5.1. Phase change demonstration by Charge Injection

5.1.1. Design of stack for voltage gating TMD

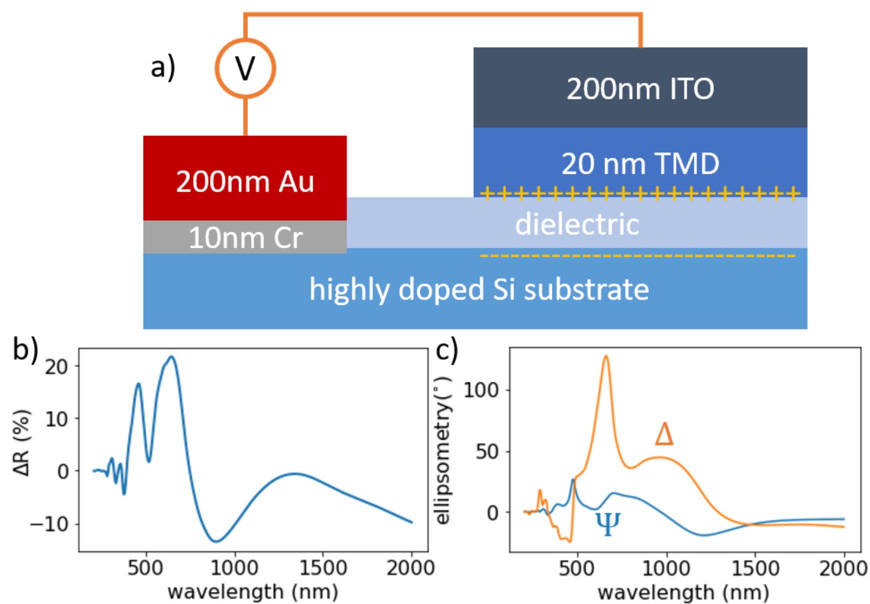

Figure 5.1: The stack for TMD phase change demonstration. a) Schematic diagram b) Difference between simulated reflection spectra of the stacks containing 2H and 1T phase MoS_2 as TMD layer and 20nm Al_2O_3 as dielectric layer c) Difference between simulated ellipsometric angles (Ψ and Δ) spectra (AoI=70°) of the stacks containing 2H and 1T phase MoS_2 as TMD layer and 20nm Al_2O_3 as dielectric layer.

To demonstrate the phase change behavior of the TMD, we use voltage gating method and design the stack as shown in **Figure 5.1a**. By applying voltage across ITO and gold electrodes, the charges accumulate around the Al_2O_3/TMD interface, thus excess charge is injected into TMD layers to induce phase transformation. Since ITO is transparent, we can perform optical characterizations including Raman, ellipsometry and FTIR on TMD layer to observe the phase

change process. We use DFT-calculated refractive index of 2H and 1T phase of MoS_2 to simulate the difference of reflection and ellipsometric spectra of the stacks containing 2H and 1T phase MoS_2 as TMD layer and 20nm Al_2O_3 as dielectric layer, as shown in **Figure 5.1b and c**.

5.1.2. Method: fabrication and characterization

We have tried SiO_2, Si_3N_4 and Al_2O_3 as dielectric materials. For SiO_2 and Si_3N_4, we purchased low resistive (<0.005 Ω-cm) p-type Si wafers with 100 nm SiO_2, 100 nm Si_3N_4 or 10 nm Si_3N_4 layer on top. The 10nm SiO_2 and Si_3N_4 layers have less than 3 nm deviation from the nominal thickness, we thus use ellipsometer to measure and fit the thickness before the stack fabrication. For Al_2O_3, we deposit Al_2O_3 on the substrate of 10nm Si_3N_4 on Si by atomic layer deposition (ALD) using trimethylaluminum (TMA) and H_2O gas under 300 °C. As we will discuss, the Si_3N_4 s no longer insulating after sulfurization in H_2S under elevated temperature. To reduce the impurity for better insulation, we pre-deposit 10nm Al_2O_3 on a 6-in wafer and use the pre-deposited 6-in wafer to isolate substrate and chamber during sample deposition. The thickness of Al_2O_3 is confirmed by post-deposition ellipsometry and multilayer model fitting. We have tried MoS_2 and $Mo_{1-x}Ti_xS_2$ as TMD layers. The synthesis is similar to the two-step method discussed in **Chapter 4**, except that we pattern the metal precursor by shadow mask during PVD process. All MoS_2 layers are sulfurized under 500 °C with slow cooling whilst all $Mo_{1-x}Ti_xS_2$ layers are sulfurized under 550 °C with quench cooling. We use sputter to deposit patterned ITO layer on patterned TMD layers. The growth rate is calibrated by depositing patterned thick ITO layers on substrate and measure the step by profilometer (Bruker DXT Stylus Profilometer). We deposit gold as electrode and Cr as adhesion layer between the wafer and gold, using E-beam deposition (AJA electron-beam evaporator system). The dielectric layer is removed by ion milling (etching rate ~ 2 nm/min) in the same chamber before metal deposition. We usually make multiple metal electrodes so that we can

check whether the contacts are ohmic. The metal electrode deposition can only be done after TMD layer synthesis because the H_2S could sulfurize gold. Since the E-beam is very crowded, we sometimes use ITO to replace metal electrode by sputtering patterned ITO directly on dielectric layer. Since the dielectric underneath is not removed, we are testing the behavior of two identical (ideally) capacitors in series when we apply voltage across ITO electrodes. Only the sulfurization step requires elevated temperature and all the fabrication methods mentioned above are dry processes to avoid further damage on synthesized TMDs. Also, all the methods are chosen to be scalable for future integration and application, as summarized in **Figure 5.2**.

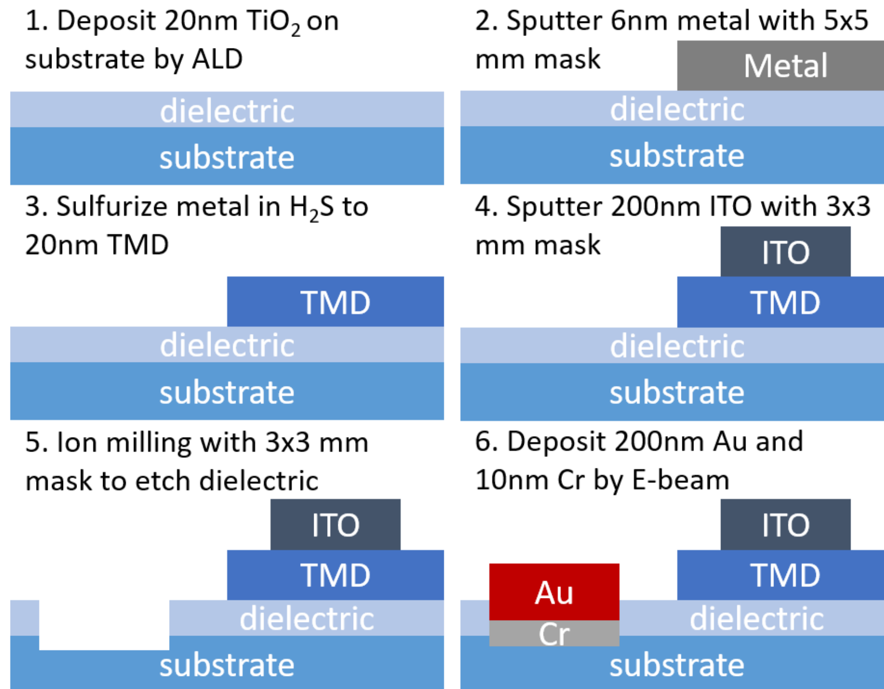

Figure 5.2: The schematic diagram of the fabrication process of the phase change demonstration stack.

We apply voltage to measure the current by contacting the electrodes with probes, using Keithley 2450 SourceMeter. We measured the optical response through ITO electrode by ellipsometer (SEMILAB SE2000) with focused optics (50 µm spotsize), as shown in **Figure 5.3**. Due to the shadow effect, even though some ITO electrodes are 3x3 mm^2 square, only about 2x2

mm^2 in the center is clear enough for optical techniques and we need to avoid the probe as well. Therefore, the focusing of ellipsometry is assisted by the microscope camera on top of the ellipsometer sample stage.

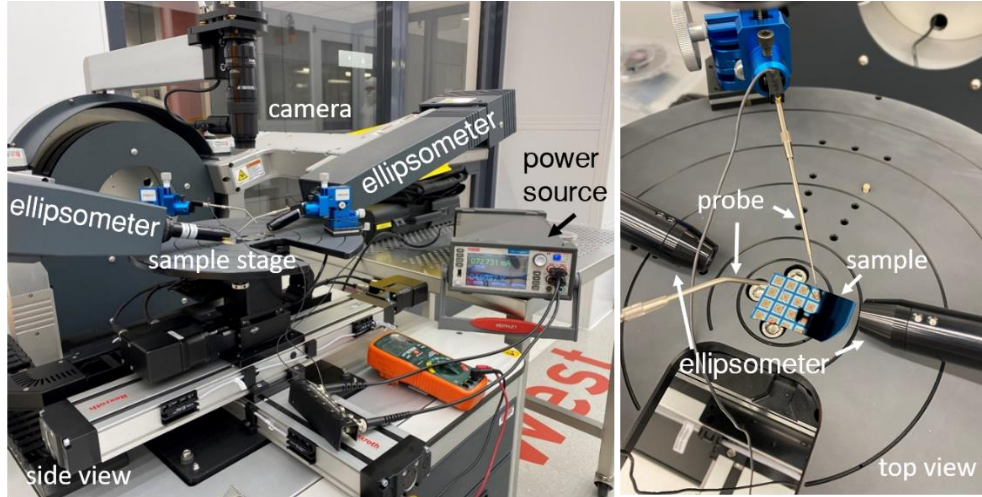

Figure 5.3: The experiment setup with ellipsometer and source meter to measure the optical response when the voltage is applied across the phase change demonstration stack through probes. The sample is a stack containing MoS_2 as TMD layer and 100 nm Si_3N_4 as dielectric layer.

5.1.3. Intermediate results and discussion

So far, we haven't observed any phase change behavior on the fabricated stack containing MoS_2 and alloy $Mo_{1-x}Ti_xS_2$ as TMD layers, but several intermediate results are worth mentioning and discussion.

To verify the fabrication and characterization process, choose MoS_2 as TMD layer and 100 nm SiO_2 as dielectric layer. However, we observe a large leakage current (about 1.5mA under 10V, gate area 2 cm^2) when we apply voltage on gold and ITO electrodes. Therefore, we fabricated a similar stack containing MoS_2 as TMD layer and 100 nm SiO_2 as dielectric layer without removing dielectric below metal electrodes, as shown in **Figure 5.4**. All electrodes are at least 1mm from the edge to avoid edge conduction. Three capacitors (electrode-dielectric-Si) are below three electrodes correspondingly and we denote them as 1, 2, 3. Applying voltage on two of three

electrodes, we test the leakage current of two corresponding capacitors in series. Applying 2V on gate area 2 cm^2, the leakage current of capacitor 1 and 2 in series is 24 μA; the leakage current of capacitor 1 and 3 in series is 6170 μA; the leakage current of capacitor 2 and 3 in series is 20 μA. We deduce that the leakage current of capacitor 1 is significantly lower than that of 2 and 3. However, even leakage current density in the scale of 10 $\mu A/cm^2$ under 2V is still too large, because the same 100 nm SiO_2, without sulfurization in H_2S under elevated temperature, gives about 0.1 $\mu A/cm^2$ under 5V, which is 100 times smaller. The reasonable explanation is that the sulfurization process could degrade the SiO_2 and increase the leakage current significantly. Also, the effect is not uniform in cm scale and the TMD layer on top can't prevent the degradation. Therefore, we design 2 concentric shadow masks, 5x5 mm with 1 mm spacing for TMD and 3x3 mm with 3 mm spacing for electrodes, to make multiple small electrodes with capacitors below, so we can select the ones with low leakage current.

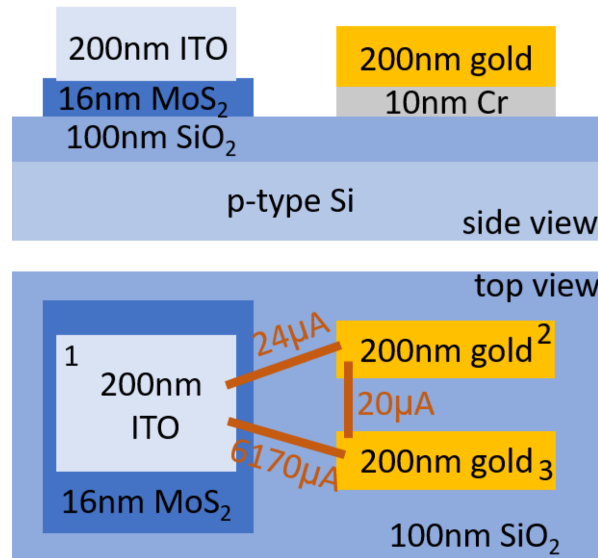

Figure 5.4: The schematic diagram of stack containing 16nm MoS_2 as TMD layer and 100nm SiO_2 as dielectric layer, without removing dielectric below metal electrodes. The red lines indicate the current when 20V DC voltage is applied across electrodes.

Since SiO_2 after sulfurization process is too leaky, we turn to use 100 nm Si_3N_4 as dielectric layer. The fabricated stack containing MoS_2 as TMD layer is shown in **Figure 5.5a** and we apply

voltage across two ITO electrodes to test the leakage current of two capacitors (ITO-MoS_2-Si_3N_4-Si) in series. We find a pair of capacitors in series gives leakage current 0.291 nA under 5V (gate area 9 mm^2) and shows clear charging or discharging behavior when we apply or stop applying large voltages. We apply from 0 to 40 V (maximum voltage of the meter) and measure the ellipsometric spectra, as shown in **Figure 5.5b**. No significant difference could be distinguished because the charge injected into the TMD layer is too low. The charge density σ could be injected into the system

$$\sigma = \frac{CV}{A} = \varepsilon_0 \varepsilon \frac{V}{d} \tag{5.1}$$

where C is the capacitance, V is the voltage, A is the area, d is the thickness of dielectric layer, ε is the dielectric constant of the dielectric material and ε_0 is the permittivity constant of vacuum. The dielectric of Si_3N_4 is 7.5 while the dielectric constant of SiO_2 is 3.9. Therefore, assuming that all the charges are accumulated in the very bottom layer of MoS_2, the sheet charge density injected under 40V is 0.0133 $\mathrm{C/m^2}$ = 0.0071 e/f.u.. However, at least 0.2 e/f.u. is required to induce the phase transformation according to previous theory prediction and experiments[93–95]. Therefore, to inject more charges, we decide to use 10 nm Si_3N_4, which is the wafer with the thinnest silicon nitride layer available for us, as dielectric layer.

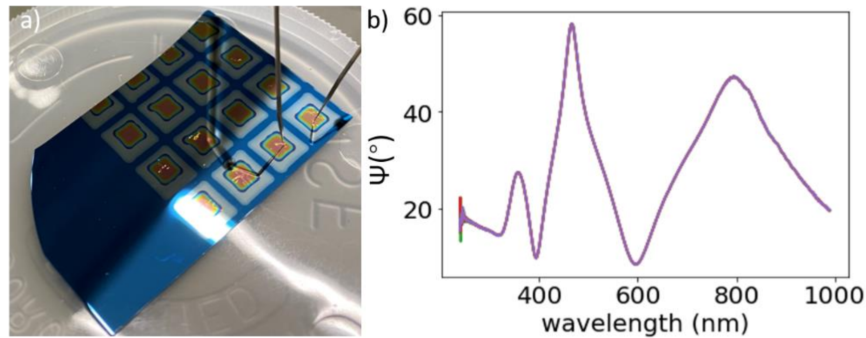

Figure 5.5: a) Photo of the fabricated stack containing 16nm MoS_2 as TMD layer and 100nm Si_3N_4 as dielectric layer, without metal electrodes. b) The ellipsometry spectra with *AoI* = 75° under the 0 – 40 V across the probes

However, the sulfurization process could degrade Si_3N_4 as well. In the same stack using 100 nm Si_3N_4 layer as dielectric, we find another pair of capacitors in series gives 105 μA (maximum current of the meter) under 0.0618 V. We made more than 30 capacitors with 14 nm Si_3N_4 as dielectric, but none of them give reasonable leakage current.

Therefore, we turn to Al_2O_3 as dielectric. We use ALD to deposit 20nm Al_2O_3 layer on 10 nm Si_3N_4/Si substrate, which is assumed to be conductive everywhere after sulfurization process. To avoid the impurities on the ALD chamber to diffuse into the Al_2O_3 layer during deposition, we pre-deposit 10 nm Al_2O_3 on a 4-in wafer and put the sample (less than 3 in) on top of the 4-in wafer for sample deposition. After few rounds of process optimization, the deposited 20 nm Al_2O_3 layer without sulfurization process gives a breakdown voltage of 20V, consistent with previously reported value 10 MV/cm, and the leakage current of 3.7 – 93.6 nA under 20V (gate area 9 mm^2)[96]. Taking the dielectric constant of ALD-deposited Al_2O_3 as 8.5, the corresponding maximum sheet charge density could be injected is 0.0752 C/m^2 = 0.0403 e/f.u., which is still far from required 0.2 e/f.u. to induce the phase change of MoS_2[97]. Therefore, we start to use alloy $Mo_{1-x}Ti_xS_2$ as TMD layer. Alloy $Mo_{1-x}Ti_xS_2$ is expected to have lower phase change energy than the MoS_2, thus we expect lower charge density required to induce phase change as well. The phase change energy of $Mo_{0.6}Ti_{0.4}S_2$ is about 20% of the phase change energy of pure MoS_2. Following the Vegard's law, the charge density required to induce phase transformation of synthesized $Mo_{0.6}Ti_{0.4}S_2$ should be around 20% * 0.2 = 0.04 e/f.u., which is about the maximum charge density could be injected using 20nm Al_2O_3 as dielectric.

At first, we tried 15 nm $Mo_{0.5}Ti_{0.5}S_2$ sulfurized under 500 °C for 12 h with slow cooling, giving a leakage current of 0.62 μA under 10V. Although Al_2O_3 layer is degraded during sulfurization process, the capacitor shows charging or discharging behavior when we apply or stop applying

large voltages. The Al_2O_3 layer is exposed to H_2S under elevated temperature for about 20 hours (1 h ramping + 12 h annealing + 7 h cooling). To reduce the degradation effect, we used $Mo_{0.5}Ti_{0.5}S_2$ sulfurized under 600 °C for 1 h with quench cooling, which exposes Al_2O_3 layer H_2S under elevated temperature for only 2h (1 h ramping + 1 h annealing + 0 h cooling). The leakage current is 7.92 nA under 10 V, which is about 80 times smaller. The leakage current level is similar as the Al_2O_3 layer without sulfurization process, but the breakdown voltage is reduced to 10V, thus the Al_2O_3 layer is still degraded with shorter sulfurization time. 10V breakdown voltage reduces maximum charge density by half, which is far from enough to induce the phase transformation of our current synthesized $Mo_{1-x}Ti_xS_2$ samples. We have considered annealing Al_2O_3 to improve the crystalline, but high temperature could damage the TMD layer on top. Reducing the thickness of Al_2O_3 is also hard because 10 nm ALD-deposited Al_2O_3, even without sulfurization process, gives orders higher leakage current.

Table 5.1 summarizes all the dielectric materials we have tried on the phase change demonstration stack and corresponding leakage current density, breakdown voltage, and maximum charge density could be injected for monolayer TMD. For the measurement with voltage applying on two capacitors in series, we assume the capacitors are identical and reduce the voltage by half.

Dielectric materials	Thickness (nm)	Sulfurized	Voltage (V)	Leakage current density	Breakdown voltage (MV/cm)	Max charge density (e/f.u.)
SiO_2	100	No	2.5	0.1 μA/cm^2	> 2	0.0037
	100	Yes	1.0	10 μA/cm^2	0	0.0
Si_3N_4	100	Yes	2.5	3.23 nA/cm^2	> 2	0.0071
	14	Yes	8.54	1167 μA/cm^2	0	0.0
ALD Al_2O_3	20	No	10.0	41.11 nA/cm^2	10	0.0403
	20	Yes, 20h	5.0	6.89 μA/cm^2	5	0.0202
	20	Yes, 2h	5.0	88.0 nA/cm^2	5	0.0202

Table 5.1: Summary of all the dielectric materials we have tried on the phase change demonstration stack and corresponding leakage current density, breakdown voltage, and maximum charge density could be injected for monolayer TMD.

5.1.4. Experiments for ion-intercalation

As discussed above, the maximum charge could be injected into TMD films by voltage gating is limited by the breakdown voltage of the dielectric layer. Comparing with the voltage gating method, ion-intercalation method can inject more charge (about 1 e/f.u. for Li intercalation in MoS_2), which is enough to induce the phase transformation of MoS_2[98]. However, ion-intercalation is usually liquid-based and ion transportation is relative slow, the method could only be used as a test tool in research.

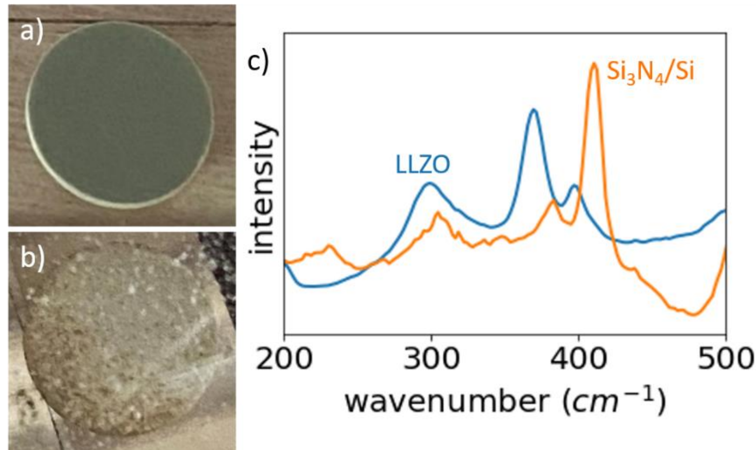

Figure 5.6: a) Sputtered $Mo_{0.5}Ti_{0.5}$ alloy precursor film on LLZO substrate b) Film on LLZO substrate after sulfurization under 550 °C for 1h with quench cooling c) Raman spectra of films on LLZO and Si_3N_4/Si substrate, which are synthesized under the exact same process. The film on Si_3N_4/Si substrate shows similar spectra as previous synthesized $Mo_{1-x}Ti_x$ films, but the film on LLZO doesn't.

Therefore, we tried to deposit $Mo_{0.5}Ti_{0.5}S_2$ on lithium lanthanum zirconium oxide (LLZO), a solid-state electrolyte. LLZO is very sensitive to the oxygen and we have to keep the sample in glovebox. We use vacuum sealing to seal the sample during transportation between labs. **Figure 5.6a** shows the Mo-Ti alloy deposited on LLZO pellet and **Figure 5.6b** shows the sample after sulfurization under 550 °C for 1h with quench cooling. The corresponding Raman spectrum in **Figure 5.6c** doesn't show any peaks from TMD. However, due to the scalability of our method, we synthesized another $Mo_{0.5}Ti_{0.5}S_2$ film on Si_3N_4/Si substrate with the same process. In **Figure 5.6c**, the film on Si_3N_4/Si shows $Mo_{0.5}Ti_{0.5}S_2$ Raman peaks, consistent with previous synthesized

samples, which proves that the process is valid. One reasonable explanation is that LLZO is sintered with roughness much larger than 20 nm. Therefore, the pellet can't be coated with continuous metal film by PVD, even though we can see the color change. The metal precursors are sulfurized in following sulfurization process and form discontinuous small $Mo_{1-x}Ti_xS_2$ crystals on LLZO. Therefore, the Raman signals from small $Mo_{1-x}Ti_xS_2$ crystals are too low to be detected. The discontinuous film is also not feasible for following Li-intercalation experiment.

5.2. Recommendation for Future Work

To further improve the film morphology, we believe that reducing the background O_2 concentration in the tube and controlling the sulfurization time would be useful. As discussed in **Chapter 4,** reducing O_2 level decreases the minimum process temperature for precursors containing Ti and suppresses all the kinetic roughening mechanisms. The current O_2 concentration is limited by the leaking rate of the quartz-to-metal seals on the tube furnace. Also, the oxide in the precursor could be a secondary oxygen source and a thermodynamic barrier for sulfurization. The process could be improved by using UHV technique and avoiding exposing the precursor to the air. Shortening sulfurization time reduces the time for phase separation and allows us to synthesize $Mo_{1-x}Ti_xS_2$ films with Mo:Ti ratio closer to 1, which is expected to have smaller phase change energy and lower barrier. The current sulfurization time is limited by the slow ramping rate of the furnace during the heating step.

To test the phase change behavior of alloy sulfide TMDs, we recommend following current voltage gating method and ion-intercalation method. For voltage gating, we propose a new design which switches the order of dielectric layer and TMD layers as shown in **Figure 5.7**. Therefore, the dielectric layer is deposited after the TMD sulfurization process and avoid the degradation. However, the new design requires to pattern ALD-deposited Al_2O_3 without damaging the TMD

layer underneath. One alternative method is using diamond scriber to scratch continuous ITO-dielectric-TMD multilayer to make isolated electrode-capacitor blocks, but the method is not scalable. ALD-deposited HfO_2 with dielectric constant of 26 and breakdown voltage of 4 MV/cm could also be a choice for dielectric material, which could inject 0.049 e/f.u. at maximum[99]. For ion-intercalation method, we suggest to mechanically press the film on the electrode instead of direct growth and try proton-intercalation as well.

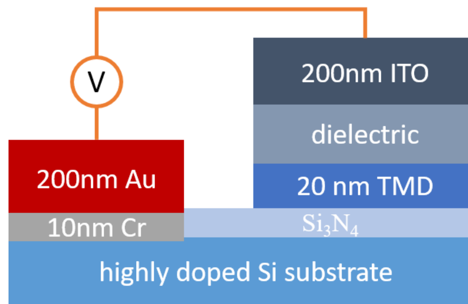

Figure 5.7: The new schematic diagram of phase change demonstration stack with dielectric layer above the TMD layer.

5.3. Conclusion and Key Findings of the Thesis

In view of the need for active materials for integrated photonics, and the challenges presented by established phase-change materials, we explore TMDs as candidates, due to the Martensitic phase transformation (expected to be fast and efficient) and the high optical contrast between different phases.

We measure the NIR optical property of telluride and sulfide TMDs and conclude that both telluride and sulfide TMDs have high optical density and large optical contrast between phases, but the sulfide has significant lower loss than tellurides in NIR. Thus, we suggest that the sulfide TMDs may be optimal for photonic phase-change.

Unfortunately, the energetic cost of switching between phases is much higher for pure sulfides (comparing to tellurides and selenides). Alloy design offers a path towards new and useful TMDs that combine the relatively low optical loss with lower switching energy. We theoretically predict

Gibbs free energy-composition curves and find $(Mo,Ti)S_2$ system with structural phases energetically degenerate at intermediate compositions.

We report the synthesis of large-area, single-phase 1T-TiS_2 thin films and large-area, high-Ti-content, single-phase 2H alloy $Mo_{1-x}Ti_xS_2$ (far-from-equilibrium) thin films via two-step method with sulfurization temperature as low as 500 °C. We also explore the roughening mechanisms for each case and expect the film roughness could be further reduced with lower O_2 background level, lower process temperature and better control of sulfurization time.

Bibliography

1. Asghari, M. & Krishnamoorthy, A. V. Energy-efficient communication. *Nat. Photonics* **5**, 268–270 (2011).
2. Shen, Y. *et al.* Deep learning with coherent nanophotonic circuits. *Nat. Photonics* **11**, 441–446 (2017).
3. Jalali, B. & Fathpour, S. Silicon Photonics. *J. Light. Technol.* **24**, 4600–4615 (2006).
4. Glass, A. M. Materials for Photonic Switching and Information Processing. *MRS Bull.* **13**, 16–20 (1988).
5. Yamada, N., Ohno, E., Nishiuchi, K., Akahira, N. & Takao, M. Rapid-phase transitions of GeTe-Sb $_2$ Te $_3$ pseudobinary amorphous thin films for an optical disk memory. *J. Appl. Phys.* **69**, 2849–2856 (1991).
6. Lee, B.-S. *et al.* Investigation of the optical and electronic properties of Ge2Sb2Te5 phase change material in its amorphous, cubic, and hexagonal phases. *J. Appl. Phys.* **97**, 093509 (2005).
7. Wong, H.-S. P. *et al.* Phase Change Memory. *Proc. IEEE* **98**, 2201–2227 (2010).
8. Wuttig, M. & Yamada, N. Phase-change materials for rewriteable data storage. *Nat. Mater.* **6**, 824–832 (2007).
9. Mak, K. F., Lee, C., Hone, J., Shan, J. & Heinz, T. F. Atomically thin MoS2: a new direct-gap semiconductor. *Phys. Rev. Lett.* **105**, 136805 (2010).
10. Splendiani, A. *et al.* Emerging photoluminescence in monolayer MoS2. *Nano Lett.* **10**, 1271–1275 (2010).
11. Chen, Y. *et al.* Tunable Band Gap Photoluminescence from Atomically Thin Transition-Metal Dichalcogenide Alloys. *ACS Nano* **7**, 4610–4616 (2013).
12. Schaibley, J. R. *et al.* Valleytronics in 2D materials. *Nat. Rev. Mater.* **1**, 16055 (2016).
13. Singh, A. *et al.* Long-lived valley polarization of intravalley trions in monolayer WSe2. *Phys. Rev. Lett.* **117**, 257402 (2016).
14. Singh, A. *et al.* Coherent Electronic Coupling in Atomically Thin MoSe2. *Phys Rev Lett* **112**, 216804 (2014).
15. Lv, R. *et al.* Two-dimensional transition metal dichalcogenides: Clusters, ribbons, sheets and more. *Nano Today* **10**, 559–592 (2015).
16. Mak, K. F. & Shan, J. Photonics and optoelectronics of 2D semiconductor transition metal dichalcogenides. *Nat. Photonics* **10**, 216 (2016).
17. Fiori, G. *et al.* Electronics based on two-dimensional materials. *Nat. Nanotechnol.* **9**, 768–779 (2014).
18. Singh, A. *et al.* Near-infrared optical properties and proposed phase-change usefulness of transition metal disulfides. *Appl. Phys. Lett.* **115**, 161902 (2019).
19. Li, Y., Singh, A., Krylyuk, S., Davydov, A. & Jaramillo, R. Near-infrared photonic phase-change properties of transition metal ditellurides. in *Low-Dimensional Materials and Devices 2019* (eds. Kobayashi, N. P., Talin, A. A. & Davydov, A. V.) 28 (SPIE, 2019). doi:10.1117/12.2532602.
20. Datta, I. *et al.* Low-loss composite photonic platform based on 2D semiconductor monolayers. *Nat. Photonics* **14**, 256–262 (2020).
21. Syrbu, N., Cebotari, V. Z. & Moldoveanu, N. P. Electronic and Vibrational Reflectivity and Absorption Spectra in ZrS2 Crystals. *Jpn. J. Appl. Phys.* **35**, 6126 (1996).
22. Buslaps, T., Johnson, R. L. & Jungk, G. Spectroscopic ellipsometry on 1T-TiSe2. *Thin Solid Films* **234**, 549–552 (1993).

23. Goldberg, A. M., Beal, A. R., Lévy, F. A. & Davis, E. A. The low-energy absorption edge in 2H-MoS $_2$ and 2H-MoSe $_2$. *Philos. Mag.* **32**, 367–378 (1975).
24. Lucovsky, G., White, R. M., Benda, J. A. & Revelli, J. F. Infrared-Reflectance Spectra of Layered Group-IV and Group-VI Transition-Metal Dichalcogenides. *Phys. Rev. B* **7**, 3859–3870 (1973).
25. Liu, L. *et al.* Phase-selective synthesis of 1T′ MoS2 monolayers and heterophase bilayers. *Nat. Mater.* **17**, 1108–1114 (2018).
26. Wang, Y. *et al.* Structural phase transition in monolayer MoTe2 driven by electrostatic doping. *Nature* **550**, 487–491 (2017).
27. Fujiwara, H. *Spectroscopic ellipsometry: principles and applications*. (John Wiley & Sons, 2007).
28. Engelsen, D. den. Ellipsometry of Anisotropic Films. *JOSA* **61**, 1460–1466 (1971).
29. Weber, J. W., Hansen, T. A. R., van de Sanden, M. C. M. & Engeln, R. B-spline parametrization of the dielectric function applied to spectroscopic ellipsometry on amorphous carbon. *J. Appl. Phys.* **106**, 123503 (2009).
30. Gilliot, M. Inversion of ellipsometry data using constrained spline analysis. *Appl. Opt.* **56**, 1173 (2017).
31. Gilliot, M. Semi-analytical method for n–k inversion of ellipsometry data. *Appl. Opt.* **58**, 800 (2019).
32. Gilliot, M. Wavelength-by-wavelength Kramers–Kronig consistent inversion of ellipsometry data. *Appl. Opt.* **58**, 8153 (2019).
33. Li, Y., Wu, Y., Yu, H., Takeuchi, I. & Jaramillo, R. Deep Learning for Rapid Analysis of Spectroscopic Ellipsometry Data. *Adv. Photonics Res.* 2100147 (2021) doi:10.1002/adpr.202100147.
34. Zhou, J., Xu, H., Li, Y., Jaramillo, R. & Li, J. Opto-Mechanics Driven Fast Martensitic Transition in Two-Dimensional Materials. *Nano Lett.* **18**, 7794–7800 (2018).
35. Gajdoš, M., Hummer, K., Kresse, G., Furthmüller, J. & Bechstedt, F. Linear optical properties in the projector-augmented wave methodology. *Phys. Rev. B* **73**, 045112 (2006).
36. Hohenberg, P. & Kohn, W. Inhomogeneous Electron Gas. *Phys. Rev.* **136**, B864–B871 (1964).
37. Kohn, W. & Sham, L. J. Self-Consistent Equations Including Exchange and Correlation Effects. *Phys. Rev.* **140**, A1133–A1138 (1965).
38. Kresse, G. & Furthmüller, J. Efficient iterative schemes for *ab initio* total-energy calculations using a plane-wave basis set. *Phys. Rev. B* **54**, 11169–11186 (1996).
39. Kresse, G. & Furthmüller, J. Efficiency of ab-initio total energy calculations for metals and semiconductors using a plane-wave basis set. *Comput. Mater. Sci.* **6**, 15–50 (1996).
40. Blöchl, P. E. Projector augmented-wave method. *Phys. Rev. B* **50**, 17953–17979 (1994).
41. Perdew, J. P., Burke, K. & Ernzerhof, M. Generalized Gradient Approximation Made Simple. *Phys. Rev. Lett.* **77**, 3865–3868 (1996).
42. Monkhorst, H. J. & Pack, J. D. Special points for Brillouin-zone integrations. *Phys. Rev. B* **13**, 5188–5192 (1976).
43. Lin, Y.-C., Dumcenco, D. O., Huang, Y.-S. & Suenaga, K. Atomic mechanism of the semiconducting-to-metallic phase transition in single-layered MoS2. *Nat. Nanotechnol.* **9**, 391–396 (2014).
44. Zhang, F. *et al.* Electric-field induced structural transition in vertical MoTe2- and Mo1–xWxTe2-based resistive memories. *Nat. Mater.* **18**, 55–61 (2019).

45. Jin, W. *et al.* Phase transition and electronic structure evolution of MoTe 2 induced by W substitution. *Phys. Rev. B* **98**, 4114–4120 (2018).
46. Duerloo, K.-A. N., Li, Y. & Reed, E. J. Structural phase transitions in two-dimensional Mo- and W-dichalcogenide monolayers. *Nat. Commun.* **5**, 4214 (2014).
47. Ma, L. *et al.* A metallic mosaic phase and the origin of Mott-insulating state in 1T-TaS2. *Nat. Commun.* **7**, 10956 (2016).
48. Hildebrand, B. *et al.* Short-range phase coherence and origin of the 1 T − TiSe 2 charge density wave. *Phys. Rev. B* **93**, 5140 (2016).
49. Ruppert, C., Aslan, O. B. & Heinz, T. F. Optical Properties and Band Gap of Single- and Few-Layer $MoTe_2$ Crystals. *Nano Lett.* **14**, 6231–6236 (2014).
50. Mleczko, M. J. *et al.* HfSe2 and ZrSe2: Two-dimensional semiconductors with native high-κ oxides. *Sci. Adv.* **3**, e1700481 (2017).
51. Bayliss, S. C. & Liang, W. Y. Symmetry dependence of optical transitions in group 4B transition metal dichalcogenides. *J. Phys. C Solid State Phys.* **15**, 1283–1296 (1982).
52. Greenaway, D. L. & Nitsche, R. Preparation and optical properties of group IV–VI2 chalcogenides having the CdI2 structure. *J. Phys. Chem. Solids* **26**, 1445–1458 (1965).
53. Wilson, J. A. & Yoffe, A. D. The transition metal dichalcogenides discussion and interpretation of the observed optical, electrical and structural properties. *Adv. Phys.* **18**, 193–335 (1969).
54. Fabbri, F. *et al.* Novel near-infrared emission from crystal defects in MoS2 multilayer flakes. *Nat. Commun.* **7**, 13044 (2016).
55. Li, W. *et al.* Broadband optical properties of large-area monolayer CVD molybdenum disulfide. *Phys. Rev. B* **90**, 195434 (2014).
56. Liu, H.-L. *et al.* Optical properties of monolayer transition metal dichalcogenides probed by spectroscopic ellipsometry. *Appl. Phys. Lett.* **105**, 201905 (2014).
57. Liang, W. Y. Optical anisotropy in layer compounds. *J. Phys. C Solid State Phys.* **6**, 551–565 (1973).
58. Hovenier, J. W. Structure of a general pure Mueller matrix. *Appl. Opt.* **33**, 8318–8324 (1994).
59. Gil, J. J. & Bernabeu, E. A Depolarization Criterion in Mueller Matrices. *Opt. Acta Int. J. Opt.* **32**, 259–261 (1985).
60. Arteaga, O. Useful Mueller matrix symmetries for ellipsometry. *Thin Solid Films* **571**, 584–588 (2014).
61. Ramsey, D. A. & Ludema, K. C. The influences of roughness on film thickness measurements by Mueller matrix ellipsometry: Review of Scientific Instruments: Vol 65, No 9. *Rev Sci Instrum* **65**, 2874 (1994).
62. Togo, A., Chaput, L., Tanaka, I. & Hug, G. First-principles phonon calculations of thermal expansion in Ti 3 SiC 2 , Ti 3 AlC 2 , and Ti 3 GeC 2. *Phys. Rev. B* **81**, 174301 (2010).
63. Youssef, M., Yildiz, B. & Van Vliet, K. J. Thermomechanical stabilization of electron small polarons in SrTi O 3 assessed by the quasiharmonic approximation. *Phys. Rev. B* **95**, 161110(R) (2017).
64. Togo, A. & Tanaka, I. First principles phonon calculations in materials science. *Scr. Mater.* **108**, 1–5 (2015).
65. Jo, S. S. *et al.* Formation of large-area MoS_2 thin films by oxygen-catalyzed sulfurization of Mo thin films. *J. Vac. Sci. Technol. A* **38**, 013405 (2020).

66. Li, Y. *et al.* Making Large-Area Titanium Disulfide Films at Reduced Temperature by Balancing the Kinetics of Sulfurization and Roughening. *Adv. Funct. Mater.* 2003617 (2020) doi:10.1002/adfm.202003617.
67. Singh, A. *et al.* Refractive Uses of Layered and Two-Dimensional Materials for Integrated Photonics. *ACS Photonics* (2020) doi:10.1021/acsphotonics.0c00915.
68. Zhou, J. *et al.* A library of atomically thin metal chalcogenides. *Nature* **556**, 355–359 (2018).
69. Shulaker, M. M. *et al.* Three-dimensional integration of nanotechnologies for computing and data storage on a single chip. *Nature* **547**, 74–78 (2017).
70. Yu, W. J. *et al.* Vertically stacked multi-heterostructures of layered materials for logic transistors and complementary inverters. *Nat. Mater.* **12**, 246–252 (2013).
71. Hong, S. *et al.* Chemical Vapor Deposition Synthesis of MoS_2 Layers from the Direct Sulfidation of MoO_3 Surfaces Using Reactive Molecular Dynamics Simulations. *J. Phys. Chem. C* **122**, 7494–7503 (2018).
72. Li, G. *et al.* All The Catalytic Active Sites of MoS_2 for Hydrogen Evolution. *J. Am. Chem. Soc.* **138**, 16632–16638 (2016).
73. Voiry, D. *et al.* Conducting MoS_2 Nanosheets as Catalysts for Hydrogen Evolution Reaction. *Nano Lett.* **13**, 6222–6227 (2013).
74. Zhao, Z. *et al.* Cathodoluminescence as an effective probe of carrier transport and deep level defects in droop-mitigating InGaN/GaN quantum well heterostructures. *Appl. Phys. Express* **12**, 034003 (2019).
75. Pore, V., Ritala, M. & Leskelä, M. Atomic Layer Deposition of Titanium Disulfide Thin Films. *Chem. Vap. Depos.* **13**, 163–168 (2007).
76. Gao, Z. *et al.* In Situ-Generated Volatile Precursor for CVD Growth of a Semimetallic 2D Dichalcogenide. *ACS Appl. Mater. Interfaces* **10**, 34401–34408 (2018).
77. Chang, H. S. W. & Schleich, D. M. TiS2 and TiS3 thin films prepared by MOCVD. *J. Solid State Chem.* **100**, 62–70 (1992).
78. Banus, M. D., Reed, T. B. & Strauss, A. J. Electrical and Magnetic Properties of TiO and VO. *Phys. Rev. B* **5**, 8 (1972).
79. Sugiyama, K. & Takéuchi, Y. The crystal structure of rutile as a function of temperature up to 1600°C. *Z. Für Krist. - Cryst. Mater.* **194**, (1991).
80. Chianelli, R. R., Scanlon, J. C. & Thompson, A. H. Structure refinement of stoichiometric TiS2. *Mater. Res. Bull.* **10**, 1379–1382 (1975).
81. Wood, R. M. The Lattice Constants of High Purity Alpha Titanium. *Proc. Phys. Soc.* **80**, 783–786 (1962).
82. Talib, M., Tabassum, R., Islam, S. S. & Mishra, P. Influence of growth temperature on titanium sulphide nanostructures: from trisulphide nanosheets and nanoribbons to disulphide nanodiscs. *RSC Adv.* **9**, 645–657 (2019).
83. McDonnell, S., Smyth, C., Hinkle, C. L. & Wallace, R. M. MoS_2 –Titanium Contact Interface Reactions. *ACS Appl. Mater. Interfaces* **8**, 8289–8294 (2016).
84. Onoda, M., Saeki, M. & Kawada, I. Stacking faults in nonstoichiometric titanium sulfide. *Phys. BC* **105**, 200–204 (1981).
85. Martin, N., Rousselot, C., Rondot, D., Palmino, F. & Mercier, R. Microstructure modification of amorphous titanium oxide thin films during annealing treatment. *Thin Solid Films* **300**, 113–121 (1997).

86. Salama, T. M., Tsunehiro Tanaka, Tsutomu Yamaguchi, & Kozo Tanabe. EXAFS/XANES study of titanium oxide supported on SiO2: A structural consideration on the amorphous state. *Surf. Sci.* **227**, L100–L104 (1990).
87. Prabhu, D. *et al.* Grain size effect on the phase transformation temperature of nanostructured CuFe2O4. *J. Appl. Phys.* **109**, 013532 (2011).
88. Frey, M. H. & Payne, D. A. Grain-size effect on structure and phase transformations for barium titanate. *Phys. Rev. B* **54**, 3158–3168 (1996).
89. Sun, Q., Aslan, A., Li, M. & Chen, M. Effects of grain size on phase transition behavior of nanocrystalline shape memory alloys. *Sci. China Technol. Sci.* **57**, 671–679 (2014).
90. Ermolaev, G. A. *et al.* Giant optical anisotropy in transition metal dichalcogenides for next-generation photonics. *Nat. Commun.* **12**, 854 (2021).
91. Qiu, D. Y., da Jornada, F. H. & Louie, S. G. Optical Spectrum of MoS 2 : Many-Body Effects and Diversity of Exciton States. *Phys. Rev. Lett.* **111**, 216805 (2013).
92. Molina-Sánchez, A., Sangalli, D., Hummer, K., Marini, A. & Wirtz, L. Effect of spin-orbit interaction on the optical spectra of single-layer, double-layer, and bulk MoS 2. *Phys. Rev. B* **88**, 045412 (2013).
93. Py, M. A. & Haering, R. R. Structural destabilization induced by lithium intercalation in MoS_2 and related compounds. *Can. J. Phys.* **61**, 76–84 (1983).
94. Imanishi, N., Toyoda, M., Takeda, Y. & Yamamoto, O. Study on lithium intercalation into MoS2. *Solid State Ion.* **58**, 333–338 (1992).
95. Li, Y., Duerloo, K.-A. N., Wauson, K. & Reed, E. J. Structural semiconductor-to-semimetal phase transition in two-dimensional materials induced by electrostatic gating. *Nat. Commun.* **7**, 10671 (2016).
96. Lin, H. C., Ye, P. D. & Wilk, G. D. Leakage current and breakdown electric-field studies on ultrathin atomic-layer-deposited Al2O3 on GaAs. *Appl. Phys. Lett.* **87**, 182904 (2005).
97. Acharya, J., Wilt, J., Liu, B. & Wu, J. Probing the Dielectric Properties of Ultrathin Al/Al_2O_3/Al Trilayers Fabricated Using *in Situ* Sputtering and Atomic Layer Deposition. *ACS Appl. Mater. Interfaces* **10**, 3112–3120 (2018).
98. Xiong, F. *et al.* Li Intercalation in MoS_2 : In Situ Observation of Its Dynamics and Tuning Optical and Electrical Properties. *Nano Lett.* **15**, 6777–6784 (2015).
99. Zhang, L. *et al.* ALD preparation of high-k HfO_2 thin films with enhanced energy density and efficient electrostatic energy storage. *RSC Adv.* **7**, 8388–8393 (2017).